Feasibility Analysis and Design of Wheeled Mobile Driving Simulators for Urban Traffic Simulation

Vom Fachbereich Maschinenbau an der
Technischen Universität Darmstadt
zur Erlangung des Grades eines
Doktor-Ingenieurs (Dr.-Ing.)
genehmigte

Dissertation

vorgelegt von

Alexander Betz, M.Sc.
aus Regensburg

Berichterstatter:	Prof. Dr. rer. nat. Hermann Winner
Mitberichterstatter:	Prof. Dr.-Ing. Günther Prokop

Tag der Einreichung:	03.06.2014
Tag der mündlichen Prüfung:	24.07.2014

Darmstadt 2015
D 17

Vorwort

Die vorliegende Arbeit entstand während meiner Tätigkeit als wissenschaftlicher Mitarbeiter am Fachgebiet Fahrzeugtechnik (FZD) der Technischen Universität Darmstadt. Die Erforschung der offenen Fragestellung wurde durch die Studienstiftung des deutschen Volkes maßgeblich unterstützt.

Herrn Prof. Dr. rer. nat. Hermann Winner danke ich für sein unermüdliches Streben und das mir entgegengebrachte Vertrauen. Sein hoher Anspruch sowie die gewährten Freiheiten trugen entscheidend zum Gelingen der vorliegenden Arbeit bei. Die unzähligen fachlichen Diskussionen haben mich stets inspiriert und nachhaltig geprägt.

Herrn Prof. Dr.-Ing. Günther Prokop danke ich herzlich für die Übernahme des Korreferats und den fachlichen Austausch, der das weitreichende Interesse an der erforschten Fragestellung zeigte.

Der Studienstiftung des deutschen Volkes danke ich für die Unterstützung auf finanzieller und wissenschaftlicher Ebene. Die durchgängige Bearbeitung des vorliegenden Forschungsprojekts wurde durch das Promotionsstipendium ermöglicht.

Desweiteren bedanke ich mich bei allen Mitarbeitern von FZD für das offene Arbeitsklima. Ich habe den fachlichen und privaten Austausch sehr geschätzt. Die ausgeprägte Hilfsbereitschaft ermöglichte einen besonderen Zusammenhalt. Die kompetente Unterstützung durch das Sekretariat und die Werkstätten, besonders im Hinblick auf dringende Anfragen, hat mir stets geholfen.

Darüber hinaus gilt mein Dank meinem Freundeskreis, den ich während der Schulzeit und dem Studium kennen und schätzen gelernt habe. Der regelmäßige Austausch sorgte für den benötigten Ausgleich zum Arbeitsalltag.

Nicht zuletzt danke ich meiner Familie für die ungebrochene Unterstützung während meiner gesamten Ausbildung. Ich bedanke mich für die Förderung meiner selbstgewählten Interessen. Ohne diesen Rückhalt wäre mir manch prägende Erfahrung verwehrt geblieben.

Besonders bedanke ich mich bei meiner Freundin Chrissi, die mich in allen Lebenslagen liebevoll unterstützt hat und mir die nötige Kraft gegeben hat, um besondere Herausforderungen anzugehen und zu bewältigen.

Alexander Betz   Darmstadt, Mai 2014

List of Contents

List of Abbreviations

Abbreviation	Description
AC	alternating current
ADAS	advanced driver assistance system
BC	best-case
CAN	controller area network
CDF	cumulative distribution function
CG	center of gravity
COS	coordinate system
CW	classical washout
DART	Darmstadt Racing Team
DC	direct current
DLR	Deutsches Zentrum für Luft- und Raumfahrt
DNE	does not exist
DOF	degrees of freedom
DS	driving simulator
dynCLC	dynamic closed-loop control
dynOLC	dynamic open-loop control
FKFS	Forschungsinstitut für Kraftfahrwesen und Fahrzeugmotoren Stuttgart
FMEA	failure mode and effects analysis
FTA	fault tree analysis
HDMI	high definition multimedia interface
HOC	human operator + cabin
HP	high-pass
IMU	internal measurement unit
kinCLC	kinematic closed-loop control
kinOLC	kinematic open-loop control
Li-Ion	lithium ion
Li-Po	lithium polymer
LP	low-pass
MCA	motion cueing algorithm
NADS	national advanced driving simulator
NiMH	nickel metal hydride
PSA	Peugeot Société Anonyme
SCP	simulation computer processing
SDD	sensory display devices
SFG	sensory feedback generation
SPDIF	Sony/Philips digital interface
TNO	Toegepast-natuurwetenschappelijk onderzoek
UNK	unknown
USB	universal serial bus

VeHIL	vehicle hardware in the loop
WC	worst-case
WMDS	wheeled mobile driving simulator
WMR	wheeled mobile robot

List of Symbols and Indices

Symbol	Unit	Description
a	m/s²	acceleration
b	m	translational stroke
c	N/m, N/°	stiffness (e.g. spring stiffness in N/m or cornering stiffness in N/°)
D	m	diameter
d	m, 1	e.g. displacement in m (in section 3.2.2 d is the dimensionless damping)
E	J	energy
F	N	force
f	Hz	frequency
G	1	transfer function (e.g. loop gain or PT2-gain)
g	9.81 m/s²	gravity
h	m	height
K	m/s²	Amplitude of the acceleration step input
KP	1	proportional control gain
KI	1	integral control gain
l	m	length (e.g. edge length)
M	Nm	moment (e.g. yaw moment)
m	kg	mass
P	W	power
Q	1	Quantile
q	1	Axis of coordinates of the rotor fixed COS of the electrical motor
r	m	radius
T	Nm, s	torque (e.g. torque of a motor in Nm. In section 3.2.2 T is the time constant of a low-pass filter in s)
t	s	time
u	miscellaneous	mathematical term (e.g. substitute term for the sake of readability)
v	m/s	velocity
y	m/s²	step response (e.g. step response of the low-pass filter of the acceleration signal)
α	°	slip angle
β	°, rad	angle (e.g. angle of the knee lever design)
γ	°, rad	angle (e.g. angle of the knee lever design)
δ	°, rad	wheel steer angle
θ	kgm²	moment of inertia
ϑ	°, rad	roll angle
μ	1	friction coefficient
ξ	°, rad	angle of wheel orientation with respect to the earth fixed COS
ρ	°, rad	angle of resulting wheel force with respect to the DS COS
τ	1/s	inverted time constant (e.g. inverted feedback gain)
φ	°, rad	angle (e.g. pitch angle. In section 3.5.6 and appendix F.2 φ is an angle of the

Symbol	Unit	Description
		knee lever design)
ψ	°, rad	yaw angle
ω	rad/s	angular frequency

Index	**Description**
act	actuation
avg	average
BC	best-case
CG	center of gravity
continuous	continuous
correvit	Correvit Sensor
curve	curve
d	displacement
dem	demand
des	desired
drive	drive unit
DS	driving simulator
dyn	dynamics
E	earth fixed (e.g. earth fixed coordinate system)
err	error
final	final
fric	friction
I	inertial (e.g. inertial coordinate system)
i	numeration (e.g. wheel number)
ic	inscribed circle
in	indicated
inital	inital
joint	mechanical joint
kin	kinematic
lat	lateral (e.g. lateral direction)
lifting	lifting
limit	limit
long	longitudinal (e.g. longitudinal direction)
loop	loop
max	maximum
mean	mean
min	minimum
peak	peak
plateau	plateau (e.g. plateau of a curve in a diagram)
pre	pre-tuning
Q90	90 % quantile
Q99	99 % quantile
ref	reference
res	resulting
rot	rotation/rotational
sim	simulation
slide	linear slide
spring	spring

steer	steer (e.g. belonging to the steer unit)
t	triangle
total	total/over-all
traction	traction (e.g. traction motor)
trans	translation/translational
V	vehicle (e.g. vehicle coordinate system)
v	velocity
WC	worst-case
w	wheel
x	x direction (e.g. longitudinal direction)
y	y direction (e.g. lateral direction)
yaw	yaw
z	z direction (e.g vertical direction)
zz	Rotation around the z-axis
α	lateral direction of the wheel

Summary

Driving simulators (DS) are established developmental tools in the automotive industry. DS applications may cover a wide portfolio such as driver behavior analysis, human machine interface development, dimensioning of chassis components in an early developmental stage and development of advanced driver assistance systems (ADAS). The versatile areas of application all profit from a high degree of reproducibility, safety and cost reduction when compared to real-world test methods. Especially for the analysis of safety-critical situations, DS constitute an adequate tool.

From a historical viewpoint DS were mainly developed for motorway traffic and overland driving. Modern-day DS show up to 12 degrees of freedom (DOF). They have reached remarkable quality in simulating real-world driving experiences but are still strongly limited in terms of providing both extensive translation motion and high acceleration amplitudes. New research perspectives such as urban traffic simulation are in conflict with the drawbacks of state-of-the-art DS and demonstrate the urgency of a profound redesign of motion systems of DS. The present work analyzes the feasibility of a self-propelled motion system design in order to pave the way for enhanced traffic safety research.

A top down methodology is used to analyze the feasibility of the wheeled mobile driving simulator (WMDS) with respect to the derived falsification aspects: power, energy, friction coefficient, motion control, and safety architecture. In order to investigate the feasibility and analyze the limitations of the WMDS, a requirement analysis is conducted. Thus, motion properties of urban traffic are identified using real-world test drives. A representative motion algorithm of the WMDS is developed that transforms the motion cues of the dynamics of the real-world vehicle into the corresponding actuator tasks of the WMDS. The architecture of the motion algorithm is designed to take advantage of the unlimited horizontal motion capability of the WMDS. The validation of the WMDS is evaluated by the falsification aspects using analytical and numerical analysis of the driving dynamics of the WMDS as well as hardware testing. A software prototype in the form of a multi-body simulation as well as a physical reference system is developed for this purpose.

For the first time, the physical feasibility of a WMDS and its system limitations are scientifically investigated and enable an attempt into the sparsely researched state of factual information on the new class of DS. As shown by the insights gained into the WMDS, its feasibility is promising. The derived friction coefficient demand is feasible with conventional tire compounds. The energy demand mainly results from the traction motors as their average power demand is significantly greater than that of the steer motors. Several hours of operation time can be realized for the wheeled motion base by state-of-the-art traction batteries. Even if the steer motors hardly raise the energy demand, the rarely occurring peak power demand they present is greater than that of the traction motors. The peak power demand is the result of the worst-case steer step in standstill and strongly depends on the tolerated time delay. This steer task thus turns out to exhibit the greatest requirements identified in the present work. The motion control created is validated by the numerical multi-body simulation. The safety architecture developed allows the secure braking of the WMDS until standstill even in case of electrical outage.

Of all the conducted effort in the present work, none has been able to falsify the feasibility of the representative WMDS developed. The new DS architecture allows for far-reaching improvements of DS studies and is accompanied by cost reductions that enable a wider researcher base and the superior goal of traffic safety. The hardware prototype and the safety architecture developed are unprecedented worldwide and thus enable the research of the pending objectives.

1 Introduction and Goal

1.1 Motivation

Driving simulators (DS) are established developmental tools in the automotive industry. A DS is intended to create a realistic driving experience for a subject. The behavior it elicits in the subject via the tools of simulation must therefore correspond to that found in real-world driving, creating a sufficient match between the two. DS applications may cover a wide portfolio, such as driver behavior analysis, human-machine interface development, dimensioning of chassis components in an early developmental stage and development of advanced driver assistance systems (ADAS).[1,2,3,4] The versatile areas of application all profit from a high degree of reproducibility, safety and cost reduction when compared to real-world test methods. Especially for the analysis of safety-critical situations, DS constitute an adequate tool.

According to Blana[3], highway research simulators were developed in the 1950's and the activity has increased over the past several decades. It was during the past decade that development of ADAS such as adaptive cruise control or lane departure warning and lane keeping support were developed. Advances in technology combined with knowledge gained in the development of ADAS led to a shift of focus onto urban traffic situations. The main reason for urban traffic accidents in Germany is human error in common traffic situations, such as turning, U-turning, drive-away and reversing.[5,6,7] The upcoming demand for ADAS with respect to urban traffic situations is expected to result in increasing DS requirements concerning workspace and system dynamics. This problem is well known in the automotive industry, as confirmed by Zeeb in 2010: "To induce a much better longitudinal motion sensation with a scaling factor close to 1:1 for all possible acceleration and deceleration scenarios even a several ten meter long sledge would not be sufficient, but would increase the technical and financial effort tremen-

[1] Zeeb: Daimler DS, 2010.

[2] Baumann, et al.: DS of Stuttgart University, 2012.

[3] Blana: Survey of DS, p. 4-5, 1996.

[4] Chapron; Colinot: PSA DS, 2007.

[5] Deutsches Statistisches Bundesamt: Unfallgeschehen 2007, 2008.

[6] Deutsches Statistisches Bundesamt: Unfallgeschehen 2008, 2009.

[7] Deutsches Statistisches Bundesamt: Verkehrsunfälle 2009, 2010.

dously, especially when the […] mandatory requirements for drive dynamic experiments have to be fulfilled."[8]. The problem becomes even more challenging in the simulation of traffic maneuvers that require combined longitudinal and lateral dynamics, as described in the following.

A simple T-junction example emphasizes Zeeb's statement and provides an impression of workspace demand. The workspace demand of a DS differs from the real-world motion because the related accelerations that are felt by the driver are performed by a superposition of horizontal motion and tilt of the cabin of the DS. The use of the so-called tilt coordination enables the DS to perform the acceleration simulation within reduced workspace compared to the vehicle motion in a real-world setting as presented later in sections 2.1.5 and 2.2. If a vehicle approaches a T-junction at 50 km/h and decelerates at 3 m/s² before making a 90° turn and reaccelerating to 50 km/h, then the DS trajectory of Figure 1.1 is produced. The figure shows the required workspace demand of approx. 50x140 m² with information about the phase of the maneuver of the vehicle that is being simulated. The information in Figure 1.1 is derived by a so-called motion cueing algorithm (MCA) that transforms the vehicle's motion into the DS motion, as described later in section 2.3.2. Obviously, this quite basic situation requires a 90° yaw angle. While very few existing simulators provide this required yaw angle, none complies with the workspace demand illustrated by this common urban traffic situation as confirmed by a literature survey in section 2.5. Hence, this example exceeds the specifications of all known DS. Similar findings are presented in Zöller et al.[9] for a DS study of a highly dynamic collision avoidance situation.

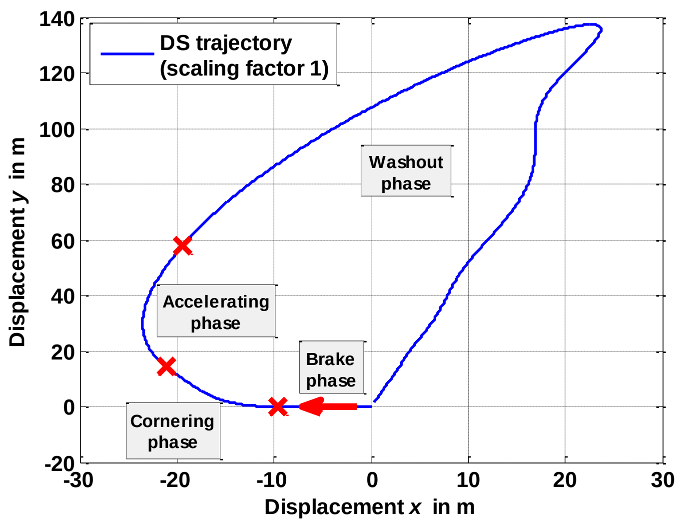

Figure 1.1: Workspace demand – T-junction example

[8] Zeeb: Daimler DS, p. 162, 2010.

[9] Zöller et al.: Validity of DS, accepted in 2014.

Modern-day DS are presented in Figure 1.2 and show up to 12 degrees of freedom (DOF). They have reached remarkable quality in simulating real-world driving experiences but are still strongly limited in translational motion (max 35 x 20 m^2)[10]. These improvements induce great costs due to system complexity and an increased moving mass of about 80 t[11]. Along with the redundant DOF, the main reason for high moving mass results from the rail systems used to connect the tilt system of the cabin to the ground. This effort is accepted to resolve the strongly limited translational motion envelope. As a result, a link between moving mass and workspace is caused, thus limiting motion envelope and system dynamics.

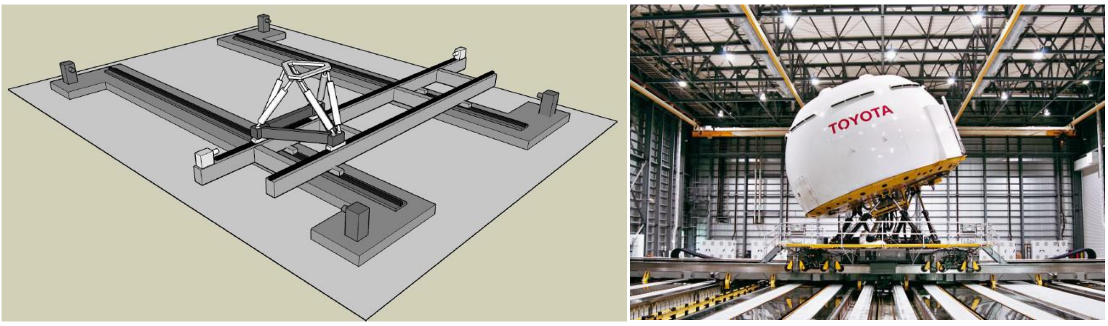

Figure 1.2: State-of-the-art DS (left[12]; right[10])

The illustrated drawbacks of state-of-the-art DS demonstrate the urgency of a profound redesign of motion systems of DS. The present work analyzes an alternative motion system design in order to pave the way for enhanced traffic safety research and a reduction of traffic accidents and fatalities.

1.2 Scientific Goal and Working Hypothesis

According to Allen et al.[13] the most significant hardware costs of DS now arise from the motion systems and the DS cabin. Thus, the focus of this work concentrates on technical aspects of the simulator motion and its control. Ergonomic criteria are considered only by means of human perception thresholds for motion as they are known from the literature. Further elements of DS are only presented in a short form in order to provide orientation.

[10] Murano et al.: Toyota DS, 2009.

[11] Clark et al.: NADS motion system, 2001.

[12] Carlsson et al.: DS of Stuttgart University, 2009.

[13] Allen et al.: History of DS, p. 2-4, 2011.

This work is intended to analyze the feasibility of a self-propelled motion system for motion simulation of urban traffic. The self-propelled approach promises to solve the drawback of state-of-the-art DS introduced above with regard to the link between workspace and moving mass. The present work is restricted to the class of self-propelled, wheeled DS. This focus is the result of preliminary research[14]. In this research, the self-propelled, wheeled DS concept distinguished itself from alternative concepts. No evident exclusion criterion is known to the author that denies the feasibility of the new DS concept. This new class of self-propelled DS is called “wheeled mobile driving simulator” (WMDS) by the author of the present work. The motion of the WMDS is performed by actively driven and steered wheels. To the author’s knowledge, a comprehensive analysis with respect to the feasibility of WMDS has not been carried out within the scope of any research project.

The scientific goal is based on the assumption that a wheeled system whose propulsion is limited by friction forces is suitable to simulate the dynamics of vehicles that are also limited by tire friction forces. In accordance with this basic assumption, the following working hypothesis is derived:

> H1: The wheeled motion base of a WMDS with its dynamics limited by friction forces is capable of simulating the horizontal dynamics of urban traffic for normal driver behavior considering common scaling factors.

The two restrictions of the hypothesis concerning normal driver behavior and common scaling factors are stipulated because no effort is desired that causes higher requirements than necessary. First, the driving experience that is intended to be reproduced in the DS is limited in its dynamics due to the driving behavior of normal drivers (further details are found in section 4.1.3). In other words, no expert or racecar drivers are considered and the road traffic regulations are obeyed. Second, advantage is gained from the common scaling factors as they are found in the literature because human perception may be fooled in certain ranges without causing disturbing losses in the perceived driving experience (further details can be found in section 2.1.4 and 2.2).

The falsification of the stated hypothesis is subject to critical aspects that must be analyzed in the present work. If one of the falsification aspects yields requirements that cannot be met by the WMDS, the hypothesis must be rejected. The falsification aspects are as follows:

- Power demand:
  Performing the acceleration simulation using a real system with mass requires tire forces. The question then arises as to whether the required power demand is feasible with state-of-the-art actuators.

[14] Betz: Preliminary WMDS research, 2010.

- Energy demand:
  Providing the aforementioned power of the actuators yields energy demand. It is questionable if the required energy demand is feasible with the state-of-the-art energy supply. It must be evaluated whether the energy supply can be realized as an on-board solution or not because this influences the system design significantly.
- Friction coefficient:
  The required tire forces must be transmitted to the ground. It is arguable whether the related friction coefficient can be realized by the tires used.
- Motion control:
  The acceleration simulation of the DS must be realized by coordination of the available actuators. The question of whether a motion control exists that decomposes the overall acceleration task into manageable assignments of the single actuators must be answered.
- Safety architecture:
  The created WMDS is an unbound motion platform that carries subjects. In case of an emergency, the kinetic energy must be reduced in a controlled manner in order to bring the system into a safe state. The question arises as to whether a safety architecture exists that enables emergency stops without harming the subject, the system, and the surroundings.

1.3 Basic Methodology

A top down methodology is used to analyze the feasibility of the WMDS according to the derived falsification aspects of the stated hypothesis. Figure 1.3 presents an overview of the applied methodology.

In order to investigate the feasibility and analyze the limitations of the WMDS, a requirement analysis is conducted. Thus, motion properties of urban traffic are identified using the aforementioned single T-junction maneuver (section 1.1, Figure 1.1) and real-world test drives in the form of a representative urban circuit (in Figure 1.3, see Test maneuver + Vehicle dynamics). The 8-track maneuver that is also provided is not used to determine DS requirements but is useful to validate the developed motion control because transient cornering is contained in a comprehensible, single maneuver.

A representative motion algorithm of the WMDS is developed that transforms the motion cues of the real-world vehicle's dynamics into the corresponding actuator tasks of the WMDS (in Figure 1.3, see Motion cueing algorithm + DS dynamics + Motion control). The architecture of the MCA is designed to take advantage of the WMDS's system-immanent motion capability. The DS dynamics provides insights into the DS trajectory task; hence, knowledge about the necessary workspace demand is gained as shown in Figure 1.3. Based on the developed motion control of the WMDS, the falsification aspects (energy, power, and friction demand) are accessible. The primary function of the tool chain created so far is the requirement analysis.

The validation of the motion control and the safety architecture is examined using analytical, numerical, and hardware models of the WMDS's driving dynamics. A software prototype in the form of a multi-body simulation as well as a physical reference system is developed for this purpose (in Figure 1.3, see Prototype software & hardware).

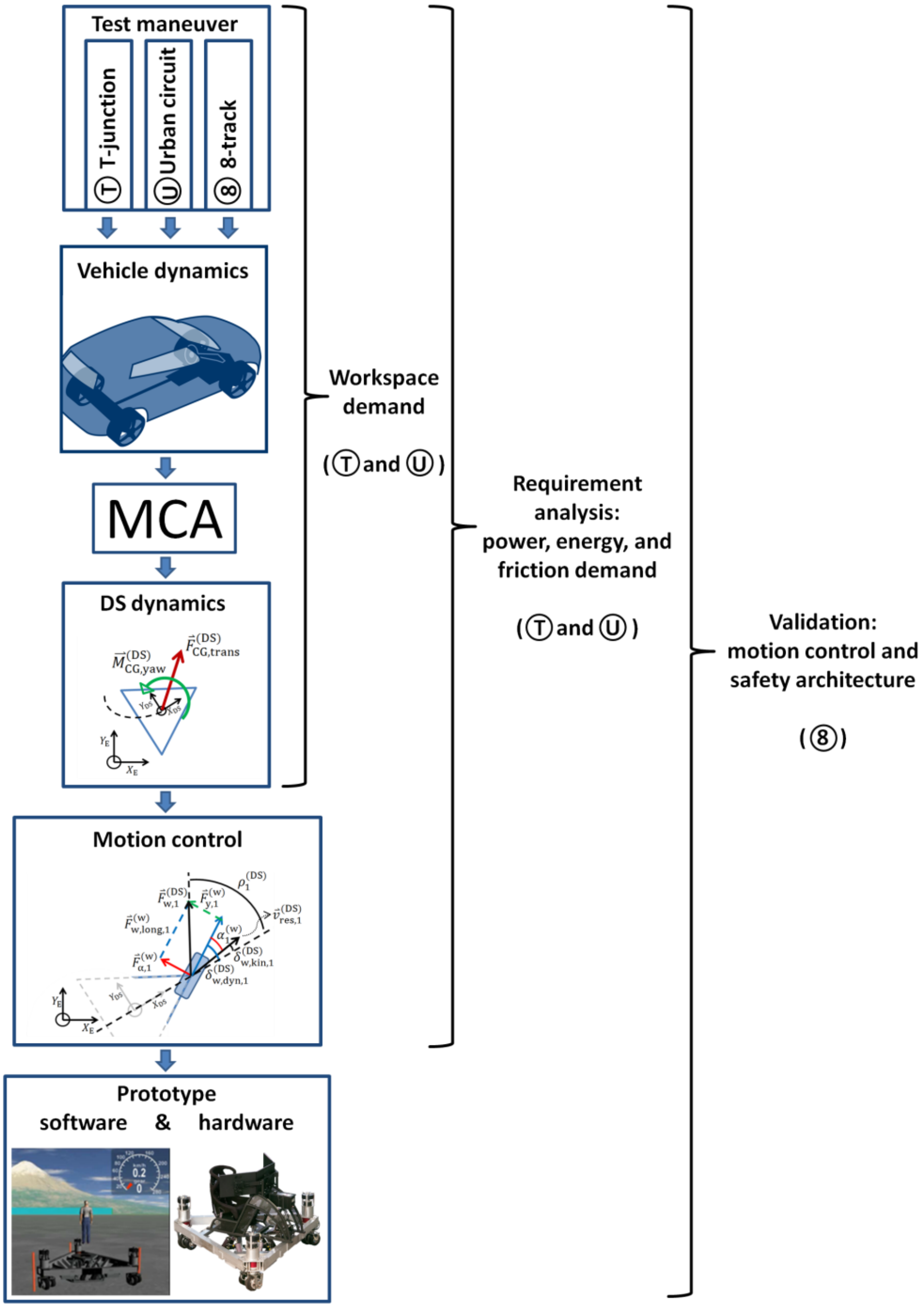

Figure 1.3: Overview of the applied methodology

1.4 Structure of the Thesis

The present work consists of six sections. The structure differs from the order of the introduced methodology. Instead, the structure is intended to provide a comprehensible documentation of the self-contained, fundamental elements of the WMDS and the related derivations. Therefore, the following sections are grouped as listed below:

2. State of the Art:
   This section starts with definitions and basics that are necessary in order to follow the reasoning of the present work (section 2.1). Because the focus of the present work is limited to the motion system of DS only, the nexus of the overall DS is briefly introduced (section 2.3). Subsequently, the focus is aimed at the motion system of state-of-the-art DS in order to identify their specifications and limitations (section 2.5). After conclusion of the study of limitations found in state-of-the-art DS, the idea of the self-propelled, wheeled DS is explored in the form of information found in the literature and existing similar applications (section 2.6). The section ends with a brief introduction of battery technology, as it is important for the question of the feasibility of the on-board energy supply.
3. System Design:
   This section contains all elements that are developed in order to answer the open research questions of the aforementioned falsification aspects. Because those elements are tailored for one representative solution of the class of WMDS, it is necessary to introduce the major design characteristics of the selected solution (section 3.1). On this basis, an “ideal” MCA along with its parameterization is described that copes with the system-immanent motion capability of the characteristics of an unbound WMDS (section 3.2). The output of the MCA must be interpreted in the motion control in terms of the necessary wheel forces and their control by the actuators (section 3.3). The architecture of the closed loop control is implemented into the aforementioned algorithms (section 3.4). The section is completed with the final design of the representative WMDS and its safety architecture (section 3.5).
4. Evaluation Tools:
   This section treats the necessary tools that are applied in order to evaluate the elements of section 3. First of all, the test maneuvers are introduced that are used for evaluating the hypothesis and the related falsification aspects (section 4.1). The requirement analysis is based on the T-junction maneuver (section 4.1.1) and the representative urban circuit (section 4.1.3). The validation of the derived motion control of section 3 is conducted on the basis of the 8-track maneuver because this is a comprehensible maneuver that contains transient cornering (section 4.1.2). The validation of the safety architecture is realized by hardware

tests performing emergency stops (section 4.1.4). The 8-track test is realized by numerical simulation utilizing a multi-body model of the WMDS (section 4.2).

5. Results:
   In order to test the hypothesis, the open research questions of the falsification aspects are evaluated using the system design of section 3 and the tools of section 4. The falsification aspects are treated in four steps. The results of the T-junction maneuver sheds light on the requirement analysis of a representative single maneuver of urban traffic (section 5.1). This single traffic maneuver is a subset of the following urban traffic circuit but is easier to understand due to its traceability. A comprehensive requirement analysis of urban traffic is analyzed by the representative urban traffic circuit that combines different traffic maneuvers conducted by normal drivers (section 5.2). The validation of the coordination of the actuators is conducted by the numerical multi-body simulation of the 8-track maneuver (section 5.3). Finally the section ends with the experimental results of the hardware tests concerning the safety architecture (section 5.4).
6. Conclusion and Outlook:
   This section summarizes the scientific goals considering the results gained as described in section 5. The hypothesis is evaluated and further insights are discussed with respect to the feasibility of the WMDS and its possible optimization (section 6.1). The outcome of the present work is classified with respect to the state-of-the-art in DS technology, and the future research goals are presented (section 6.2).

2 State of the Art

2.1 Definitions and Basics

2.1.1 Coordinate System (COS)

The COS used corresponds to DIN standard 70000[15] and is presented in Figure 2.1. Index E refers to the earth fixed COS and is the reference system. The vehicle's COS has the index V and is transformed by translational offset (not illustrated in Figure 2.1) and three angels: φ, θ, and ψ. The leveled coordinate system is the result of disregarding the rotation about the X and Y-axis. In the present work, this pitch and roll motion is disregarded; thus the leveled COS is identical to the one of the vehicle (V). Because the WMDS itself is a vehicle, the index DS is used to distinguish it from the COS of the vehicle. As exemplarily shown in Figure 2.2, an additional COS is introduced for the wheels (W). The COS of the wheels is transformed by the angle δ with respect to the DS COS. Therefore, four different indices are used for the various COS: E = earth fixed, V = vehicle, DS = driving simulator, W = wheel.

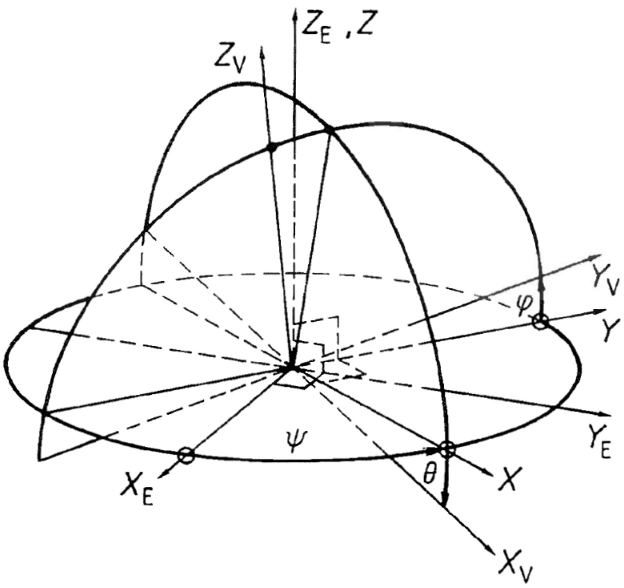

Figure 2.1: COS implemented according to DIN standard 70000[15]

[15] DIN 70000, ISO 8855: Fahrzeugdynamik und Fahrverhalten, 1991.

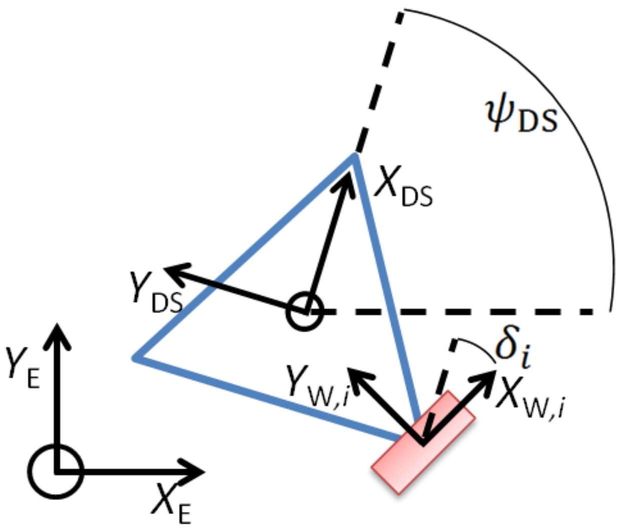

Figure 2.2: Angular correlation between the different COS

2.1.2 Wheeled Mobile Driving Simulator (WMDS)

The wheeled mobile driving simulator is a familiar application to the class of the wheeled mobile robots (WMR). The applications of both classes are supposed to perform horizontal motion that is realized by tire forces. Because wheeled mobile robots are widely known as WMR, the logical abbreviation for the DS application is determined to be WMDS.

2.1.3 Motion Cue

The term "motion cue" is used in Baarspul[16] as sensory information that is provided to the subject in flight simulators. This information is grouped according to the sensory channels of human beings – vision, audition, tactition and vestibular. Some references use the term "motion cues" for vestibular information only.[17] The present work is focused on the acceleration simulation of DS. Because the vestibular system and the proprioceptors of the skin and the muscles are the most important sensory organs for acceleration perception, the term "motion cues" is introduced as the cue carrying solely acceleration information for those sensory organs. This definition is according to Grant[18]. The individual word cue is used to describe signals carrying information for the other sensory channels.

[16] cf. Baarspul: Motion cues of flight simulation, 1986, according to Fischer: MCA DLR, p. 5, 2009

[17] Fischer: MCA DLR, p. 5, 2009.

[18] cf. Grant: Motion algorithm of flight simulators, 1995, according to Fischer: MCA DLR, p. 5, 2009

2.1.4 Scaling and Scaling Factor

Scaling is a preprocessing of the motion cues. The amplitude of the original signal is multiplied by a factor smaller than 1. Thus, the amplitude of the original signal as well as the necessary motion performance is reduced. This process is frequency-independent and modifies the amplitude uniformly across all frequencies.[19] Because human perception is subject to typical sensing errors, the original signal may be reduced within a certain range without shortening the driving experience.[20] The scaling factor is determined depending on the available motion system and the test drives conducted. The difficulty is to be able to determine the effect of the scaling factor on the validity of the created driving experience. If validity is compromised, the goal of the study is missed. The present work is not intended to research tolerated scaling factors or their influence on the validity of DS studies. Hence, common scaling factors are used (1, 0.7, and 0.5) as they are found in the literature in order to investigate the effect on the requirements analysis.[20,21,22]

To the author it is not clear if yaw motion should also be scaled. Scaling the yaw motion would match the scaled lateral acceleration impression but harm the visual feedback which, of course, remains unscaled. Because yaw motion is an unlimited motion capability of the researched WMDS, it is not scaled, causing a worst case assumption for the yaw task.

2.1.5 Tilt Coordination

According to Reid[19], Nahon[23], and Fischer[24], Tilt Coordination describes the utilization of subject tilt (with respect to the gravity vector) in order to create a horizontal acceleration impression. If the subject is visually shielded from the surroundings and has no reference to the horizon, it perceives tilt as a superposition of horizontal acceleration and gravity. Because this rotational motion does not require translational workspace, it is suitable for performing long-lasting motion cues. The limitations due to the subject's perception of tilt are described in section 2.2.

---

[19] Reid; Nahon: Motion algorithm of flight simulators, 1985.

[20] Greenberg et al.: Lateral motion cues, 2003.

[21] Brünger-Koch et al.: DS motion assessment, 2006.

[22] Fischer: MCA DLR, p. 57-58, 2009.

[23] Nahon; Reid: MCA, 1990.

[24] Fischer: MCA DLR, p. 7, 2009.

2.1.6 Washout

Washout is an important approach to reducing the required workspace of a DS system. The goal is to return the DS into its initial position because this point shows maximum workspace to all directions.[25] The returning motion must not be noticed by the subject because this would impede the created driving experience. To mask the subject's perception of the returning motion, tilt coordination is utilized. The word "washout" is also frequently used as a short form of classical washout, which stands for one specific MCA or MCA in general.[26,27]

2.2 Human Perception of Motion

Human beings use several senses to determine motion. The information gained through these senses is merged in the brain to determine the human's position and motion in space. This "sensor fusion" is a complex process involving visual, auditive, tactile and vestibular information of the related sensory organs. The fusion is important because it compensates for the weaknesses of the individual senses operating on their own. If the discrepancies between conflicting sensory inputs give rise to conflict with a plausible overall impression, confusion and nausea are the possible consequences. In DS context, this is known as simulator sickness. Essentially, it can be stated that the individual senses may be fooled as long as the overall impression presents a plausible image of the known situation. Because the present work deals only with the motion system of DS, the description of human perception principles is limited to the vestibular organ because it is the most essential one for acceleration perception.[28,29]

2.2.1 Vestibular

The human perception of acceleration is mainly based on the vestibular organ[30,31] which is situated in the inner ear as illustrated in Figure 2.3. The vestibular organ senses three translational and three rotational accelerations.

---

[25] Fischer: MCA DLR, p. 6, 2009.

[26] Reid; Nahon: Motion algorithm of flight simulators, 1985.

[27] Nahon; Reid: MCA, 1990.

[28] Fischer: MCA DLR, p. 8, 2009.

[29] Richter: Acceleration simulation in DS, p. 11, 1971.

[30] Fischer: MCA DLR, p. 9-11, 2009.

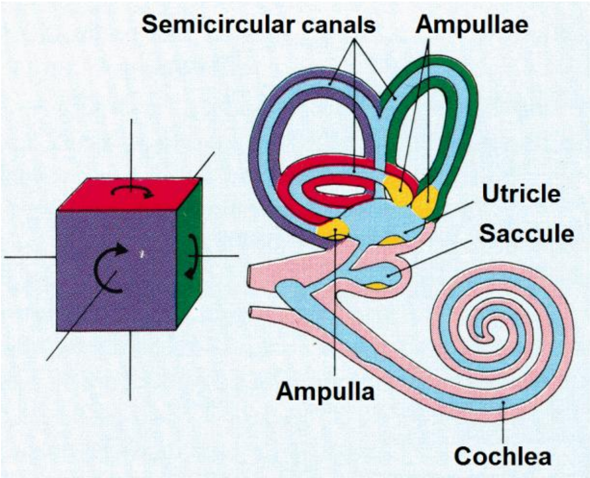

Figure 2.3: Vestibular organ[32]

The rotational sensing occurs in the ampullae of the semicircular canal which is filled with a viscous fluid that allows relative motion between the fluid and the wall of the canal. The relative motion is sensed due to bending of the cupula which extends into the fluid as shown in Figure 2.4.[33] The vestibular organ is comprised of three of these semicircular canals that are positioned perpendicular to each other.

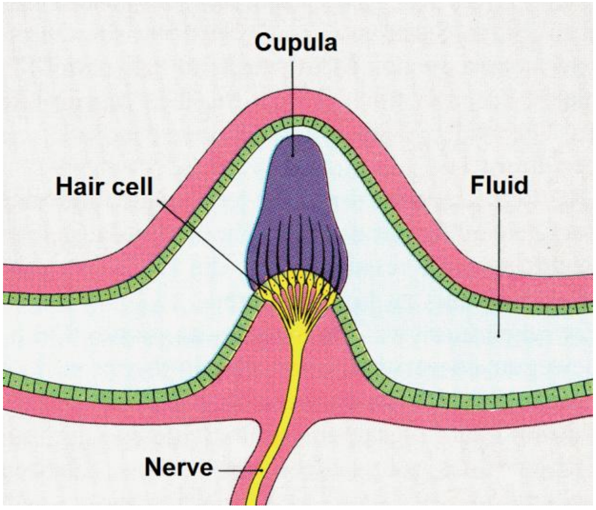

Figure 2.4: Cupula as an element of the vestibular organ[32]

The translational acceleration sensing occures in the utriculus and sacculus chamber of the vestibular organ. The macula is presented in Figure 2.5 and works similarly to the previously described cupula but is not excited due to the fluid's volume flow. It utilizes statoliths (otoconia) that are positioned on top of a jelly pillow. The statoliths and the

[31] Dobbeck: Acceleration simulation in DS, p 11, 1974.

[32] cf. Miram; Krumwiede: Stimulus processing, 1985, according to Fischer: MCA DLR, p. 9-10, 2009

[33] cf. Tiesler: Motion perception, 1973, according to Fischer: MCA DLR, p. 10, 2009

jelly pillow differ in mass. Due to the different mass, the inertia force causes relative motion that is sensed.

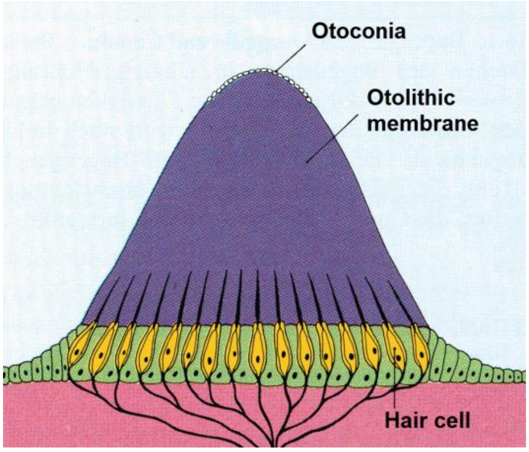

Figure 2.5: Macula as an element of the vestibular organ[34]

For further details concerning the vestibular principle, please see the comprehensive description summarized by Fischer[35].

2.2.2 Acceleration Perception in Driving Simulators

The complex fusion of the various perceptions allows for deviations in the acceleration simulation. One important property of human perception is the aforementioned misinterpretation of gravity when the subject is being tilted about the pitch or roll axis (tilt coordination: section 2.1.5). Due to the setup of the vestibular organ, it cannot distinguish between true horizontal acceleration and translational acceleration impression caused by tilt around the pitch or roll axis. This phenomenon is limited to about a 20° to 30° tilt angle which allows horizontal acceleration simulation of about 0.34 to 0.5 g by tilt.[36] At higher tilt angles, the subject realizes reduced vertical acceleration in its tilted coordinate system and notices the fooling.[37] The utilization of this phenomenon is widely used in DS. For the present work the maximum applied acceleration by tilt is limited to 0.4 g (≈ 24°) because this seems to be a representative value according to the range introduced by Mittelstädt[36].

[34] cf. Miram; Krumwiede: Stimulus processing, 1985, according to Fischer: MCA DLR, p. 9-10, 2009

[35] Fischer: MCA DLR, p. 9-20, 2009.

[36] cf. Mittelstädt: Tilt coordination, 1985, according to Fischer: MCA DLR, p. 11, 2009

[37] Dobbeck: Acceleration simulation in DS, p 15, 1974.

Human perception is subject to thresholds, like all sensors. Thus, humans do not perceive translational and rotational accelerations below those thresholds. Furthermore, the literature provides thresholds for rotational rate although the described principle of the vestibular organ (section 2.2.1) cannot be stimulated directly by constant rotational rate. The literature gives no further information about the perception principle of rotational rate. One possible explanation is the sensed change of position in the gravitational field due to pitch/roll rate or centripetal forces sensed by the proprioceptors and the macula due to a significant yaw rate. The thresholds found vary for individuals and depend on duration of exposure. The wide range of perception thresholds is emphasized by the values found in the literature as shown in Table 2.1. As Fischer[38] describes, the perception thresholds are usually used in DS studies according to applications of flight simulators. The thresholds described may be surpassed in some situations because they are dependent on the subject's expectations (brake dive etc.).[39,38] Fischer stresses that the dynamics in DS is increased compared to flight simulators as illustrated by the sudden acceleration change after strong braking into standstill or dynamic driving through an S-bend. Fischer suggests exceeding the limitations of human perception thresholds because some DS studies attest increased driving experience due to exceeded thresholds of tilt coordination.[40,41,42] Thus, the present work uses increased thresholds for the tilt coordination of 6°/s and 6°/s² according to the aforementioned references.

[38] Fischer: MCA DLR, p. 13, 2009.

[39] Reymond; Kemeny: Renault DS, 2000.

[40] Wentink et al.: Curve driving in a centrifuge, 2008.

[41] Fischer: MCA DLR, p. 70, 2009.

[42] cf. Nordmark: DS trends and experiences, 1994, according to Fischer: MCA DLR, p. 70, 2009

Table 2.1: Human perception thresholds for motion[43,44]

<table>
<tr><th></th><th colspan="3">Translational acceleration
in m/s²</th><th colspan="3">Rotational rate
in °/s</th><th>Rotational acceleration
in °/s²</th></tr>
<tr><td></td><td>$\ddot{x}$</td><td>$\ddot{y}$</td><td>$\ddot{z}$</td><td>$\dot{\varphi}$</td><td>$\dot{\vartheta}$</td><td>$\dot{\psi}$</td><td>$\ddot{\varphi}, \ddot{\vartheta}, \ddot{\psi}$</td></tr>
<tr><td>McConnel[45]</td><td colspan="3">0.18</td><td colspan="3">5</td><td>2</td></tr>
<tr><td>Clark and Steward[46]</td><td></td><td></td><td></td><td></td><td></td><td></td><td>4</td></tr>
<tr><td>Fogel[47]</td><td colspan="3">0.2</td><td></td><td></td><td></td><td></td></tr>
<tr><td>Richter[48]</td><td></td><td></td><td></td><td></td><td></td><td></td><td>5.73</td></tr>
<tr><td>Durth[49]</td><td colspan="3">0.18</td><td colspan="3">12</td><td>6</td></tr>
<tr><td>Reid and Nahon[50]</td><td>0.17</td><td>0.17</td><td>0.28</td><td>3.0</td><td>3.6</td><td>2.6</td><td></td></tr>
<tr><td>Nahon and Reid[51]
Nordmark[52]
Groen and Bles [53]</td><td></td><td></td><td></td><td colspan="3">3.0</td><td></td></tr>
<tr><td>Reymond et al.[54]</td><td></td><td></td><td></td><td colspan="3">2.04</td><td>0.3</td></tr>
<tr><td>Reymond et al.[55]</td><td>0.05</td><td></td><td></td><td></td><td></td><td></td><td>0.3</td></tr>
</table>

43 cf. Betz: Preliminary WMDS research, p. 11, 2010.

44 cf. Fischer: MCA DLR, p. 14, 2009.

45 cf. McConnel: Motion sensitivity, 1957, according to Tomaske, Design of DS, p. 15, 1983.

46 cf. Clark; Steward, Perception of angular acceleration, 1962, according to Tomaske, Design of DS, p. 15, 1983.

47 cf. Fogel, Biotechnology, 1963, according to Dobbeck, Acceleration simulation in DS, p 10-11, 1974.

48 Richter: Acceleration simulation in DS, p. 13-14, 1971.

49 cf. Durth: Driver-vehicle-road model, 1974, according to Tomaske, Design of DS, p. 15, 1983.

50 Reid; Nahon: Motion algorithm of flight simulators, 1985.

51 Nahon; Reid: MCA, 1990.

52 cf. Nordmark, DS trends and experiences, 1994, according to Fischer, MCA DLR, p. 14, 2009.

53 cf. Groen; Bles, Tilt in DS, 1994, according to Fischer, MCA DLR, p. 14, 2009.

54 cf. Reymond et al., Kinesthetic restitution in a DS, 1999, according to Fischer, MCA DLR, p. 14, 2009.

55 cf. Reymond et al., Validation of the Renault DS, 2000, according to Fischer, MCA DLR, p. 14, 2009.

2.3 Functional Elements of Driving Simulators

2.3.1 General Overview of Functional Elements

The functional elements are divided into four main groups as shown in Figure 2.6 according to Allen et al.[56]. Although the present work is focused on the motion system of DS, a brief introduction of the nexus of the overall DS is provided in the following subsections. The information from section 2.3.1 is according to Allen et al.[57] if not referenced differently.

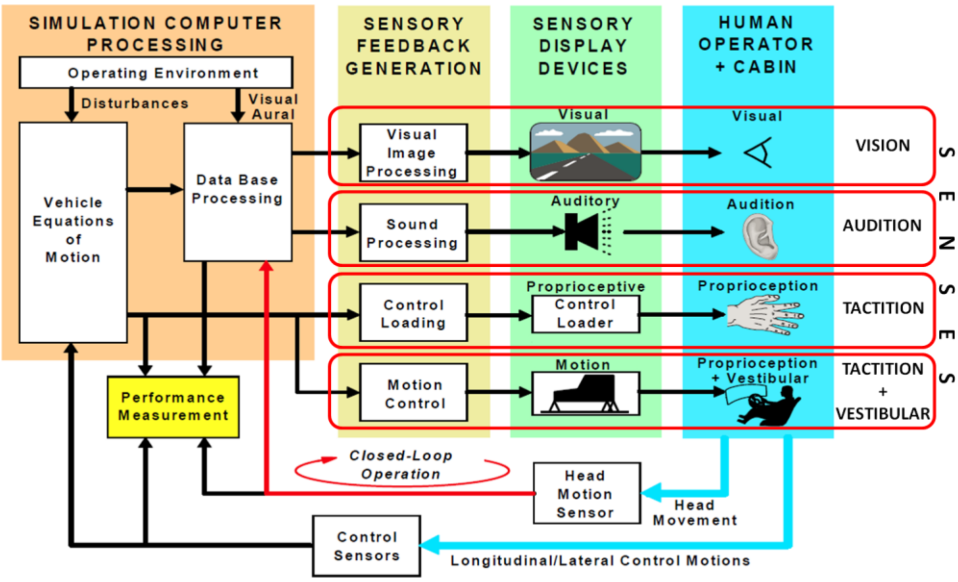

Figure 2.6: Functional elements of DS[58]

Simulation Computer Processing (SCP)

Simulation computer processing deals with the virtual elements of the DS, such as the operating environment and the vehicle dynamics. Those elements are mandatory for all kinds of DS. In order to provide a realistic driving experience to the subject, virtual elements must be linked according to physical constraints. Here, the vehicle motion must be calculated by the vehicle equations of motion regarding disturbances from the environment. The *operating environment* contains information like road properties and traffic objects. The next step in SCP is the *data base processing*. The environment must

[56] Allen et al.: History of DS, p. 2-2, 2011.

[57] Allen et al.: History of DS, 2011.

[58] cf. Allen et al.: History of DS, p. 2-2, 2011.

be represented from the aspect of the vehicle in order to provide plausible visual and auditory information for the subject. Thus, the vehicle's position and motion must be merged with the model of the environment.

The information generated in this manner is used in the next functional group (s*ensory feedback generation*) to create four different sensory feedbacks as follows.

Sensory Feedback Generation (SFG)

The driving experience is a composition of four different senses (cf. section 2.2):

- Vision
- Audition
- Tactition (also called proprioception)
- Vestibular

These senses must be fed with accurate information in order to provide a realistic driving experience. The cues must be generated according to the inputs from the previously described functional group (SCP). Thus, this functional group is called s*ensory feedback generation*.

The generated cues are used in the next functional group (s*ensory display devices*) to provide the cues' information to the subject as described in the following.

Sensory Display Devices (SDD)

The calculated cues must be performed according to human sensory perception.

- Vision: Visual representation using light in the human's visible light spectrum
  - Displays
  - Projectors and screens
- Audition: Auditory representation by speakers using human's audible frequencies
  - Speakers
- Tactition: Proprioceptive stimulation by contact forces
  - Shaker
    - Seat vibration
    - Steering wheel vibration
    - Pedal pulsation
  - Loading
    - Steering wheel torque
    - Wind (for motorcycles etc.)
- Vestibular: Motion in six DOF
  - Hexapod
  - Sledge/rail system
  - Gimbaled system
  - Self-propelled motion systems

The created stimulations are used in the next functional group (*Human Operator + Cabin*) to create the subject's driving experience as follows.

Human Operator + Cabin (HOC)

Now that the sensory stimulation has been provided, the subject perceives the driving experience as calculated in the SFG. The driving experience allows the subject to interact properly with the virtual elements – the vehicle itself and the environment. The goal is to generate a valid subject behavior while keeping the hardware expenditures as low as possible due to costs and mass.

Summary of Functional Elements

The quality of the functional elements has improved greatly over the past decades. Beside the technical improvements, costs of many elements have dropped due to the cost decline of computing power. As mentioned before, the most significant hardware costs arise from the motion system and the DS cabin.[59] Thus, the focus of this work deals with a costly part of the DS and aims for reducing DS costs significantly.

2.3.2 Motion System

The basic strategy for providing acceleration within a limited workspace is the utilization of human perception thresholds for motion. The translational acceleration simulation of DS is based on two principles – tilt coordination and translational motion itself. The missing yaw acceleration is superimposed by rotating the subject around its vertical axis.

Principles of Translational Acceleration Simulation

As described in section 2.2, utilizing tilt coordination is limited to a maximum angle of about 20° to 30° and the thresholds summarized in Table 2.1. Due to the described limitations, the tilt principle is strongly restricted in its usable dynamics and cannot perform high-frequency changes of horizontal acceleration simulation. Hence, DS utilizing only tilt coordination for acceleration simulation cannot provide transient motion cues as they occur in the real world.

The translational motion uses horizontal accelerations of the DS cabin. In contrast to tilt coordination, this principle is suitable for the performance of high-frequency acceleration cues. As a result of the performed acceleration cues, the DS must conduct corre-

[59] Allen et. al.: History of DS, p. 2-4, 2011.

sponding velocity and displacement cues. For long-lasting (e.g. low-frequency) accelerations, the corresponding cues lead to great workspace demand, especially when combined with high amplitude. Thus, a DS cannot solely utilize the translational principle. The advantage arises when the tilt coordination and translational principle are combined. The resulting translation-tilt-system now allows the performance of short-term, high-frequency acceleration cues as well as long-lasting, continuous ones. Limitations now arise from constraints like available workspace and further technical specifications of the DS, such as maximum velocity and peak acceleration performance.

Some references introduce circular motion as independent principle to perform acceleration.[60,61] Indeed it must be emphasized that circular motion does not represent another principle because it is a translational motion that is combined with yaw rate of the DS dome. Utilizing yaw rate continuously represents the only difference to the previously introduced principle of translational motion. In the author's point of view, circular motion is a special application of the translation principle and also benefits from superimposing tilt coordination. The application of continuous yaw rate is subject to several constraints as discussed in Dobbeck[60]. The occurring tangential, radial, and Coriolis accelerations are strongly coupled. The implementation of continuous yaw rate takes place at the software level as introduced later in section 2.4 (motion cueing algorithm).

Because of the constraints which were introduced, dynamic DS as they are used in research and development all utilize combined tilt-translation systems. Various DS setups came into being – all impaired by the same physical constraints – as discussed in the following.

Hardware of Combined Tilt-Translation Systems

The most common motion system for DS is the hexapod (also Stewart platform)[62]. The hexapod is a compact tilt-translation system that offers 6 DOF motion. The DOFs are actuated using six identical linear actuators (electric, hydraulic or pneumatic). As presented in Figure 2.7, the actuators are mounted between the fixed base frame and the upper platform that has to move. The mounting is realized by bearings that provide two rotational DOF (universal joint) in order not to impede the unambiguous 6 DOF motion.

---

[60] Dobbeck: Acceleration simulation in DS, p 18-27, 1974.

[61] Richter: Acceleration simulation in DS, p. 157, 1971.

[62] Stewart: Hexapod, 1966.

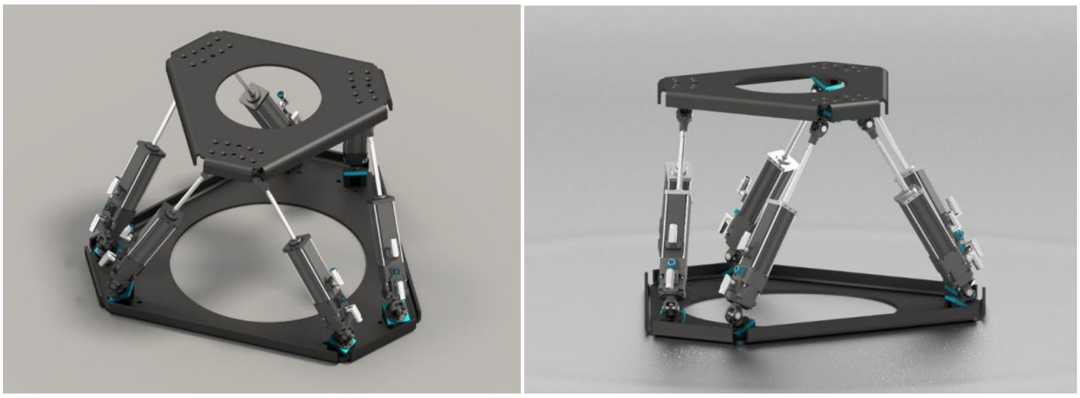

Figure 2.7: CAD model of a hexapod[63]

Real-world vehicle motion also consists of 6 DOF. However, surge (x-direction), sway (y-direction) and yaw (rotation about z-axis, ψ) have unlimited stroke, whereas pitch (rotation about y-axis), roll (rotation about x-axis) and heave (z-direction) show high-frequency behavior with strongly limited stroke. The motion simulation of the unlimited vehicle surge, sway and yaw easily exceeds the physical limits of hexapod systems, which are constrained by the workspace. In contrast, the limited pitch, roll and heave motion are adequately executable by hexapod systems. The stroke of the linear actuators limits the hexapod's motion capability for surge, sway, and yaw. Big systems, as they are often used in DS, reach translational workspace of about 2 m.[64,65,66] The workspace constraint causes system limitations with respect to the performable acceleration cues. While most of the acceleration peak values that occur in real-world driving can be performed by hexapods, the workspace restriction does not allow for sufficient long-lasting acceleration simulation (e.g. low-frequency). The following example describes the limitations between the acceleration amplitude and the cueing frequency:

Within a workspace providing b to each side and a desired harmonic excitation with the maximum acceleration amplitude of $\hat{a}_{\mathrm{max}}$ the minimum excitation frequency is derived:

$$f_{\mathrm{trans}} = \frac{\sqrt{\hat{a}_{\mathrm{max}}/b}}{2\pi} \tag{1}$$

With $b = 1\ \mathrm{m}$ and $\hat{a}_{\mathrm{max}} = 5\ \mathrm{m/s^2}$ the critical frequency becomes $f_{\mathrm{trans}} = 0.37\ \mathrm{Hz}$. The described harmonic excitation task can be performed by translational motion for

[63] MEVEA – virtual: Hexapod, last access January 14th 2014.

[64] Greenberg et al.: Lateral motion cues, 2003.

[65] Murano et al.: Toyota DS, 2009.

[66] Suikat: DLR DS, 2005.

frequencies above the calculated critical frequency. In order to demonstrate the behavior for low-frequency acceleration cues, the exemplarily chosen acceleration of 5 m/s² is maintained. The example provides a workspace of 2 m; 1 m acceleration path and the remaining 1 m as deceleration path. Within this workspace, the exemplarily chosen acceleration of 5 m/s² can be performed for only 0.63 s. The long-lasting acceleration cues must be performed by tilt coordination as described previously, but tilt coordination is also restricted due to the human perception thresholds for rotational motion. The critical frequencies for rotational motion become (derivation see appendix A):

$$f_{\mathrm{rot},\dot{\varphi}} = \frac{g}{2\pi \hat{a}_{\mathrm{max}}} \dot{\varphi}_{\mathrm{limit}} \tag{2}$$

$$f_{\mathrm{rot},\ddot{\varphi}} = \frac{\sqrt{g/\hat{a}_{\mathrm{max}} \cdot \ddot{\varphi}_{\mathrm{limit}}}}{2\pi} \tag{3}$$

With the values introduced previously, the following critical frequencies appear: $f_{\mathrm{rot},\dot{\varphi}} = 0.016$ Hz and $f_{\mathrm{rot},\ddot{\varphi}} = 0.072$ Hz. The described harmonic excitation task can be performed by tilt coordination for frequencies below the calculated critical frequency. For the constraints of the exemplarily chosen hexapod system, combining both principles – translational motion and tilt coordination – does not allow the performance of the described task in a frequency range of 0.016 Hz to 0.37 Hz. A gap of about 4.5 octaves is left that is impaired by strongly limited acceleration simulation. The only solution to solve the problem is to increase the workspace. For performing the exemplary task at all frequencies using a tilt-translation system, b ≈ 495 m is required. The resulting frequency gaps are illustrated exemplarily in Figure 2.8.

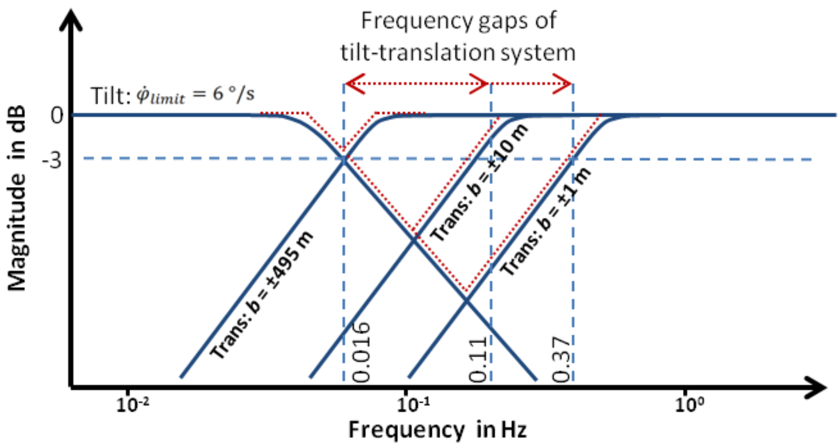

Figure 2.8: Frequency gaps of exemplarily chosen tilt-translation systems according to equations (1) and (2)

In order to fulfill the increased requirements caused by urban traffic simulation, supplementary actuated subsystems must be added to the hexapod – additional DOF are the consequence (Figure 1.2, p. 3). The enhanced tilt-translation system is supposed to solve the deficit of the strongly limited translational workspaces of hexapods. Thus, sledges are mounted underneath the hexapod resulting in the significant increase of moved mass. Existing DS show setups utilizing one or two additional sledges. The systems reach workspaces up to 35 x 20 m[67], which lead to moved masses of about 80 t[68]. The increased complexity results in significantly rising purchase, operating and maintenance costs. As introduced with the exemplary harmonic excitation task, even those enhanced tilt-translation systems are strongly limited. Further details concerning existing DS setups are presented in section 2.5. The hardware necessary to perform motion cues has thus been discussed in detail. The open question remains as to how the motion cues are generated. The generation takes place in the *sensory feedback generation* (Figure 2.6, p. 17) within the area of motion control. The following section introduces state-of-the-art motion cueing algorithms.

2.4 Motion Cueing Algorithm (MCA)

The DS task is to provide various driving experiences to a subject within the workspace of the simulator system. Because real-world driving is meant to travel distance, real-world motion requires much workspace. In order to conduct such driving tasks in a DS, a motion transformation is required that reduces performed motion. The MCA accomplishes this transformation and is a vital software element of dynamic DS. It must transform the vehicle dynamics (driver-felt accelerations) of the virtual car into the motion task of the DS as shown in Figure 2.9. The motion task of the DS is composed of the motion of the wheeled platform and the tilt coordination of the cabin. This task is subject to several constraints depending on the available DOF of the DS and their specifications.

[67] Murano et al.: Toyota DS, 2009.

[68] Clark et al.: NADS Motion system, 2001.

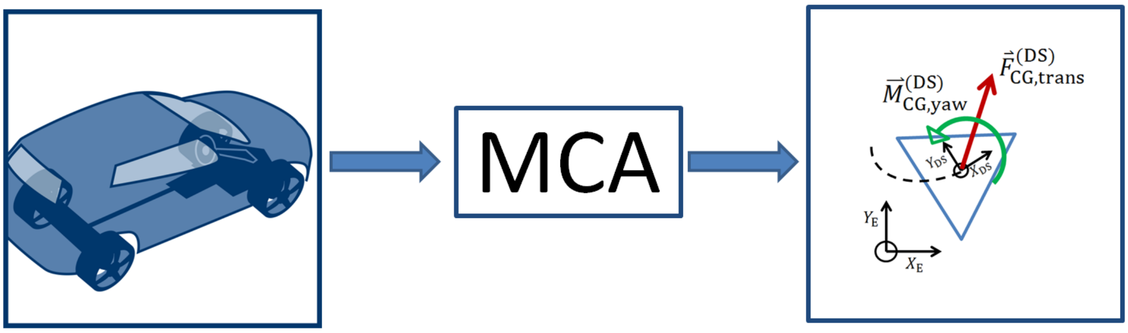

Figure 2.9: Transformation from vehicle dynamics into DS dynamics

Because no existing DS provides sufficient workspace to perform the driving experience 1:1, as described in section 1.1, the common MCA[69] filter the critical frequencies from the overall acceleration task. Different approaches are used in order to do so. The MCA must be able to take advantage of the system-immanent motion capability of the DS used.

This work is not intended to bring about improvements in terms of exploitation of the workspace, as most research in this field does, but aims for frequency-independent motion simulation in order to improve the driving experience (see Figure 2.8). Furthermore, tuning transparency is demanded because the present work is focused on comprehensibility to investigate the general feasibility of the new DS concept.

A variety of MCA are known today. Most MCA are based on the three so called classical algorithms: the classical washout, the optimal control, and the coordinated adaptive algorithm. The summary of these commonly used MCA is based on the dissertation of Fischer[70]. He comprehensively reviews the research that was done for the above mentioned MCA[71,69,72].

2.4.1 Classical Washout (CW)[70]

The CW has a translational path and a rotational one as shown in Figure 2.10. All processing steps in the CW are time invariant. The transparency of the filter parameters is high because they can be described analytically. Depending on the order and the parameterization of the filters, a complementary tuning is possible that allows for frequency independent acceleration simulation.

---

[69] Nahon; Reid: MCA, 1990.

[70] Fischer: MCA DLR, p. 27-40, 2009.

[71] Reid; Nahon: Motion algorithm of flight simulators, 1985.

[72] cf. Grant: Motion algorithm of flight simulators, 1995, according to Fischer: MCA DLR, p. 27, 2009.

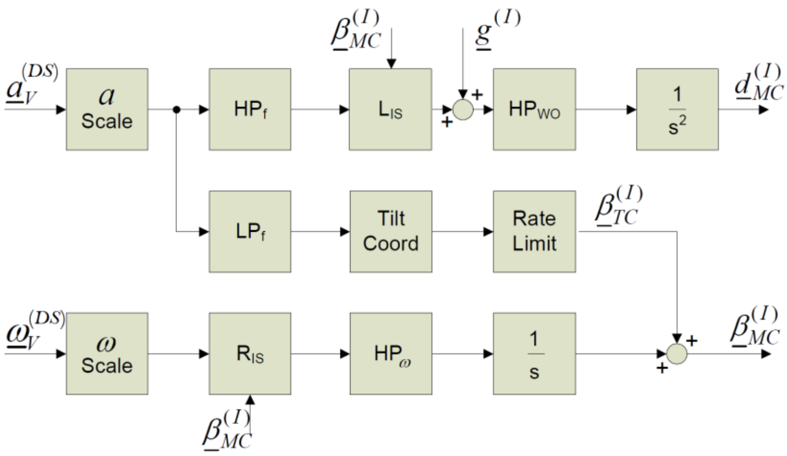

Figure 2.10: Block diagram of the CW[73]

The inputs into the translational path are three translational accelerations of the virtual vehicle ($\underline{a}_{\mathrm{V}}^{(\mathrm{DS})}$). The first processing scales and limits the inputs. The scaling is done by a constant factor that is parameterized according to the focus of the test drives and the performance specifications of the motion system used. The limitation is a nonlinear process that mainly focuses on the performance specifications of the DS, because there is no use in demanding more amplitude than the system can provide. After restricting the inputs, a frequency-sensitive splitting is done in order to determine the shares of the acceleration cues that are suitable for the translational motion system (high-pass filter (HP): $\mathrm{HP_f}$) and the tilt coordination (low-pass filter (LP): $\mathrm{LP_f}$). The high-frequency translational path then needs to be transformed by a rotation matrix ($\mathrm{L_{IS}}$) in order to calculate the translational acceleration task of the DS with respect to the inertial COS (I). After adding gravity, another high-pass filter is applied ($\mathrm{HP_{WO}}$) that causes the return to the initial DS position (washout). The position cue ($\underline{d}_{\mathrm{MC}}^{(\mathrm{I})}$) is finally derived by integrating twice ($1/s^2$).

The already filtered, low-frequency share of the acceleration cues ($\mathrm{LP_f}$) is processed in the tilt coordination to corresponding pitch and roll angle cues with respect to the inertial COS ($\underline{\beta}_{\mathrm{TC}}^{(\mathrm{I})}$). The rate limiter ensures that the previously introduced human perception thresholds for rotational rates are retained. This rate limiter again represents a nonlinear processing. The calculated orientation of the tilt coordination ($\underline{\beta}_{\mathrm{TC}}^{(\mathrm{I})}$) is finally added to the results of the rotational path and determines the final platform orientation ($\underline{\beta}_{\mathrm{MC}}^{(\mathrm{I})}$).

---

[73] cf. Fischer (According to Reid; Nahon, Motion algorithm of flight simulators, 1985 und Nahon; Reid, MCA, 1990): MCA DLR, p. 29, 2009.

The rotational path is treated similarly to the translational one. After the scaling and limitation of the rotational input ($\underline{\omega}_V^{(DS)}$) an elementary rotation matrix (R_{IS}) is applied to transform the angles into the inertial COS. The following high-pass filter (HP_ω) separates the share of the rotational rates that can be performed by the tilt system within its workspace. The rotational orientation is derived by integration.

Lastly, it is emphasized that the transparency and the frequency independency of the CW meet the aforementioned demands for the WMDS research of the present work. Therefore, this MCA is of interest for the present work and the developed "ideal" MCA in section 3.2.

2.4.2 Optimal Control[74]

The basic structure of the algorithm of optimal control is similar to the CW. As with the CW, all processing steps are time invariant. The input into the rotational path differs, because absolute angles ($\underline{\beta}_V^{(DS)}$) are used here instead of rotational rates. Thus, the transformation between the simulator's and inertial COS is unnecessary. Another difference is the use of weighting functions (W_{ij}) instead of the tilt coordination and the filter elements. Compared to the CW, an additional path is added that links the rotational input to the translational accelerations.

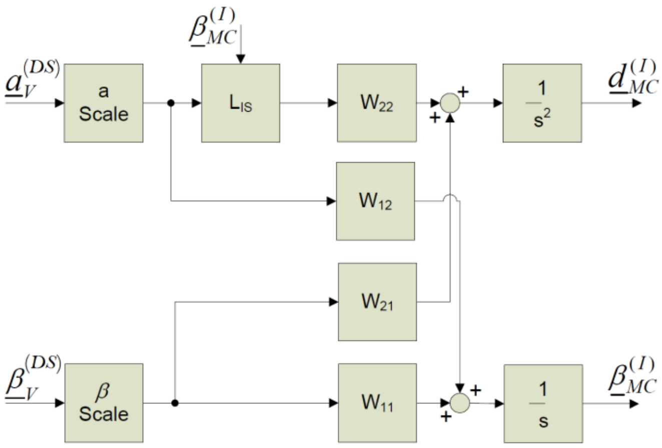

Figure 2.11: Block diagram of the algorithm of optimal control[75]

The weighting functions represent transfer functions of higher order or can be simplified due to typical coupling or signal properties according to Table 6.1 (Appendix B, p. 126). The major disadvantage for the application in the present work is that the tuning of this

[74] Fischer: MCA DLR, p. 27-40, 2009.

[75] cf. Fischer (According to Reid; Nahon, Motion algorithm of flight simulators, 1985 und Nahon; Reid, MCA, 1990): MCA DLR, p. 29, 2009.

algorithm is more complicated compared to the CW because the transparency of the parameters is lost. The tuning is done by a human perception model that helps in determining the perception error as shown in Figure 6.1 (Appendix B, p. 126). The tuning takes place offline using cost function optimization.

In conclusion, it must be underscored that the loss of transparency of this MCA is a major disadvantage for the focus of the present work. Hence, it is not considered for the WMDS research of the present work. Furthermore, the tuning by cost functions makes it more difficult to provide a frequency-independent acceleration simulation. Nevertheless, the algorithm of optimal control can be used for operating a WMDS and might provide better usage of the given workspace. For the present work, however, this advantage is subordinate to comprehensibility. Comprehensibility is of great importance in order to facilitate the general feasibility analysis of the WMDS concept. For further details concerning the optimal control algorithm and its optimization, see Fischer[76], Telban[77], and Telban et al.[78].

2.4.3 Coordinated Adaptive[76]

The algorithm of the coordinated adaptive represents a combination of the two previously introduced algorithms. As shown in Figure 2.12, the structure is similar to the CW but the filters used are adaptive and thus, time variant. The tuning of the filters takes place during operation. The optimization is achieved by cost functions as for the optimal control algorithm, but the application of human perception models is unusual. Tilt coordination is integrated in the adaptive filter of the rotational path (Adpt. Filter #2).

---

[76] Fischer: MCA DLR, p 27-40. 2009.

[77] cf. Telban: Nonlinear MCA, 2002, according to Fischer: MCA DLR, p. 29-30, 2009.

[78] cf. Telban et al.: Nonlinear human-centered MCA, 2002, according to Fischer: MCA DLR, p. 29-30, 2009.

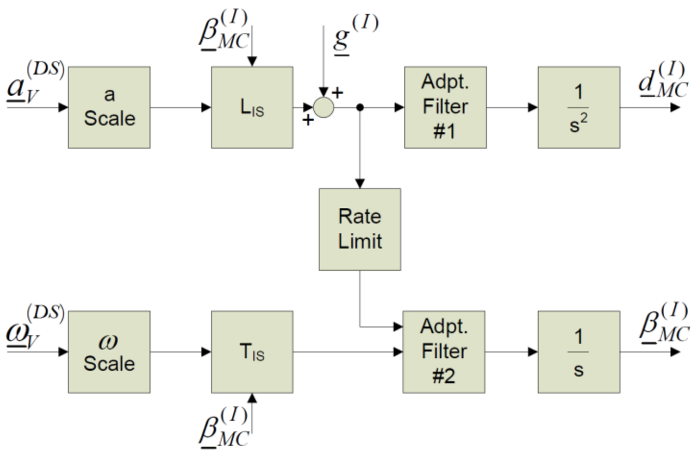

Figure 2.12: Block diagram of the algorithm of coordinated adaptive [79]

The exclusion of this algorithm is in accordance with the justification of the previous algorithm (section 2.4.2). For further details concerning this algorithm and its tuning, see Grant and Naseri.[80]

2.4.4 Further Optimization Approaches

In addition to the three introduced classical algorithms (sections 2.4.1 to 2.4.3), further approaches for optimization exist. A comprehensive overview is presented in Fischer[81]. One of the approaches is of great interest for this work as it uses complementary filters for providing a frequency-independent driving experience[82]. The idea is to tune the utilized LP-filter and HP-filter complementarily (translational path and tilt coordination). As a result, the sum of both filter outputs equals the original filter input. Thus, no frequency-dependent filter effect appears and a 1:1 driving experience is enabled. According to Fischer[83] this is possible for first order filters only. Alternative to complementary filters, the same effect is achieved when using only one LP-filter (tilt coordination) and subtracting the filter output from the original signal as proposed by Murano et al.[84]. The general problem of frequency-independent MCA is the significant increase of workspace demand as introduced in section 2.3.2 (example of harmonic excitation for all frequencies by a tilt-translation system: $\hat{a}_{\max} = 5\ \mathrm{m/s^2}$, ±495 m). If the increased workspace demand cannot be coped with by the available DS, a loss in quality of the

[79] cf. Fischer (According to Reid1985 und Nahon1990): MCA DLR, p. 31, 2009.

[80] cf. Grant; Naseri: adaptive MCA, 2005, according to Fischer: MCA DLR, p. 31, 2009.

[81] Fischer: MCA DLR, p. 32-39, 2009.

[82] Sammet: MCA, 2007.

[83] Fischer: MCA DLR, p. 33, 2009.

[84] Murano et al.: Toyota DS, 2009.

created driving experience must be accepted: Fitting the DS motion to the available workspace must be done by scaling the motion cues or increasing the limits for tilt coordination. Because the WMDS analysis is not limited to common workspace of DS, this optimization approach is suitable for taking advantage of the system-immanent motion capability of WMDS. Hence, this optimization is considered in the development of the "ideal" MCA later introduced in section 3.2.

2.5 State-of-the-Art Driving Simulators

This section introduces the most advanced tilt-translation systems. The focus is on DS with enhanced motion systems, as this work mainly treats acceleration simulation. The information in this section shows that the cost-benefit ratio of state-of-the-art DS has a progressive characteristic due to physical constraints. Hence, advanced state-of-the-art DS are not widely used due to economic considerations. The work of scientific institutes is impaired most by the significant costs. The introduced systems are summarized in Table 2.2.

Table 2.2: Overview of introduced DS systems

Organization	Workspace	DOF	Moving mass
Peugeot Société Anonyme (PSA)[85]	10 m x 5.5 m	8 DoF	UNK
University of Iowa[86]	20 m x 20 m	12 DoF	80 t
Toyota[87]	35 m x 20 m	12 DoF	80 t[88]
Daimler[89]	12.5 m	7 DoF	UNK
Research Institute of Automotive Engineering and Vehicle Engines Stuttgart (FKFS)[90]	10 m x 7 m	9 DoF	UNK

[85] Chapron; Colinot: PSA DS, 2007.

[86] Clark et al.: NADS motion system, 2001.

[87] Murano et al.: Toyota DS, 2009.

[88] Iwazaki; Yonekawa – expert discussion: Toyota DS, 2013.

[89] Schöner – expert discussion: Daimler DS, 2014.

[90] Baumann et al.: DS of Stuttgart University, 2012.

2.5.1 PSA DS[91]

The PSA DS is composed of two sledges and an electrical hexapod, both systems delivered by Bosch Rexroth. The hexapod is a 1000 kg payload system. The motion specifications are smaller than the ones of the following state-of-the-art DS systems. This system is introduced because of its well presented mass distribution of the dome components as shown in Figure 2.13. The dome comprises a half-vehicle cab, a visual system (projectors), vehicle standard equipment, feedback systems and a composite honeycomb structure. In total, the dome mass amounts to 720 kg. The presented setup is important for the present work because its mass information is transferred to the WMDS mass estimation[92]. The specifications of the whole motion system as it is presented in Figure 2.14 are presented in Table 2.3.

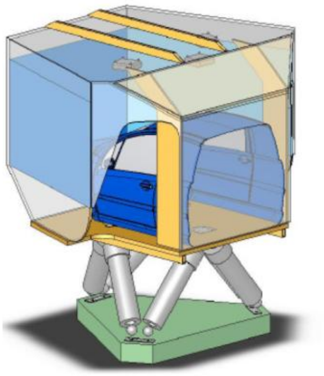

Major cell component	Weight (kg)
Visual system (projectors etc..) including retrovision	30
Composite honeycomb structure	250
Fixation devices, bushings	40
Vehicle cab (body shell)	160
Vehicle standard equipment (dashboard, seats etc..)	150
Acoustic reduction material	30
Passive force feedback system	30
Steering wheel feedback system	20
Total	**720**

Figure 2.13: Distribution of mass of the cabin of the PSA DS[91]

Figure 2.14: Picture of the PSA DS[91]

[91] Chapron, Colinot: PSA DS, 2007.

[92] Betz et al.: Motion analysis of WMDS, 2012.

Table 2.3: Specifications of the motion system of the PSA DS[93]

		Max stroke	**Max velocity**	**Max acceleration**	P_{peak}	$P_{continuous}$
		m, deg	m/s, deg/s	m/s², deg/s²	kW	kW
XY-System	X	±5	±3	±5	UNK	UNK
	Y	±2.75	±3	±5		
Hexapod	X	UNK	UNK	UNK	UNK	UNK
	Y	UNK	UNK	UNK		
	Z	±0.2	±2	±5		
	Pitch	±18	±20	±300		
	Roll	±18	±20	±300		
	Yaw	±23	±30	±600		
Turntable	Yaw	DNE	DNE	DNE	DNE	DNE
Shaker	Z	DNE	DNE	DNE		
	Pitch	DNE	DNE	DNE	DNE	DNE
	Roll	DNE	DNE	DNE		

2.5.2 NADS, University of Iowa

The *National Advanced Driving Simulator* (NADS) of the University of Iowa has a 12 DOF motion system. The information presented here is from Clark et al.[94], if not referenced differently. When introduced in 2001, it was the most advanced DS setup in the world. Figure 2.15 illustrates the DS setup. The goal of the NADS simulator is to conduct human factors research of crash avoidance. The most important enhancement is the XY system that extends the horizontal workspace significantly. Beside the sledges, a customized hexapod, a turntable and a shaker is used. The known motion specifications of the DS are summarized in Table 2.4. According to Clark, the specifications are based on maximizing the motion capacity for a given budget.[94] The horizontal workspace provides 20 x 20 m. The cumulative moving mass for the base sledge is 80 t. The sledges are driven by metal belts that are operated with metal drums in order to provide a stiff drive path. While the XY system is driven by electric motors, hydraulics is used for the hexapod, the turntable and the shaker. The NADS is the most advanced DS that is operated at a scientific institute. It still provides the biggest workspace of all known DS worldwide, while the acceleration performance is exceeded by the Daimler DS (section

[93] cf. Chapron, Colinot: PSA DS, 2007.

[94] Clark et al.: NADS motion system, 2001.

2.5.4). The costs of the NADS increased from an original estimate of 36.5 million US $ to a final amount of 80.8 million US $.[95]

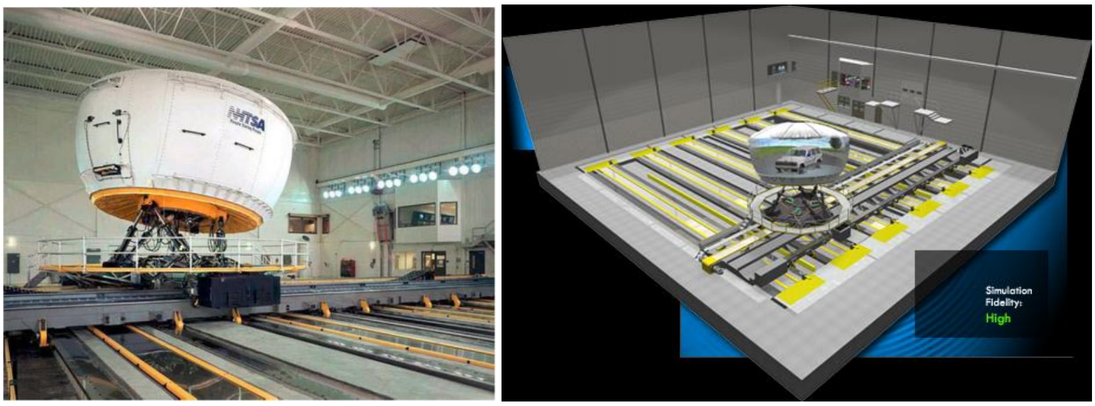

Figure 2.15: Picture of the NADS system (left[96], right[97])

Table 2.4: Specifications of the motion system of the NADS[98]

		Max stroke	**Max velocity**	**Max acceleration**	P_{peak}	$P_{continuous}$
		m, deg	m/s, deg/s	m/s², deg/s²	kW	kW
XY-System	X	±10	±6.1	±6.1	4,500	1950
	Y	±10	±6.1	±6.1		26 x 75 kW
Hexapod	X	UNK	UNK	UNK	1,100[99] for operating hydraulics	
	Y	UNK	UNK	UNK		
	Z	±0.6	±1.5	±10		
	Pitch	±25	±45	±120		
	Roll	±25	±45	±120		
	Yaw	UNK	UNK	UNK		
Turntable	Yaw	±330	±60	±120		
Shaker	Z	±0.05	±0.16	±4.9		
	Pitch	UNK	UNK	UNK		
	Roll	UNK	UNK	UNK		

[95] Stefani: Cost increase of NADS, 2001.

[96] NADS – virtual: NADS Overview 2010, Last access: January 14th 2014.

[97] NADS – virtual: Homepage, Last access: January 14th 2014.

[98] cf. Clark et al.: NADS motion system, 2001.

[99] The reference does not clarify if the value is peak or continuous power.

2.5.3 Toyota

Toyota has developed a DS that is similar to the NADS system in Iowa. The information presented here about the Toyota system is from Murano et al.[100], if not referenced differently. The specifications of the motion system are presented in Table 2.5. The specifications for the XY system were determined by experiments at the NADS. Toyota's goal is to provide real-world driving experience up to 0.3 *g* and at least 4 Hz according to their information about ordinary driving (appendix C.1: Figure 6.2 and Figure 6.3). The dome has a height of 4.5 m and an inner diameter of 7 m. The delay of the visual rendering is 63 ms.

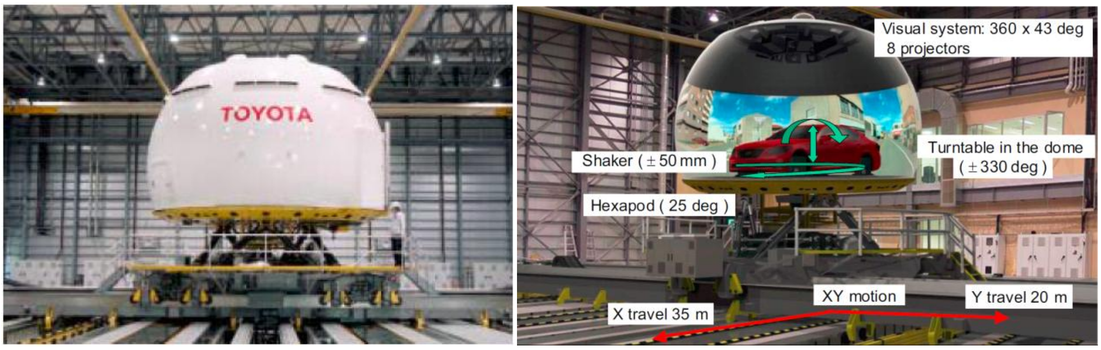

Figure 2.16: Pictures of the Toyota DS[101]

[100] Murano et al.: Toyota DS, 2009.

[101] Murano et al.: Toyota DS, 2009.

Table 2.5: Specifications of the motion system of the Toyota DS[102]

		Max stroke	Max velocity	Max acceleration	P_{peak}	$P_{continuous}$
		m, deg	m/s, deg/s	m/s², deg/s²	kW	kW
XY-System	X	±17.5	±6.1	±4.9	ca. 2,390[103]	UNK
	Y	±10	±6.1	±4.9		
Hexapod	X	±0.7	±1	±4.9	UNK	UNK
	Y	±0.66	±1	±4.9		
	Z	±0.6	±1	±9.8		
	Pitch	±25	±45	±120		
	Roll	±25	±44	±120		
	Yaw	±25	±44	±120		
Turntable	Yaw	±330	±60	±120	UNK	UNK
Shaker	Z	±0.05	±0.16	±4.9	UNK	UNK
	Pitch	±2	±2	±197		
	Roll	±3.88	3.88	±381		

2.5.4 Daimler

The new Daimler DS was put into operation in 2010. It is a fully new development of the previous DS system that was made public in 1985 for the first time. The information presented here about the Daimler system is from Zeeb[104], if not referenced differently. The hydraulic concept is substituted by an electrical drive system. The DS setup is presented in Figure 2.17. One of the major goals of the new DS is the application in driving dynamics up to 1 g of acceleration for 1:1 scaled experiments[105]. According to Zeeb, this goal is not realized for extended XY sledge systems similar to the NADS or Toyota systems, due to the tremendous increase in technical and financial effort. These enhanced XY systems are encumbered by physical limitations due to high moving mass. Thus the Daimler DS utilizes a single sledge. The linear slide is realized by frictionless air bearings. The sledge is actuated by a short stator linear motor with a maximum force of 212 kN. An electric hexapod is mounted on top of the sledge. The specifications of the motion system are found in Table 2.6. The mock-up is a full car. Similar to the PSA

[102] cf. Murano et al.: Toyota DS, 2009.

[103] Estimation according to available information and expert discussion with Toyota: $80{,}000\,\mathrm{kg}\cdot 4.9\,\frac{\mathrm{m}}{\mathrm{s}^2}\cdot 6.1\,\frac{\mathrm{m}}{\mathrm{s}} = 2{,}390\,\mathrm{kW}$. Information about moved mass according to Iwazaki and Yonekawa 2013.

[104] Zeeb: Daimler DS, 2010.

[105] Due to the limited workspace, highly dynamic test maneuvers are only possible for special maneuvers such as slalom and lane change because the lateral trajectory of the virtual vehicle can be performed 1:1 by the available rail system.

system, the mock-up can be mounted in parallel or perpendicular to the sledge for experiments treating longitudinal or lateral dynamics. The dome has an inner diameter of ca. 7.5 m and a height of ca. 4.5 m. The system is of interest for the present work because it is the DS providing the greatest acceleration performance among the presented systems – up to about 1 *g*. The costs of the Daimler DS are stated to be approx. 40 million €.[106]

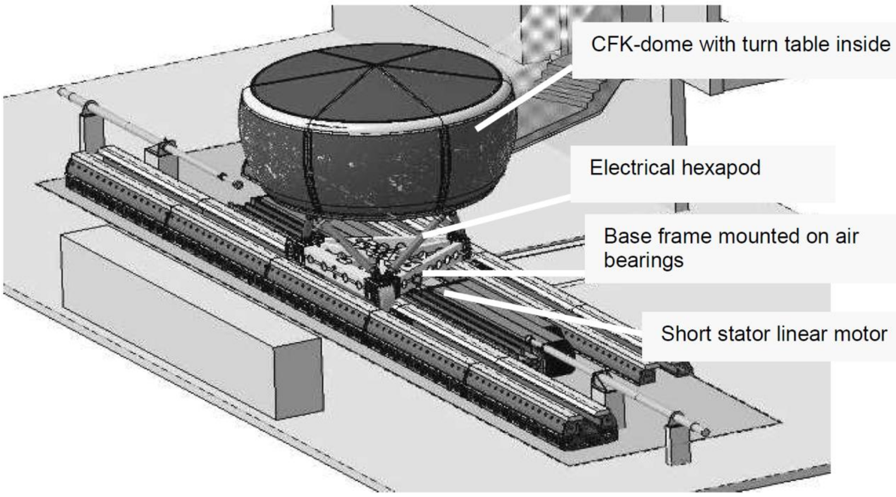

Figure 2.17: Illustration of the Daimler DS[104]

Table 2.6: Specifications of the motion system of the Daimler DS[107]

		Max stroke	**Max velocity**	**Max acceleration**	P_{peak}	$P_{continuous}$
		m, deg	m/s, deg/s	m/s², deg/s²	kW	kW
XY-system	X | Y	±6.25	±10	±10	2000	1500
Hexapod	X	+1.5	±1.2	±10	250	150
	Y	±1.1	±1.2	±10		
	Z	±1	±1.2	±10		
	Pitch	+24	±80	±250		
	Roll	±20	±80	±250		
	Yaw	±38	±80	±250		
Turntable	Yaw	0 | 90	0	0	0	0
Shaker	Z	DNE	DNE	DNE	DNE	DNE
	Pitch	DNE	DNE	DNE		
	Roll	DNE	DNE	DNE		

[106] Weber – virtual: Daimler DS, last access: February 13th 2014.

[107] Schöner – expert discussion: Daimler DS, 2014.

2.5.5 FKFS, Stuttgart

The Research Institute of Automotive Engineering and Vehicle Engines Stuttgart (FKFS) has built the largest DS that is operated at a European research institute.[108] The construction is the most recent DS and is still based on the conventional rail guided principle. This recent effort proves the ongoing trend of the physically limited state of the art. The system utilizes a hexapod and two rail systems as shown in Figure 2.18. The technical specifications of the motion system are listed in Table 2.7. The costs of the FKFS DS make up the biggest share of the overall project budget of 3.7 million €.[109]

Figure 2.18: CAD drawing of the FKFS DS[110]

[108] FKFS – virtual: FKFS DS, 2010.

[109] FKFS – virtual: FKFS DS, 2011.

[110] FKFS – virtual: FKFS DS, 2010.

Table 2.7: Specifications of the motion system of the FKFS DS[111]

		Max stroke	**Max velocity**	**Max acceleration**	$\boldsymbol{P_{peak}}$	$\boldsymbol{P_{continuous}}$
		m, deg	m/s, deg/s	m/s², deg/s²	kW	kW
XY-System	X	±5	2[112]	±5	UNK	UNK
	Y	±3.5	3[112]	±5		
Hexapod	X	+0.54[112]	UNK	±5	UNK	UNK
	Y	±0.45[112]	UNK	±5		
	Z	+0.38[112]	UNK	UNK		
	Pitch	±18.7[112]	UNK	UNK		
	Roll	+18.3[112]	UNK	UNK		
	Yaw	±21.5[112]	UNK	UNK		
Turntable	Yaw	DNE	DNE	DNE	DNE	DNE
Shaker	Z	DNE	DNE	DNE	DNE	DNE
	Pitch	DNE	DNE	DNE		
	Roll	DNE	DNE	DNE		

2.5.6 Conclusion on State-of-the-Art DS

None of the introduced DS is capable of performing the very basic T-junction maneuver[113] that has been introduced in the motivation (section 1.1). The main restriction results from the limited workspace of state-of-the-art DS. In the performance of this single maneuver, the quality of the created driving experience is necessarily affected by scaling factors and violation of the human perception thresholds. The consequences for the validity of the DS study are difficult to predict and have been only sparsely researched.[114,115] If more complex test cases such as combined urban traffic maneuvers that are strung together are also considered, there is a rapid widening of the gap between state-of-the-art DS performance and required workspace as presented later in section 5.2.1.

Comparisons of motion performance in terms of peak acceleration and workspace to project costs of the NADS[116], Daimler[117] and FKFS[118] systems reveal that the cost-

[111] Baumann et al.: DS of Stuttgart University, 2012.

[112] According to the Bosch Rexroth E-Motion 4000 (8DOF) system www.boschrexroth.de, last access: January 19th 2014.

[113] Estimated Workspace demand for unscaled T-junction maneuver: ca. 50x140 m².

[114] Blaauw: Validity of DS, 1982.

[115] Zöller et al.: Validity of DS, 2013.

[116] NADS: 20 x 20 m², $a_{\max} = 6.1\ \mathrm{m/s^2}$, 80.8 million US $.

benefit ratio is highly progressive as already implied by Zeeb[119]. Therefore, economic boundaries are easily exceeded when accomplishing increased DS performance demands by state-of-the-art technology. Concluding, it must be stressed that a new motion system for DS is required that enables the extension of workspace while keeping highly dynamic performance at reasonable cost.

2.6 Wheeled Motion Bases

2.6.1 BMW Patent[120]

Donges[120] provides the first description of a WMDS. The system is described as a carrier platform having at least three drive units with single or twin wheels as presented in Figure 2.19. The wheels provide maximum steer angles of ±180°. The platform creates at least horizontal motion for the subject sitting in a vehicle that can be carried out as a mock-up or real vehicle. The safety architecture of the DS is described as an element of the infrastructure limiting the workspace by safety fences that are located at the walls of the horizontal workspace. Further details concerning the motion platform, its feasibility or the control architecture are not provided in the patent.

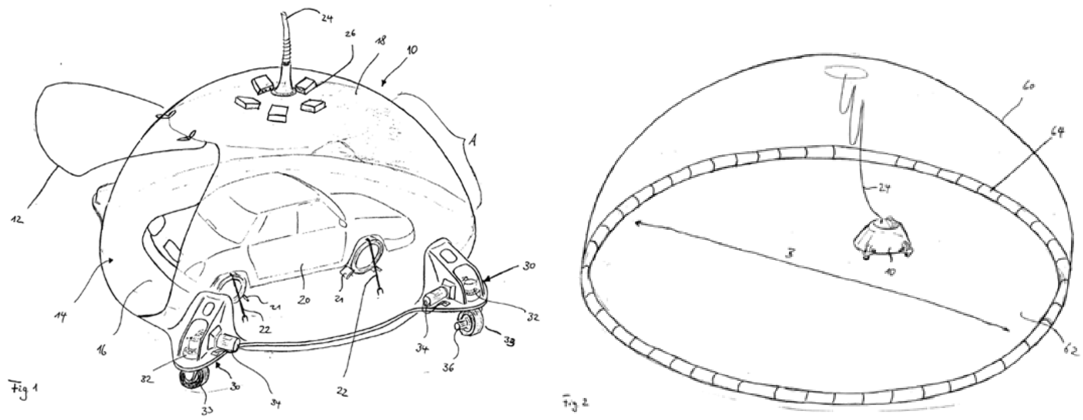

Figure 2.19: Self-propelled DS of Donges[121]

[117] Daimler: 12.5 m, $a_{\max} = 10\ \mathrm{m/s^2}$, 40 million €.

[118] FKFS: 10 x 7 m², $a_{\max} = 5\ \mathrm{m/s^2}$, 3.7 million €.

[119] Zeeb: Daimler DS, 2010.

[120] Donges: BMW DS patent, 2002.

[121] Donges: BMW DS patent, 2002.

The literature leaves unanswered why the steer angle of the DS is limited to ±180°. The consequences are restrictions for the possible washout motion because the yaw angle of the cabin is not independent from the trajectory of the DS. The washout is one of the major measures to reduce workspace. The additional effort for unlimited steer angle at the wheels is expected to be reasonable compared to the assumed benefit for the washout motion and long-lasting DS studies with complex trajectories. Additional disadvantage is expected from the introduced safety architecture that is an element of the infrastructure. One major problem is that the angle and position of impact is unknown. Hence, the workspace must be fully framed with the safety architecture and the DS itself needs to be designed to cope with any angle of impact. If the brake system of an on board safety architecture is designed for omnidirectional motion, the problem with orientation and position of the DS is solved. Furthermore, carrying the safety architecture on-board results in further independence of the infrastructure and eases the application at different locations.

2.6.2 Eindhoven University of Technology[122]

Slob et al. presents a concept of a self-propelled DS that provides 6 DOF. The carrier platform has 12 twin wheels that are grouped in four wheel frames as shown in Figure 2.20. Solid rubber tires are used. The dome is supposed to carry a real vehicle and performs pitch, roll, and heave via a three crank mechanism. The required motion performance of Table 2.8 is justified by simulation and measurements of typical vehicle maneuvers and by experience of former DS developments. No further details concerning the methodology of the derivation is provided. Whether an MCA is used for deriving the performance requirements remains unanswered. The literature gives no explanation why the yaw excursion is limited to ±1.2 rad (Table 2.8). The energy supply is realized by cables that are suspended from the ceiling by an active tracking system. No dimensioning of the electrical components of the DS is conducted.

[122] Slob et al.: WMDS, 2009.

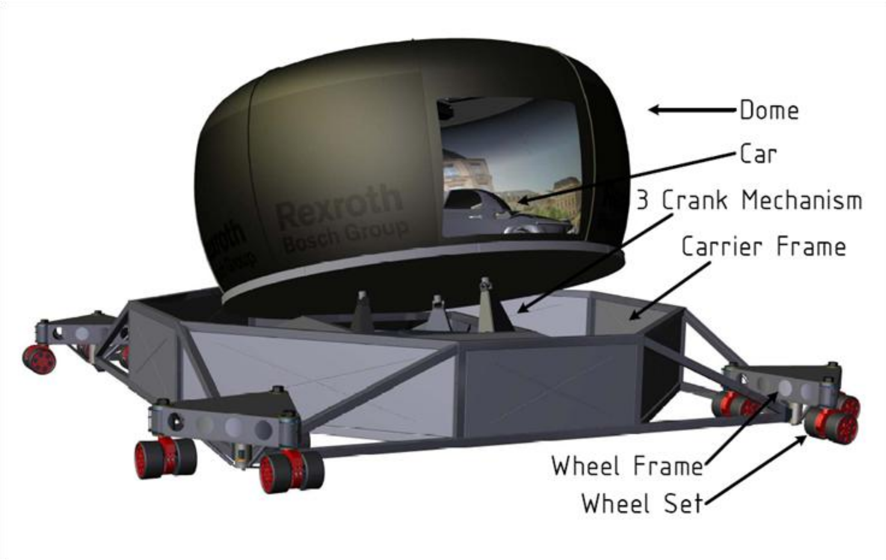

Figure 2.20: Self-propelled DS of Slob et al.[123]

Major focus is aimed at the wheel frames that allow performing instantaneous acceleration in any direction. This goal is reached by a caster of each wheel set as shown in Figure 2.21. The caster allows accelerating the steer axis in any direction by combined steering and rolling of the wheel. Longitudinal displacement of the steer axis (Figure 2.21: *P*) is performed by equal wheel rotation of both wheels in the same direction. Lateral displacement is created by superposing the aforementioned longitudinal motion and steering around point *A* due to counter rotation of the twin wheels. This idea overcomes the nonholonomic[124] characteristic of conventional wheels, thus enabling omnidirectional motion.

[123] Slob et al.: WMDS, 2009.

[124] Waldron; Schmiedeler: Kinematics of robots, p. 23, 2008.

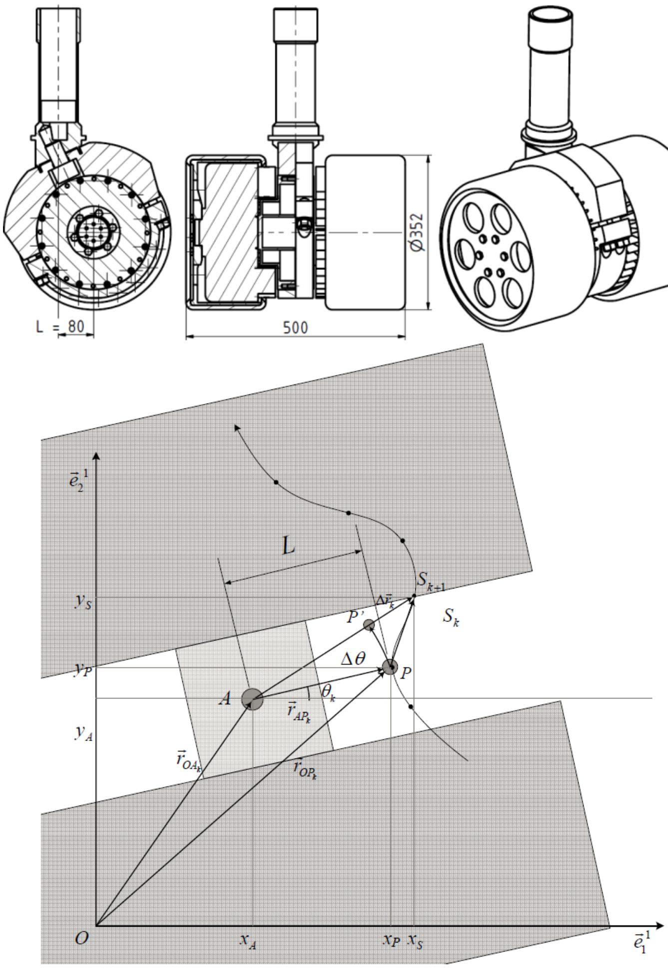

Figure 2.21: Wheel set of caster wheels of Slob et al.[125]

Table 2.8: Required motion performance of Slob's DS concept[126]

Non-simultaneous	Acceleration	Velocities	Displacement
Surge (x)	±7 m/s²	±4 m/s	± wall
Sway (y)	±7 m/s²	±4 m/s	± wall
Heave (z)	±5 m/s²	±0.4 m/s	±0.2 m
Roll (ϑ)	±5.2 rad/s²	±0.7 rad/s	±0.4 rad
Pitch (φ)	±5.2 rad/s²	±0.7 rad/s	±0.4 rad
Yaw (ψ)	±1.4 rad/s²	±1.1 rad/s	±1.2 rad

The safety architecture remains unaddressed. Only the need of a positioning system is stressed by Slob because the autonomous DS is unbound from the infrastructure. The

[125] Slob et al.: WMDS, 2009.

[126] cf. Slob et al.: WMDS, 2009.

energy supply of Slob's concept is wayside and must be fed from the ceiling by cables. It remains unanswered whether an on-board energy supply is of interest or feasible. In the context of rising electrical mobility and related battery technology, the present work opposes the idea of on-board energy supply. The overall effort is assumed to be reduced because elaborate active tracking systems for feeding energy from the ceiling are avoided. Furthermore, the expected independency increase of the infrastructure eases the application at different locations.

Slob is focused on performing trajectories while the task of the DS is to provide acceleration to the subject because humans do not perceive trajectory but do perceive acceleration. The nonholonomic constraint of a conventional wheel is a drawback of a wheeled system and is correctly stressed by Slob. It is hardly possible to control lateral motion of a conventional wheel, but it is possible to control its lateral forces if the wheel is in motion. Recalling the acceleration-based task of a DS shows that the problems caused by the nonholonomic characteristic only occurs in standstill. Thus, to the author, the question whether the effort of caster wheels is expedient remains unanswered, especially when considering further drawbacks like upcoming interaction of horizontal wheel forces and steer torque, as these are not mentioned by Slob.

2.6.3 TNO VeHIL

The VeHIL (Vehicle Hardware in the Loop)[127] is a developmental tool that enables hardware-in-the-loop tests for evaluating safety and reliability of sensors and the following chain of data processing. Hence, sensor information simulating relative motion between the treated sensors and traffic objects must be created. To do so, the sensors are mounted to a vehicle that is bound on a roller drum test rig following given velocity profiles. According to the velocity change of the bound vehicle, objects around the vehicle are actively moved, creating the relative motion of the artificial traffic objects. The setup is shown in Figure 2.22.

[127] TNO – virtual: VeHIL, 2008.

Figure 2.22: Picture of the TNO VeHIL motion base[128]

The applications differ from most DS studies where driver behavior is in focus and thus must be in the loop. Nevertheless, this system is introduced because the moving bases represent a highly concretized and similar system to the wheeled motion base of the present WMDS research.

System-immanent differences result from the diverse applications. The information presented here about the VeHIL system is from van der Meulen[129], if not referenced differently. The VeHIL must perform relative motion for the treated sensors. Hence, the task is based on position (distance) and velocity (relative velocity) level leading to these main controlled variables.[129] Because trajectory and velocity cannot be sensed by encapsulated human subjects (section 2.2), the main controlled variable of DS is the acceleration.

The VeHIL motion base does not carry subjects in contrast to DS. This circumstance dictates different requirements for the chassis design and safety architecture. Concerning the chassis design, it is emphasized that, in general, the body movement of the system (heave, pitch and roll) caused by pavement excitation and inertia forces is unwanted in both applications. Because the VeHIL motion base does not have to provide a valid driving experience to the cargo, the body movement caused by pneumatic tires is tolerated. The subject of a self-propelled, wheeled DS is more sensitive to the body movement because this affects the created driving experience. It is assumed that the vertical stiffness of the tire of the new DS concept will affect the created driving

[128] TU Delft – virtual: VeHIL, 2014.

[129] van der Meulen: Validation VeHIL, 2004.

experience. In the author’s opinion, the operationality of conventional pneumatic tires in DS applications is questionable.

Concerning safety architecture, attention is drawn to the fact that the references found do not treat this topic. Thus, it is unknown to the author how the motion bases behave in case of possible failures such as loss of electrical power and similar. While the safety architecture of the VeHIL motion base must ensure safety for the surrounding (system, hall, passenger car, driver, etc.), the DS has to provide additional safety for the carried subject. Therefore, more precise knowledge about the consequences of the counter-measures of the safety architecture is required. Hence, the maximum acceleration and deceleration of the DS, even for emergency stops, must be restricted to prevent harm to the subject.

The steer system of the VeHIL motion base is limited to ±350° and does not provide decoupling of the yaw orientation and the trajectory. The restriction becomes obvious when imagining the motion base circling the bound passenger car without yawing. Such a maneuver requires infinite steer angle of all wheels. Similar motion is caused by the washout of DS. Hence, unlimited steer angles are essential for WMDS.

The tolerated response time of the VeHIL motion bases is unknown to the author. The references do not deal with this topic. Even if the steer performance is not published, the motors and gearboxes of the steer unit allow conclusions with respect to the created steer performance. The worst case for the steer system of the VeHIL and the self-propelled DS is identical due to the common nonholonomic constraint: acceleration performance in standstill in perpendicular direction to the wheel orientation. In this case, the steer task is a 90° steer step performed as quickly as possible. According to the utilized hardware components, the minimum delay for the 90° steer step is estimated to be greater than about 0.2 s (see appendix C.2)

Concluding, it must be stressed that the discussed motion bases of the TNO VeHIL are similar to the concept idea of a self-propelled DS. On second sight, the VeHIL motion bases show several differences compared to DS applications as stated previously. In any case, the system setup is related, so that some research insights may profit from one another. The specifications of the VeHIL’s moving bases are shown in Table 2.9.

Table 2.9: Specifications of the motion system of the TNO moving base[130]

Property	Unit	Value
Mass	kg	750
Wheelbase	m	1.4
Track width	m	1.4
Propulsion	./.	Four-wheel independent drive
Steering	deg	Four-wheel independent steering (±350)
Moment of inertia of steer unit	kgm²	2.7[131]
Maximum velocity	m/s	±13.89
Maximum acceleration	m/s²	±10
Installed power	kW	52
Battery	./.	288 NiMH D-cells, 375 V, 100 kg

2.7 Battery Technology

The rail guided DS are connected to their power supply via a cable. This technology seems to be highly recommended when considering the introduced power demand of state-of-the-art DS (sections 2.5.2 and 2.5.4: 2000 - 4500 kW). The motivated goal for future DS technologies might take advantage of recent developments in battery technology. The energy supply via battery facilitates the necessary infrastructure of unbound motion systems. Therefore, a comparison between different energy storage strategies is presented in the form of a Ragone plot in Figure 2.23.

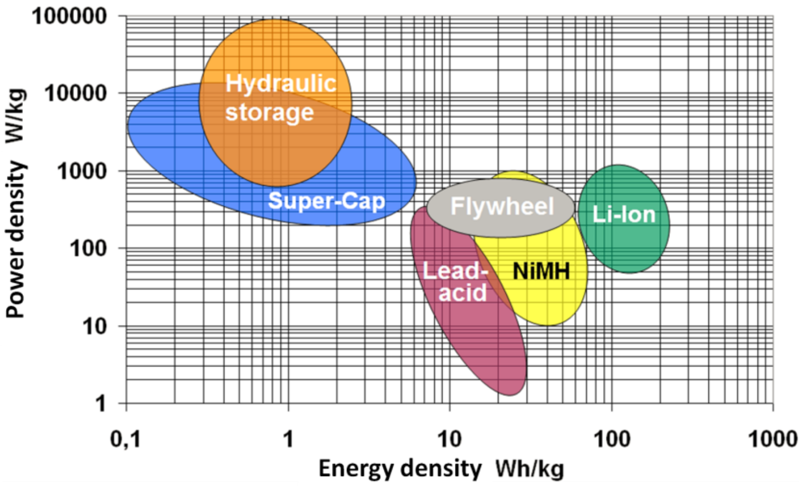

Figure 2.23: Ragone plot[132]

[130] cf. TNO – virtual: VeHIL, 2008.

[131] van der Meulen: validation VeHil, p. 43, 2004.

[132] Beidl: Lecture notes, 2013.

The most advanced battery technology used to date in automotive volume application is lithium-ion (Li-Ion). Nickel metal hydride (NiMH) and lead-acid technology are hampered by disadvantageous mass compared to more advanced battery technology such as Li-Ion and are excluded as the unbound motion system is strongly mass sensitive. Super capacitors (Super-Cap) are constrained by their strongly limited energy density, and as a consequence this technology is not suitable yet to solely power a future DS. The same constraints prohibit the use of hydraulic energy storage. The lithium-polymer (Li-Po) technology is not included in the Ragone plot. According to Pfaffenbichler et al.[133] Li-Po technology is similar to the Li-Ion but provides higher energy density at reduced costs. The disadvantage of Li-Po cells is the increased sensitivity to thermal and electrical constraints. Thus, the temperature range for operation is restricted from 0° to 60° C. Furthermore, the Li-Po cells are more complicated with respect to overcharging and exhausting discharge. The performance and cost advantage of Li-Po technology is of value for the present work because operation is expected to take place under thermally controlled in-door conditions. Hence, Li-Po technology is assumed to be promising for the feasibility analysis of the present work.

[133] Pfaffenbichler et al.: Electric mobility in Austria, 2009.

3 System Design

3.1 Description of WMDS Idea

This work provides a fundamental and systematic analysis of the self-propelled DS approach. For the first time, the physical feasibility of a WMDS and its limitations are determined. The new DS architecture is encouraging for far-reaching improvements of DS studies and is accompanied by cost reductions that enable a wider researcher base and extension of use.

WMDS are promising to solve the core problem of tremendous moving mass.[134,135,136] The new design approach does not require a mechanical system that spans the work-space. Recalling the scientific goal of the present work, the main idea is based on the assumption that a wheeled system whose propulsion is limited by friction forces is suitable to simulate the dynamics of vehicles that are also limited by tire friction forces.

The idea of a WMDS is addressed by a patent of Donges[137] (section 2.6.1) and a reference by Slob et al.[138] (section 2.6.2). Still, the references do not prove the feasibility of self-propelled DS. Requirements such as workspace, power, energy, and friction demand of the new DS approach are not analyzed in the aforementioned references and neither is system latency or the safety architecture. Therefore, a representative assembly of a WMDS utilizing an omnidirectional motion base is considered. This assembly of the class of the self-propelled, wheeled DS is the result preliminary research of the present work.[139] The wheeled motion base, with three conventional, powered and actively steerable wheels, allows translational motion (surge: x, sway: y) and yaw (ψ). On top of the platform a tilt system would be mounted, providing at minimum pitch (φ), roll (ϑ) and heave (z). The chosen design shows inbuilt stroke fitting real-world vehicle motion. Avoiding the conventional sledges, which mainly cause the moving mass to increase, results in a light-weight design concept.

---

[134] Betz et al.: Motion analysis of WMDS, 2012.

[135] Betz et al.: Concept analysis of WMDS, 2012.

[136] Betz et al.: Driving dynamics control of WMDS, 2013.

[137] Donges: BMW DS patent, 2002.

[138] Slob et al.: WMDS, 2009.

[139] Betz: Preliminary WMDS research, 2010.

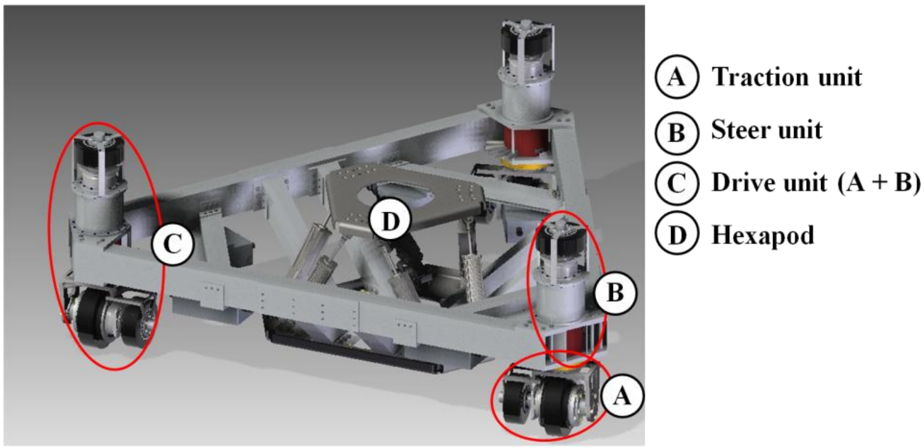

Figure 3.1: CAD model of the representative WMDS[140]

In Figure 3.1 a CAD model of the representative WMDS setup is presented. Because tilting is a familiar task in DS and the major scientific interest lies in the wheeled motion base, a conventional hexapod is utilized for providing cabin tilt (D). The hexapod is a highly developed tilt system because it is used in all dynamic DS (section 2.5). The hexapod is mounted between the wheeled motion base and the DS cabin, which is not illustrated in the figure. Three drive units (C) must provide tire friction forces. To do so, a steer unit (B) and a traction unit (A) are required in order to control the wheel torque and the slip angle.

The representative WMDS of the present work is characterized by three main design decisions: number of drive units, chassis design, and type of tire. Because there are no existing examples concerning WMDS in the literature, very little knowledge is available for the necessary design decisions. In any case, the representative WMDS design is determined by the information available to the author and leads to a structure that is intended to accelerate the gain of insights into the new DS concept.

The determined design decisions are justified in the following:

- Number of drive units:
  At least three drive units are required in order to create a system that does not need to be actively stabilized in standstill. The maximum number of drive units is not limited. The decision for the minimum number of drive units is justified by the minimum hardware effort and the advantage of the not over-determined characteristic of the wheel load distribution. If a solution exists that does not require enhanced chassis design (body spring and damper), it is expected to be the

[140] cf. Wagner: WMDS, Master’s thesis supervised by Betz, 2013.

three-wheeler due to its unambiguous wheel load distribution[141]. With an increasing number of drive units, the footprint decreases because the created polygon draws nearer to the inscribed circle of rollover safety (as presented in section 3.5.4). Whether the increased number of drive units confers any advantage besides reduction of footprint is unknown. For the fundamental feasibility analysis of the WMDS, the size of the footprint is not of relevance because the generally needed operating space is significantly larger by more than one magnitude.

- Chassis design:
  Even if the number of wheel units is determined to the minimum number of three, several possible designs for the wheel frame exist. Chassis parameters like caster, toe, camber, single or twin wheel and similar have to be considered.
    - Toe:
      The independent wheel steer angles do not require designed toe, because it is a fully controllable DOF of the motion base.
    - Caster:
      The chosen design has no caster for two reasons. First, steering would lead to excitations of the body due to the lever between the steer axis and the contact patch. This constraint would cause disturbances to the acceleration simulation of the DS and would cause additional effort to the motion control or alternative countermeasures. Second, the horizontal wheel forces would cause self-aligning torque that must be considered as disturbance of the steer task. The only advantage of caster wheels might result from the possibility of solving the nonholonomic constraint of conventional wheels as presented by Slob (section 2.6.2). The associated problems of caster wheels are expected to be excessive and therefore prompt the decision of no caster wheels.
    - Camber:
      The selected chassis design has neither body spring or damper nor complex steer kinematics. Thus, no wheel lift occurs. Furthermore, the omnidirectional property of the WMDS causes no predictable coherence of steer angle and the demand of lateral forces as known from passenger cars. Therefore, no camber is applied to the drive units.
    - Single or twin wheel:
      Both setups require six motors in order to provide traction and steer torque. The single setup uses three motors for traction and the remaining ones for the steer task of the wheel. The steer torque is supported by the moment of inertia around the vertical axis of the DS and the friction forces of the other drive units considering the lever arm between the

[141] Similar to three-legged furniture items that do not wobble on uneven foundations.

drive units. The twin wheel setup does not require motors that are solely dedicated to the steer task. Instead it utilizes opposed torque of the traction motors in order to perform the steer task. The steer torque is supported by the tire friction force and by the lever arm of the wheel to its steer axis. The major problem of the twin wheel setup is expected to result from the increased moment of inertia of the steer unit because twice as many components have to be assembled around the steer axis. This fact causes significant increase of the required steer torque because of the quadratic dependency of the moment of inertia with respect to displacement of the steer axis. Striving for reducing the necessary hardware effort leads to the decision for single wheels.

- Type of tire:
  In general, the body movement of the system[142] (heave, pitch, and roll) is unwanted because it affects the created driving experience and must be considered as disturbance. In order to counteract these movements, the WMDS utilizes press-on band tires as they are known from forklift trucks. These tires provide high vertical tire spring stiffness, thus reducing body movement assuming an even foundation.

3.2 Applied MCA

This work utilizes an MCA for analyzing the feasibility of an alternative motion system for DS. The MCA should be able to take advantage of the system-immanent motion capability of the new DS approach in terms of enhanced horizontal workspace. The concept presented in this section and subsection 3.2.1 was published in Betz et al.[143].

The applied MCA is similar to the classical washout. The so called “ideal” MCA (Figure 3.2) calculates the target DS states that are necessary to perform the target motion cue input. The goal is a frequency independent acceleration simulation similar to the complementary filter approach from Sammet[144] and Murano et al.[145] (section 2.3.2). By closing the frequency gap of the MCA, the created driving experience is no longer subject to the occurring frequencies. In general, this “ideal” MCA provides a more

[142] This motion is caused by inertial forces.

[143] Betz et al.: Motion analysis of WMDS, 2012.

[144] Sammet: MCA, 2007.

[145] Murano et al.: Toyota DS, 2009.

realistic acceleration simulation at the cost of increased workspace demand. The characteristic of the new MCA suits the system-immanent motion capability of the WMDS.

The basic idea is to allow as much acceleration simulation from tilt as possible by a linear filter, while considering human perception thresholds for tilt coordination. Therefore, a 2nd order LP is used to determine the change of translational acceleration performed by tilt coordination. The parameterization of the LP used should fit human perception thresholds and is tuned for the expected acceleration cues of the conducted test drives as described in section 3.2.2. The filters used are time invariant and must be tuned in advance. More advanced filter designs exist that are time variant in order to improve the exploitation of the workspace, but are disregarded on purpose because transparency of the filter parameters is lost and tuning effort increases.[146] Thus a comprehensive evaluation of the WMDS behavior is facilitated.

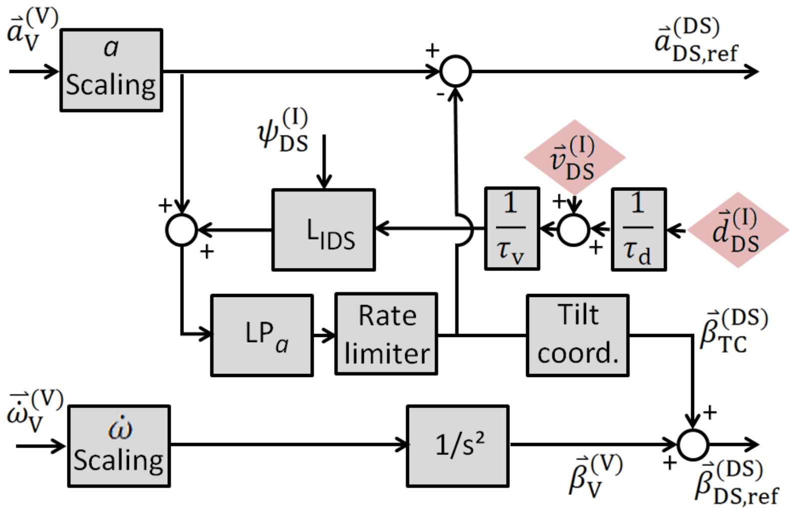

Figure 3.2: Block diagram of the MCA used[147]

The acceleration realized by tilt coordination is subtracted from the target acceleration and leads to the part of acceleration that must be performed by translational motion. The translational control variable of the control architecture introduced later (section 3.3.3, p. 69) is on the acceleration level; thus, neither a coordinate transformation (to inertial COS (I)) nor an integration to position cues is required in the translational path. This method provides a frequency-independent gain for the acceleration cues. With the described method, an “ideal” motion simulation is reached, considering the usual adverse

[146] Fischer: MCA DLR, p. 24-40. 2009.

[147] cf. Betz et al.: Driving dynamics control of WMDS, 2013.

effects due to tilt[148]. A rate limiter is implemented that limits the LP output rate if human perception thresholds are approached. The limiter becomes necessary if the subject's reaction causes higher onsets of the motion cues as expected in the previously conducted MCA tuning.

The washout is implemented as a feedback gain of DS velocity $\vec{v}_{\mathrm{DS}}$ ($1/\tau_{\mathrm{v}}$) and displacement from origin $\vec{d}_{\mathrm{DS}}$ ($1/\tau_{\mathrm{d}}$). The feedback must be transformed ($\mathrm{L_{IDS}}$) from the DS COS (DS) into the inertial COS (I) in order to generate a returning motion to the initial position.

The physical limitation of tilt coordination is recognized by a saturation block that avoids simulating more than 0.4 g translational acceleration by tilt (not illustrated in Figure 3.2).

The rotational path also contains scaling that can be used if necessary[149]. First it should be stressed that the rotational path is reduced to yaw motion in the present work. The pitch and roll motion of the virtual vehicle is disregarded because it belongs to the well researched part of the hexapod motion that is not treated in the present work as aforementioned. Considering real DS applications, these disregarded hexapod motions have to be superpositioned with the motion of the tilt coordination. Scaling of yaw motion is not applied in the present work (section 2.1.4) because no yaw angle limitation exists for WMDS; thus, scaling of yaw becomes unnecessary.

3.2.1 Parameterization of Feedback Gains[150]

The parameterization for the feedback gains depends on the research focus and the traffic maneuver conducted. The stability analysis refers to the loop gain (G_{loop}), derived from equations (4) and (5) and gives a lower boundary for the product of the two feedback gains according to equation (6). The derivation of equation (6) is described in appendix D (p. 131). The parameter c is used to tune the stability margin in view of the Nyquist criterion. According to the analytical limit of equation (6), the gains are tuned iteratively in order to reduce the required workspace for the conducted urban test drives: $\tau_v = 4.49$ s and $\tau_d = 19.77$ s.

---

[148] Tilt causes the subject's COS to be reoriented with respect to the horizontal plane of the translational motion. Thus, the elicited translational motions are perceived with trigonometrical distortion of cosine and sine of the tilt angle. These adverse effects are tolerated in all enhanced DS that utilize additional translational motion such as the DS introduced in section 2.5.

[149] Possible reasons for scaling the rotational inputs: reducing minor relevant motion in order to prevent motion sickness; reducing the vehicles pitch and roll motion in order to keep reserve for tilt coordination, washout, and similar.

$$G_{\text{loop}} = \left(\frac{1 + s\tau_d}{s^2\tau_d\tau_v}\right) G_{\text{LP}} \tag{4}$$

$$G_{\text{loop}} = \left(\frac{1 + s\tau_d}{s^2\tau_d\tau_v}\right) \frac{1}{1 + 2dTs + T^2s^2} = -c, c \leq 1, \tau_v \geq 0, \tau_d \geq 0 \tag{5}$$

$$\tau_d\tau_v > \frac{4T^2}{c} \tag{6}$$

3.2.2 Parameterization of the Low-Pass Filter

The tuning of the invariant low-pass filter is subject to tolerated rotational rate and acceleration limits (exemplarily for pitch: $\dot{\varphi}_{\text{limit}}$ and $\ddot{\varphi}_{\text{limit}}$) as well as the expected acceleration profiles. The tuning is conducted in two steps: pre-tuning and final tuning. The methodology of the pre-tuning is presented in Figure 3.3. The detailed derivation is described hereafter.

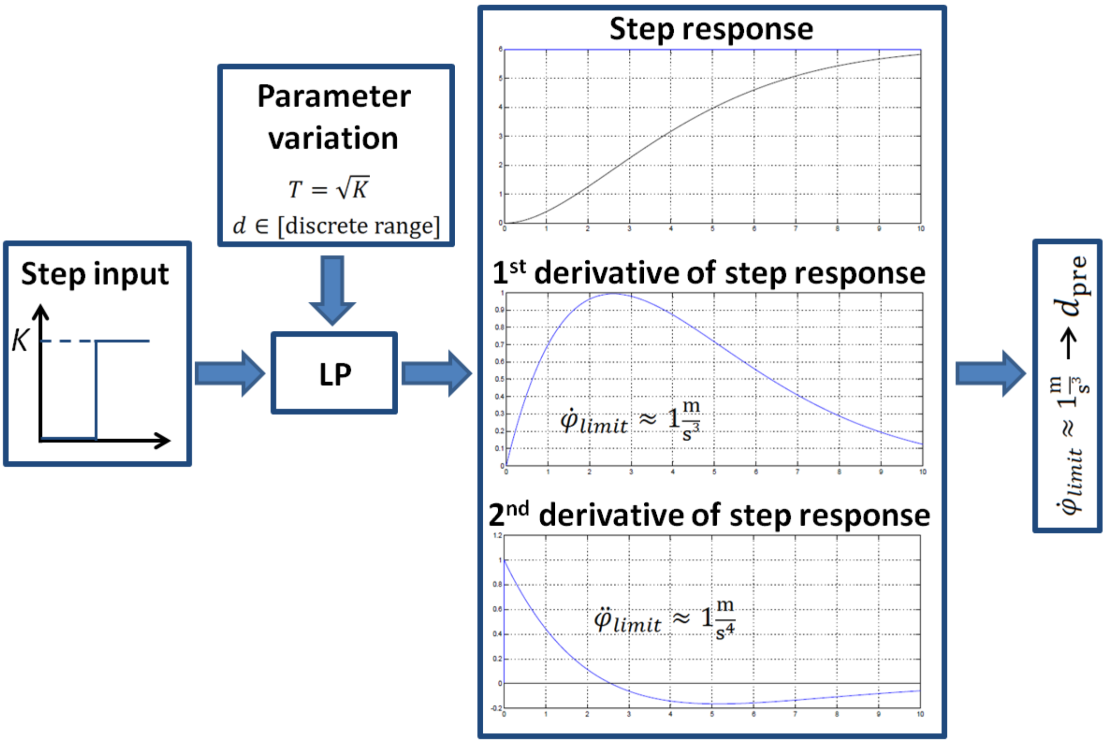

Figure 3.3: Methodology of the pre-tuning of the LP

The rotational limits are converted into corresponding limitations of the first and second derivative of the filter's response. Therefore, the relation between tilt and horizontal acceleration is linearized. The calculations are conducted exemplarily for pitch motion.

[150] Betz et al.: Motion analysis of WMDS, 2012.

$$a_x = \sin(\varphi)\, g$$
$$a_x \approx \varphi \frac{1}{\text{rad}} g$$
$$\rightarrow \; \dot{a}_{x,\text{limit}} \approx \dot{\varphi}_{\text{limit}} \frac{1}{\text{rad}} g = 0.1 \frac{\text{rad}}{\text{s}} \frac{1}{\text{rad}} 9.81 \frac{\text{m}}{\text{s}^2} \approx 1 \frac{\text{m}}{\text{s}^3}$$
$$\rightarrow \; \ddot{a}_{x,\text{limit}} \approx \ddot{\varphi}_{\text{limit}} \frac{1}{\text{rad}} g = 0.1 \frac{\text{rad}}{\text{s}^2} \frac{1}{\text{rad}} 9.81 \frac{\text{m}}{\text{s}^2} \approx 1 \frac{\text{m}}{\text{s}^4} \qquad (7)$$

The transfer function of a second order LP is

$$G_{\text{LP}}(s) = \frac{1}{1 + 2dTs + T^2 s^2} \qquad (8)^{151}$$

The pre-tuning is done by the analytical step response (aperiodic: $d > 1$) in order to avoid multiple extreme values. The amplitude K is selected according to the regarded maneuver considering the maximum occurring acceleration peak of the virtual vehicle and the applied scaling ($K = a_{xy,\text{V,max}} \cdot scaling\ factor$):

$$y(t) = K - \frac{K}{T_1 - T_2}\left[T_1 e^{-\frac{t}{T_1}} - T_2 e^{-\frac{t}{T_2}}\right], \qquad \text{with } T_{1,2} = \frac{T}{d \pm \sqrt{d^2 - 1}} \qquad (9)^{152}$$

The first and second derivatives of the step response must be limited so as not to harm the tolerated rotational limits.

$$\dot{y}(t) = \frac{K}{T_1 - T_2}\left[e^{-\frac{t}{T_1}} - e^{-\frac{t}{T_2}}\right] \qquad (10)$$

$$\ddot{y}(t) = \frac{K}{T_1 - T_2}\left[-\frac{1}{T_1} e^{-\frac{t}{T_1}} + \frac{1}{T_2} e^{-\frac{t}{T_2}}\right] \qquad (11)$$

$$\dddot{y}(t) = \frac{K}{T_1 - T_2}\left[\frac{1}{{T_1}^2} e^{-\frac{t}{T_1}} - \frac{1}{{T_2}^2} e^{-\frac{t}{T_2}}\right] \qquad (12)$$

[151] Lunze: Control engineering, p. 290, eq. 6.108, 2010.

[152] Lunze: Control engineering, p. 193, eq. 5.177, 2010.

The maximum of $|\dot{y}(t)|$ takes place at

$$\ddot{y}(t) = \frac{K}{T_1 - T_2}\left[-\frac{1}{T_1}e^{-\frac{t}{T_1}} + \frac{1}{T_2}e^{-\frac{t}{T_2}}\right] = 0$$
$$\rightarrow t_{\dot{y},\max} = (\ln(T_1) - \ln(T_2))\frac{T_1 T_2}{T_1 - T_2} \tag{13}$$

The maximum of $|\ddot{y}(t)|$ takes place at

$$\dddot{y}(t) = \frac{K}{T_1 - T_2}\left[\frac{1}{T_1{}^2}e^{-\frac{t}{T_1}} - \frac{1}{T_2{}^2}e^{-\frac{t}{T_2}}\right] = 0$$
$$\rightarrow t_{\ddot{y},\min,1} = 2(\ln(T_1) - \ln(T_2))\frac{T_1 T_2}{T_1 - T_2} \tag{14}$$
$$\rightarrow t_{\ddot{y},\max,1} = 0$$

The relevant solutions that have to be considered for the pre-tuning are $t_{\dot{y},\max}$ and the trivial solution $t_{\ddot{y},\max,1} = 0$ because these solutions cause the peak values ($|\dot{y}|_{\max}$ and $|\ddot{y}|_{\max}$). According to Figure 3.3 the solution $t_{\ddot{y},\min,1}$ causes smaller absolute values than $t_{\ddot{y},\max,1}$ ($\left|\ddot{y}\left(t_{\ddot{y},max,1}\right)\right| > \left|\ddot{y}\left(t_{\ddot{y},\min,1}\right)\right|$) and thus is disregarded.

The pre-tuning now assumes the tolerated rate, acceleration limits (according to equation (7)), and a worst-case edge steepness of the input: step input with the amplitude *K*. The filter pre-tuning is conducted to meet the constraints:

$$\left|\dot{y}\left(t_{\dot{y},\max}\right)\right| = \dot{a}_{x,\mathrm{limit}} = 1\ \frac{\mathrm{m}}{\mathrm{s}^3} \tag{15}$$
$$\left|\ddot{y}\left(t_{\ddot{y},\max,2}\right)\right| = \ddot{a}_{x,\mathrm{limit}} = 1\ \frac{\mathrm{m}}{\mathrm{s}^4} \tag{16}$$

According to Mathematica[153], the set of equations cannot be solved unambiguously for the filter parameters *d* and *T*. When considering only equation (16), an unambiguous solution for the parameter *T* is determined:

$$T = \sqrt{K\frac{\mathrm{s}^4}{\mathrm{m}}} \tag{17}$$

[153] Wolfram – virtual: Computational software program, http://www.wolfram.com/mathematica/?source=nav, last access: May 30th 2014.

Therefore, the tuning of the parameter d takes place numerically in order to determine the filter parameterization allowing maximum tilt limits without harming the tolerated boundaries.

It should be considered that the introduced pre-tuning of the filter fulfills the requested constraints of equation (15) and (16) for the applied step input. The step input itself is an artificial signal with infinite edge steepness that does not occur in real-world vehicle dynamics. This artificial characteristic is used by the conducted T-junction maneuver because calculated reference signals are assumed (section 4.1.1). Hence, the pre-tuning is suitable for the analyzed T-junction maneuver. The filter parameterizations of the various T-junction maneuvers are presented in Table 3.1.

Concerning the representative urban circuit it should be noted that the amplitude of the filter input in the DS's MCA is composed of the washout and real-world acceleration profiles of the virtual vehicle as shown in Figure 3.2. Thus, the precise edge steepness and amplitude are difficult to predict. Therefore, the described methodology of the pre-tuning by step inputs is used to provide first orientation but requires additional tuning for the specific test maneuver of real-world traffic. The methodology of the final tuning is presented in Figure 3.4.

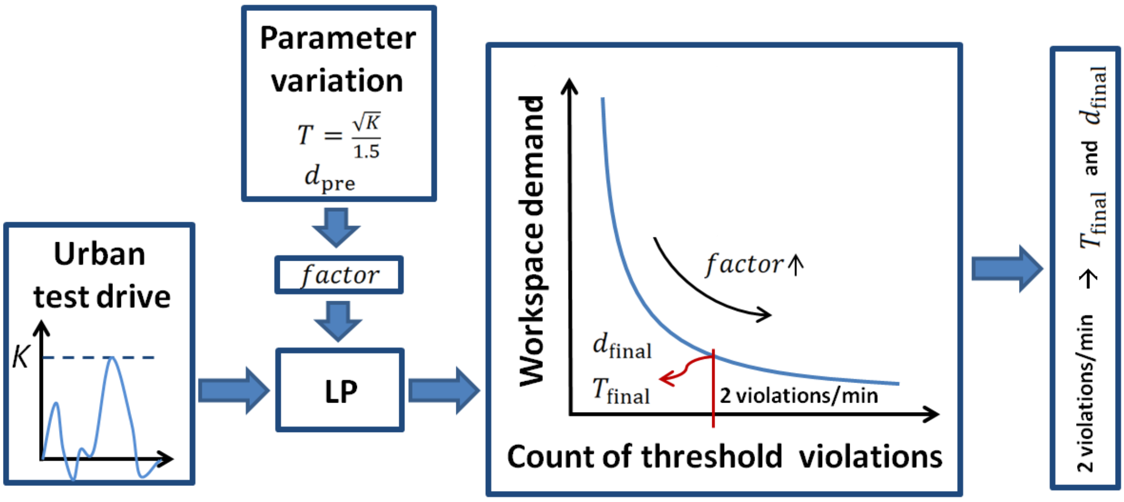

Figure 3.4: Methodology of the final tuning of the LP

The results imply that the real-world acceleration profiles affect the relations of equations (15) and (16) differently. The real-world test drives cause significantly more $\dot{\varphi}_{\mathrm{limit}}$ violations than $\ddot{\varphi}_{\mathrm{limit}}$ violations. This result shows that there is not as much advantage taken of rotational acceleration as of rotational rate. Thus, the analytically derived relationship between T and K of equation (17) is iteratively adapted in order to cause an equal count of violations of both rotational limits for the real-world test maneuver of the urban circuit:

$$T = \frac{\sqrt{K \frac{\mathrm{s}^4}{\mathrm{m}}}}{1.5} \tag{18}$$

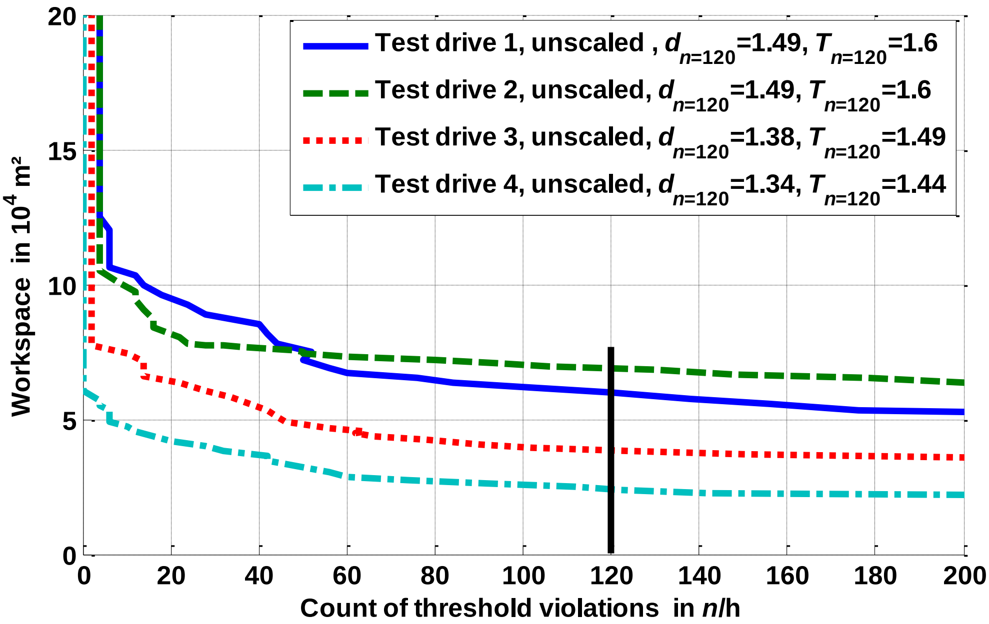

Figure 3.5: Exemplary filter parameterization – workspace vs. violations (derived in accordance with Figure 3.4 by variation of d_{pre} and T while remaining their ratio $-T_i/d_{\mathrm{pre},i}$ = constant)

The final tuning of the filter parameterization for the urban circuit is subject to the tradeoff between workspace demand and count of threshold violations. Some violations are tolerated on the basis of two aspects. First, the selected thresholds for tilt coordination are not physically determined, precise values but may vary with the subject and the conducted maneuver as previously mentioned in section 2.2.2. Second, the MCA has a limiter that prevents the severity of the transgression. Figure 3.5 shows exemplarily the tradeoff for the four different, unscaled urban test drives. The set of filter parameters (T and d) is numerically varied and applied to each of the test drives. The parameter variation is based on the pre-tuning results derived by the constraint of equation (18). The derived ratio (T/d) is maintained unchanged. For the present work, the final tuning for real-world test drives determines the parameterization that causes about two threshold violations per minute. Because the duration of the urban test drives is about 1 h, the selected count of violations is $n = 120$. This request is determined by the author in order to compare different test drives by maneuver-dependent parameterization that takes comparable advantage of tilt coordination.

Table 3.1: Parameterization of LP

		K in m/s²	**Scaling**	**$d_{n=120}$**	**$T_{n=120}$**
T-junction		3	1	0.46	1.73
		6	1	0.86	2.45
Representative urban circuit	Test drive 1	6	1	1.49	1.6
		6	0.7	1.16	1.33
		6	0.5	0.93	1.14
	Test drive 2	6	1	1.49	1.6
		6	0.7	1.18	1.34
		6	0.5	0.94	1.15
	Test drive 3	6	1	1.38	1.49
		6	0.7	1.1	1.26
		6	0.5	0.88	1.09
	Test drive 4	6	1	1.34	1.44
		6	0.7	1.07	1.22
		6	0.5	0.86	1.05

3.3 Applied Motion Control

The MCA creates a task for the tilt system of the cabin and the wheeled motion base. In the following, only the motion cues of the wheeled motion base are treated (3 DOF: x, y, ψ). The task of the tilt system (3 DOF: φ, ϑ, z) is not further presented because it is well researched and understood as described previously (section 3.1). The concept presented in this section was published in Betz et al.[154,155].

The relevant outputs of the MCA for the wheeled motion base are horizontal ($\vec{a}_{\mathrm{DS,ref}}^{(\mathrm{DS})}$) and yaw ($\ddot{\psi}_{\mathrm{DS,ref}}^{(\mathrm{DS})}$) accelerations for the center of gravity (CG) of the motion base. But the coordination of the available actuators must be established in order to perform the motion of the CG of the WMDS. The so-called motion control transforms the acceleration-based task of the DS's CG into the required DS's actuator tasks. The motion control strongly depends on the system design used because it may differ significantly in terms of the number of actuators, wheels and geometric constraints.

The main difficulties for regarding the wheeled motion base adressed here are the over-actuated design and the slip-afflicted tires. The motion control is required to solve the ambiguous characteristics of the presented assembly and should take into account slip

[154] Betz et al.: Concept analysis of WMDS, 2012.

[155] Betz et al.: Driving dynamics control of WMDS, 2013.

effects of the tires. The task is solved using the equations of horizontal vehicle dynamics, making use of a linear model of the lateral tire dynamics and adding further constraints like equal exploitation of the wheels' friction capability. The added constraints solve the ambiguous characteristics and incidentally cause equal friction reserve at each wheel in order to stay in the linear μ-slip characteristics of the tire for as long as possible. An overview of the motion control methodology developed in the present work is presented in the form of a schematic block diagram in Figure 3.6. The process presented in the figure is explained step-by-step in the following enumeration (a) to (d).

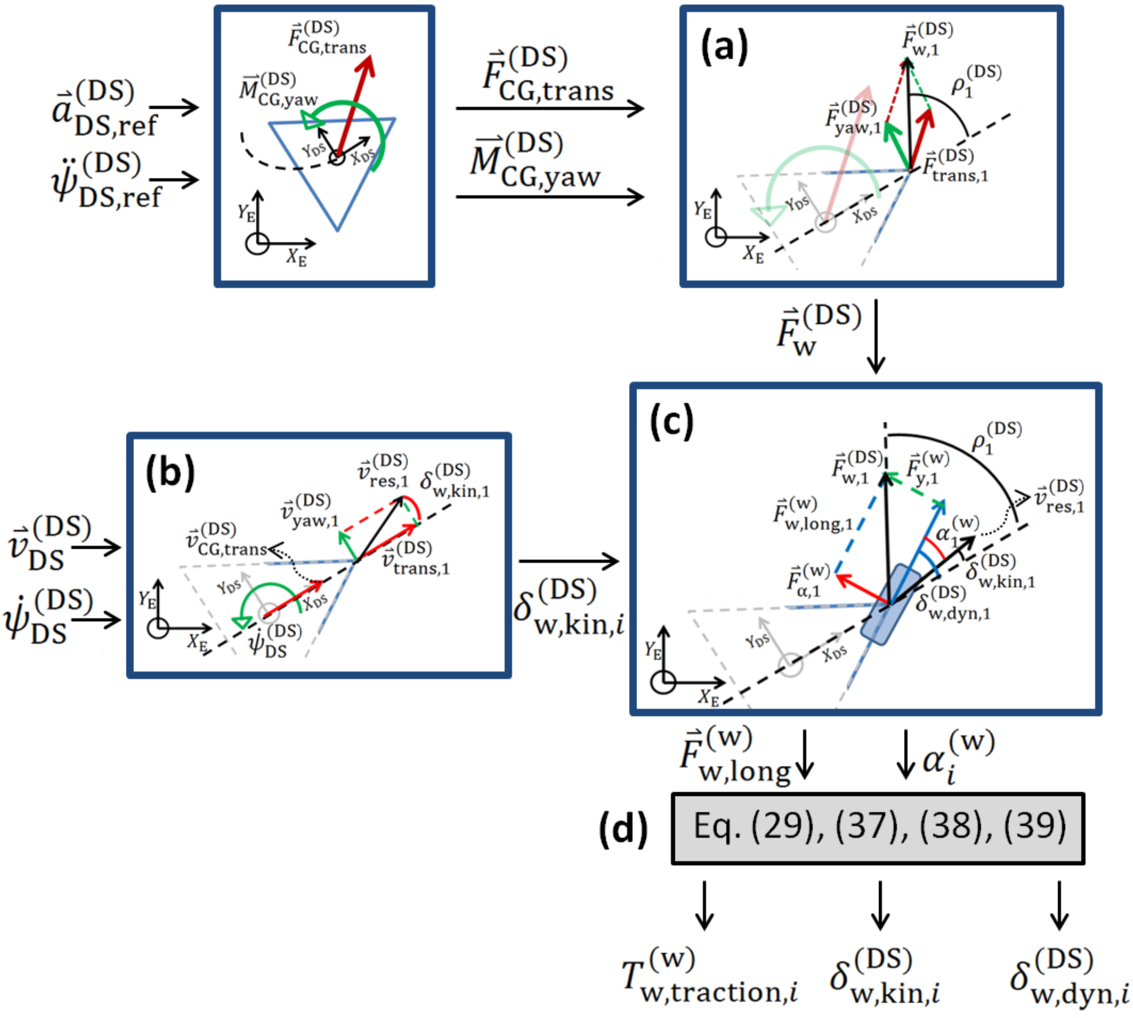

Figure 3.6: Block diagram of the motion control methodology[156]

(a) The required distribution of the horizontal wheel force for the three wheels of the motion base must be determined to achieve the introduced acceleration demands. The motion demand is split into a translational ($\vec{F}_{\text{trans},i}$) and a yaw task ($\vec{F}_{\text{yaw},i}$). The presented algorithm distributes the traction forces with the aim of

[156] cf. Betz et al.: Driving dynamics control of WMDS, 2013.

minimizing friction coefficient differences between the wheels in order to realize equal friction demand and to stay in the linear µ-slip characteristics of the tire for as long as possible. Thus, the information about dynamic wheel load distribution is required in order to determine the resulting wheel forces ($\vec{F}^{(\mathrm{DS})}_{\mathrm{w},i}$). A detailed description of the calculations of (a) is presented in section 3.3.1.

(b) Now that the required wheel forces are known ($\vec{F}^{(\mathrm{DS})}_{\mathrm{w},i}$) the actual DS states have to be identified to derive the tasks of the wheels. The DS states are required because the acceleration-based task calculated here is superimposed with the velocity state of the system. Hence, a kinematic model is utilized to determine the kinematic vehicle states disregarding dynamic effects like slip. The resulting kinematic wheel steer angles ($\delta^{(\mathrm{DS})}_{\mathrm{w,kin},i}$) are provided for further calculation in (c) and (d). A detailed description of the calculations of (b) is presented in section 3.3.2 (Kinematic Model of WMDS).

(c) The required wheel forces ($\vec{F}^{(\mathrm{DS})}_{\mathrm{w},i}$) and kinematic wheel orientations ($\delta^{(\mathrm{DS})}_{\mathrm{w,kin},i}$) are provided to determine the longitudinal and lateral tasks of the wheels – longitudinal wheel force demand ($\vec{F}^{(\mathrm{W})}_{\mathrm{w,long},i}$) and slip angles ($\alpha^{(\mathrm{W})}_{i}$). These values are estimated using a numerical optimization of a linear model of lateral tire dynamics. A detailed description of the calculations of (c) is presented in section 3.3.2 (Slip Angle Estimation).

(d) The final actuator tasks, three torques ($T^{(\mathrm{W})}_{\mathrm{w,traction},i}$) of the traction motors and three dynamic steer angles of the wheels ($\delta^{(\mathrm{DS})}_{\mathrm{w,dyn},i}$), are calculated according to equations (29), (37), (38), and (39). A detailed description of the calculations of (d) is presented in the section 3.3.2 (Resulting Actuator Tasks).

3.3.1 Distribution of Horizontal Wheel Force

Dynamic Wheel Loads

The dynamic wheel loads are calculated with respect to Newton's first law of motion. The wheel load distribution is affected by the following: system mass (m_{total}), translational acceleration demand with respect to the DS COS ($a_{\mathrm{CG},x}$, $a_{\mathrm{CG},y}$), height of the CG (h_{CG}) and edge length of the equilateral triangle arising from the three wheel contact patches (l_{t}). The demanded horizontal forces are shown here:

$$F_{\mathrm{CG},x} = m_{\mathrm{total}} \cdot a_{\mathrm{CG},x} \tag{19}$$
$$F_{\mathrm{CG},y} = m_{\mathrm{total}} \cdot a_{\mathrm{CG},y} \tag{20}$$

According to Newton's first law of motion and Figure 3.7, the following set of equations is derived:

$$\begin{aligned}\sum F_z &= F_{z,\mathrm{w},1} + F_{z,\mathrm{w},2} + F_{z,\mathrm{w},3} + m_{\mathrm{total}} \cdot g = 0 \\ \sum M_x &= F_{\mathrm{CG},y} \cdot h_{CG} + \frac{F_{z,\mathrm{w},2} \cdot l_t}{2} - \frac{F_{z,\mathrm{w},3} \cdot l_t}{2} = 0 \\ \sum M_y &= F_{\mathrm{CG},x} \cdot h_{\mathrm{CG}} - \frac{F_{z,\mathrm{w},1} \cdot l_t}{\sqrt{3}} + \frac{F_{z,\mathrm{w},2} \cdot l_t}{2\sqrt{3}} + \frac{F_{z,\mathrm{w},3} \cdot l_t}{2\sqrt{3}} = 0\end{aligned} \tag{21}$$

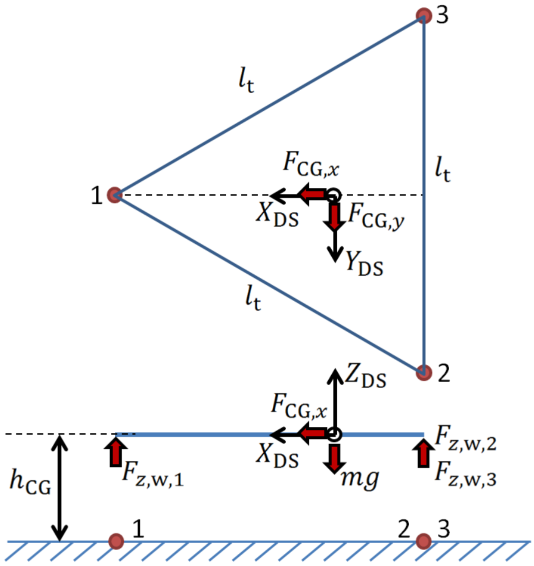

Figure 3.7: Schematic drawing of the geometrical constraints for the calculation of the wheel loads[157]

The system of equations (21) is solved for the three wheel loads:

$$\begin{aligned}F_{z,\mathrm{w},1} &= \frac{2F_{\mathrm{CG},x} \cdot h_{\mathrm{CG}}}{\sqrt{3} \cdot l_{\mathrm{t}}} + \frac{m_{\mathrm{total}} \cdot g}{3} \\ F_{z,\mathrm{w},2} &= \frac{-F_{\mathrm{CG},x} \cdot h_{CG}}{\sqrt{3} \cdot l_{\mathrm{t}}} + \frac{F_{\mathrm{CG},y} \cdot h_{\mathrm{CG}}}{l_{\mathrm{t}}} + \frac{m_{\mathrm{total}} \cdot g}{3} \\ F_{z,\mathrm{w},3} &= \frac{-F_{\mathrm{CG},x} \cdot h_{\mathrm{CG}}}{\sqrt{3} \cdot l_{\mathrm{t}}} - \frac{F_{\mathrm{CG},y} \cdot h_{\mathrm{CG}}}{l_{\mathrm{t}}} + \frac{m_{\mathrm{total}} \cdot g}{3}\end{aligned} \tag{22}$$

Force Distribution for Translational Task

The translational forces at each wheel are oriented parallel to the translational force vector ($\vec{F}_{\mathrm{CG,trans}}$) of the horizontal acceleration demands as shown in Figure 3.8. The

[157] cf. Wagner: WMDS, Master's thesis supervised by Betz, 2013.

magnitude at each wheel is determined by equations (23), (24) and (25) using the same friction coefficient (μ_{trans}) resulting from translational force demand divided by overall system wheel load ($m_{\mathrm{total}} \cdot g$).

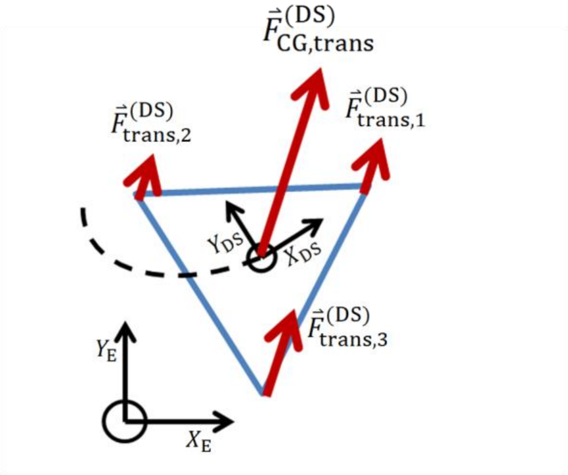

Figure 3.8: Force distribution of translational task[158]

$$\left|\vec{F}_{\mathrm{CG,trans}}\right| = \sqrt{F^2{}_{\mathrm{CG},x} + F^2{}_{\mathrm{CG},y}} \tag{23}$$

$$\mu_{\mathrm{trans}} = \frac{\left|\vec{F}_{\mathrm{CG,trans}}\right|}{m_{\mathrm{total}} \cdot g} \tag{24}$$

$$F_{\mathrm{trans},i} = F_{z,\mathrm{w},i} \cdot \mu_{\mathrm{trans}} \tag{25}$$

Analytical examination of the equations of motion in Mathematica[159] shows no interaction of the translational wheel forces onto the yaw motion of the moving base (appendix E, p. 132). The reason for this is the wheel-load-dependent distribution of the overall translational force demand. The moment about the yaw axis, generated by the translational wheel forces, cancel each other out. Therefore, the translational task is calculated independently from the yaw task.

---

158 cf. Betz et al.: Concept analysis of WMDS, 2012.

159 Wolfram – virtual: Computational software program, http://www.wolfram.com/mathematica/, last access: May 30th 2014.

Force Distribution for Yaw Task

The yaw forces are necessary to generate the yaw momentum in order to achieve the yaw acceleration demanded by the MCA. Here, the wheel forces required for yaw motion are always in the horizontal plane and perpendicular to the triangle's symmetry axes, as shown in Figure 3.9.

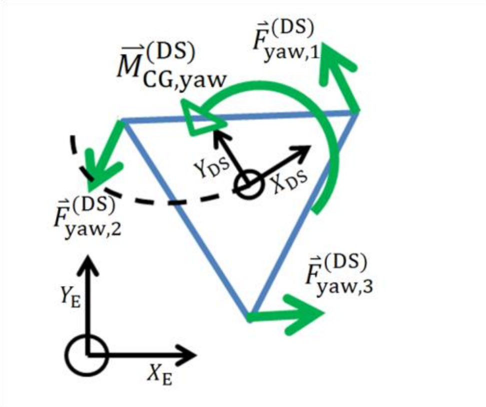

Figure 3.9: Force distribution of yaw task[160]

The force demand for the yaw task is distributed equally to the three wheels. Distributing same force magnitudes to wheels that show different wheel loads thwarts attempts to minimize friction coefficient differences between the wheels, but prevents a disturbance of the translational task. The required yaw force at each wheel for a given yaw acceleration depends on the DS's mass moment of inertia about the vertical yaw axis ($\Theta_{zz,\mathrm{DS}}$), the edge length of the equilateral triangle setup (l_t), and the yaw acceleration demand ($\ddot{\psi}_{\mathrm{DS,ref}}$) from the MCA:

$$F_{\mathrm{yaw},i} = \frac{\left|\vec{M}_{\mathrm{CG,yaw}}\right|}{\sqrt{3} \cdot l_\mathrm{t}} = \frac{\Theta_{zz,\mathrm{DS}} \cdot \ddot{\psi}_{\mathrm{DS,ref}}}{\sqrt{3} \cdot l_\mathrm{t}} \tag{26}$$

Considering the driving simulator's COS, the orientation of the yaw forces differs at each wheel as presented in Figure 3.9 but each orientation stays unchanged with respect to the simulator's COS. Splitting the yaw force at each wheel into the x- and y-components of the motion base leads to the results shown in Table 3.2.

---

[160] cf. Betz et al.: Concept analysis of WMDS, 2012.

Table 3.2: Decomposition of yaw force into components[160]

Force \ Wheel	1	2	3
$\boldsymbol{F}_{\mathbf{yaw},\boldsymbol{x},\boldsymbol{i}}$	0	$\frac{-\sqrt{3}F_{\text{yaw},i}}{2}$	$\frac{\sqrt{3}F_{\text{yaw},i}}{2}$
$\boldsymbol{F}_{\mathbf{yaw},\boldsymbol{y},\boldsymbol{i}}$	$F_{\text{yaw},i}$	$\frac{-F_{\text{yaw},i}}{2}$	$\frac{-F_{\text{yaw},i}}{2}$

Resulting Distribution of Horizontal Wheel Force

As shown in Figure 3.10, the x- and y-components of the translational and yaw task are summed up to generate a resulting force vector at each wheel. Equations (27) and (28) show the related calculations.

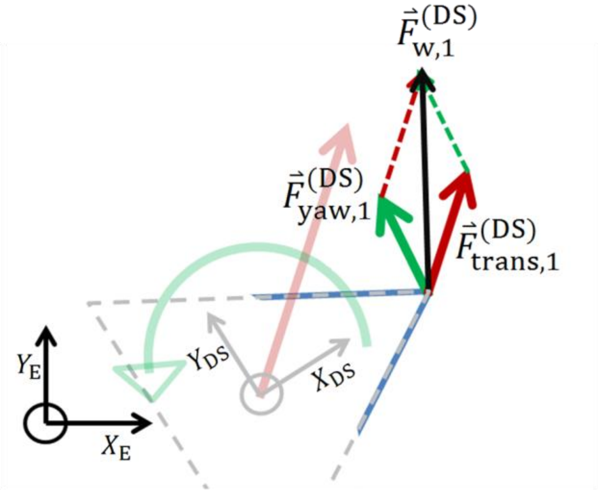

Figure 3.10: Addition of vectors of translational and yaw force[161]

$$
\begin{aligned}
F_{w,i,x} &= F_{\text{trans},i,x} + F_{\text{yaw},i,x} \\
F_{w,i,y} &= F_{\text{trans},i,y} + F_{\text{yaw},i,y}
\end{aligned}
\tag{27}
$$

$$
F_{\text{w},i} = \sqrt{F_{w,i,x}{}^{2} + F_{w,i,y}{}^{2}} \tag{28}
$$

[161] cf. Betz et al.: Concept analysis of WMDS, 2012.

3.3.2 Actuator Task of the Wheeled Motion Base

So far, the presented algorithm provides the requisite force vector for each wheel. The question arises how this force vector is created by the coordination of the available actuators. The wheel's task is defined by longitudinal and lateral force. In total, these two forces must match the previously derived force vector demand ($\vec{F}_{\mathrm{w},i}$). The longitudinal force is set in motion directly by the torque of the traction motor and heads in the longitudinal direction of the wheel's COS:

$$T_{\mathrm{w,traction},i} = F_{\mathrm{w,long},i} \cdot r_{\mathrm{w}} \tag{29}$$

The lateral force of a conventional wheel cannot be actuated directly by a motor in the same way as the longitudinal force. The lateral force of a conventional tire results from the slip angle and the tire's cornering stiffness. Hence, the lateral force is controlled by the wheel's steer angle. Furthermore, it should be underscored that providing lateral force on a horizontal plane is only possible if and only if the wheel hub is in motion. Otherwise, there is no velocity vector and consequently no slip angle is possible. These circumstances show that the lateral tire force depends on the slip angle and thus is subject to the wheel's orientation and velocity state ($\vec{v}_i$ and δ_i). The necessary DS states are calculated using a simplified kinematic model, which assumes ideal rolling tires and disregards slip angles. Thus, the orientation of the wheel is expected to orient in the direction of predicted motion.

Kinematic Model of WMDS

This method does not require knowledge of the tire properties and is commonly used in robotics[162] because it is valid for low dynamic motion where only a low degree of slip occurs that can be corrected by closed-loop approaches. The tire is modeled to behave as if it has infinite cornering stiffness. The method disregards slip effects. As a result, transient motion causes error.

As described previously, it is possible to divide simulator motion into translational and yaw parts as shown in Figure 3.11.

[162] Betz et al.: Driving dynamics control of WMDS, 2013.

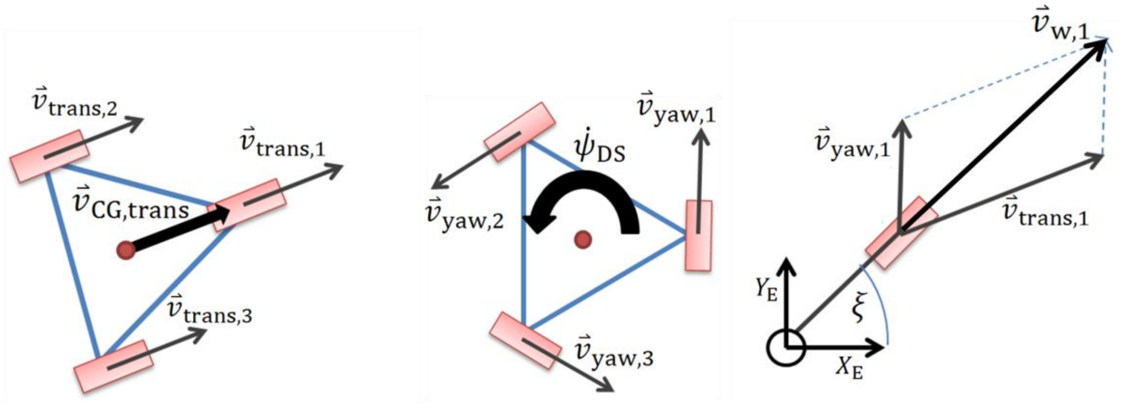

Figure 3.11: Kinematic model of the WMDS concept regarding velocities[163]

In translational motion, all velocity vectors $\vec{v}_{\mathrm{trans},i}$ face in the same direction and have magnitude equal to the CG's motion (Figure 3.11, left). When considering only yaw motion, the velocities $\vec{v}_{\mathrm{yaw},i}$ face perpendicular to the triangle's symmetry axes, rotating the simulator around its CG (Figure 3.11, center). The vectors $\vec{v}_{\mathrm{yaw},i}$ are of equal magnitude, which is calculated from the yaw angle rate ($\dot{\psi}_{\mathrm{DS}}$) and the lever arm from the wheel contact patch to the yaw axis (r_{drive}):

$$v_{\mathrm{yaw}} = \dot{\psi}_{\mathrm{DS}} \cdot r_{\mathrm{drive}} \tag{30}$$

As shown in Figure 3.11 (right) and Figure 3.12, adding both vectors returns the resulting velocity vector of each wheel ($\vec{v}_{\mathrm{w},i}$, equation (31)) as well as the angle of the wheel to the origin (ξ_i). By using the yaw angle of the motion base (ψ_{DS}), the steer angle ($\delta_{\mathrm{kin},i}$) and its derivatives are obtained as shown in equation (32).

$$\vec{v}_{\mathrm{w},i} = \vec{v}_{\mathrm{trans},i} + \vec{v}_{\mathrm{yaw},i} \tag{31}$$

$$\delta_{\mathrm{w,kin},i} = \psi_{\mathrm{DS}} - \xi_i \tag{32}$$

[163] cf. Betz et al.: Concept analysis of WMDS, 2012.

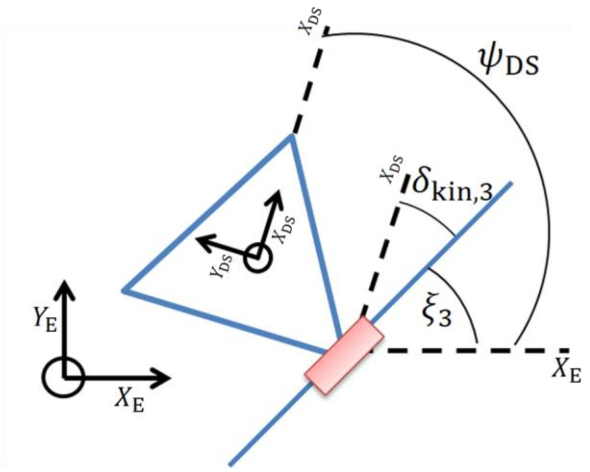

Figure 3.12: Kinematic model of the WMDS concept regarding angles[164]

Slip Angle Estimation

If there is knowledge about the properties of the tire used, dynamic slip angle estimation is possible. A more plausible tire characteristic such as real cornering stiffness (c_α), is considered for predicting slip angle demand. This method represents a feed-forward approach. The relationship used between lateral force and slip angle (equation (33)) might be represented in as much detail as necessary. For this work, a linear behavior is implemented using the same cornering stiffness as is used later in the vehicle dynamics simulation of the WMDS (section 4.2). The required slip angle and the matching torque of the traction motor must be identified regarding the DS states. This identification is done by a numerical root-finding algorithm. The slip angle of the wheel is varied in discrete steps without interpolation. As shown by equation (35), the lateral force (equation (33)) resulting from the varied slip angles is compared to the lateral component (equation (34)) of the demanded force vector with respect to the COS of the wheel. In accordance with equation (36), the set of the slip angle α is determined that satisfies equation (35). The geometric relation is presented in Figure 3.13.

$$F_{\alpha,i} = c_\alpha \alpha_i \tag{33}$$

$$F_{y,i} = |\vec{F}_{\mathrm{w},i}| \cdot \sin\left(\rho_i - \delta_{\mathrm{w,kin},i} - \alpha_i\right) \tag{34}$$

$$F_{\alpha,i} = F_{y,i} \tag{35}$$

[164] cf. Betz et al.: Concept analysis of WMDS, 2012.

$$\{\alpha_i : F_{y,i} = F_{\alpha,i}\} \tag{36}$$

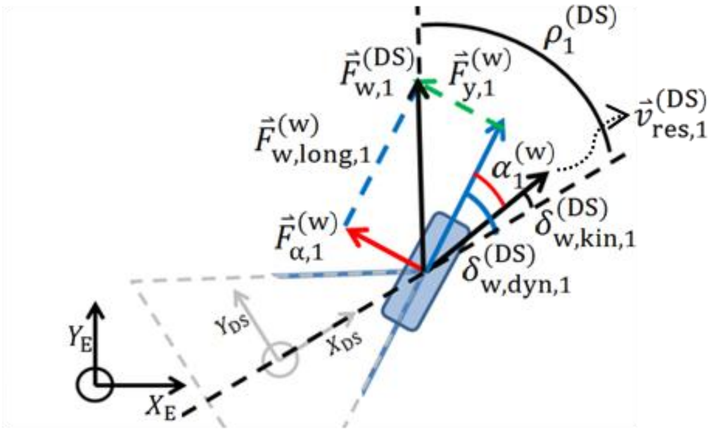

Figure 3.13: Geometric relation of wheel orientation[165]

Resulting Actuator Tasks

After determining the required lateral force, the missing longitudinal force is calculated which results in the requisite force vector when superposed with lateral wheel force. The longitudinal component of the requisite force vector is calculated with respect to the COS of the wheel (equation (37) and Figure 3.13).

$$F_{w,long,i} = |\vec{F}_{w,i}| \cdot \cos\left(\rho_i - \delta_{w,kin,i} - \alpha_i\right) \tag{37}$$

It should be taken into account that this approach represents a simplification of slip effects and disregards dependencies of longitudinal and lateral slip. These dependencies can be satisfied by combined slip approaches if necessary. The steer angle is calculated using a 4-quadrant function of arctangent (atan2):

$$\delta_{w,kin,i} = \mathrm{atan2}\left(v_{w,y,i}, v_{w,x,i}\right) \tag{38}$$

$$\delta_{w,dyn,i} = \delta_{w,kin,i} + \alpha_i \tag{39}$$

[165] cf. Betz et al.: Driving dynamics control of WMDS, 2013.

3.3.3 System Power and Energy Model

At the current level of research, aspects like visual systems and data transfer are not considered. The estimation of energy and power demand is focused on motion of the wheeled motion base only. The energy consumers under consideration are the traction and steer motors. A maximum regenerating power of 29 kW is assumed, as is used for quick charging batteries of electric vehicles[166]. An efficiency coefficient of $\eta = 0.8$ for battery power to wheel-hub torque and vice versa is applied. The calculations are performed in accordance with equations (40) to (44).

$$P_{\mathrm{w,traction},i} = v_{\mathrm{w,long},i} \cdot F_{\mathrm{w,long},i} \tag{40}$$

The traction power is a straightforward approach of the longitudinal velocity and force of the wheel. The lateral power results from the control of the wheel's slip angle. The steer motor controls the lateral force by the generated slip angle. The power demand of the steer motors is mainly caused by the angular acceleration and the moment of inertia about the steer axis. The additional effects

- drill moment,
- aligning torque, and
- friction of the drive path of the steer unit

are disregarded. The drill moment mainly occurs in standstill as it only takes place at driveaway. The drill moment significantly drops with the wheel's rotational velocity as familiar from vehicles without power steering. The aligning torque is disregarded because the chosen setup has no geometrical caster, and no verified information about the change of the force's working point exists for the chosen press-on band tires. The high vertical tire stiffness causes a small tire patch; thus, little aligning torque is expected compared to pneumatic tires. Therefore, in the present work, the steer power is estimated according to equation (41). Nevertheless, these topics need to be researched further by hardware testing in future research.

$$P_{\mathrm{w,steer},i} = \dot{\delta}_i \ddot{\delta}_i \theta_{\mathrm{steer}} \tag{41}$$

The total power is derived by summing up the power of all traction and steer motors used:

$$P = \sum_{1}^{i} P_{\mathrm{w,traction},i} + \sum_{1}^{i} P_{\mathrm{w,steer},i} \tag{42}$$

The energy is calculated by integrating the power signals while taking constraints like degree of efficiency and maximum regenerating power of the battery into account:

[166] Knauer: Opel Ampera, 2011.

$$E = \int P_{\text{in}}\,dt, P_{\text{in}} = \begin{cases} P\dfrac{1}{\eta}\,, P > 0;\ \eta = 0.8 \\ P \cdot \eta\,, P_{\text{min}} \le P \le 0;\ \eta = 0.8 \\ P_{\text{min}}\,, P \le P_{\text{min}};\ P_{\text{min}} = 29\ \text{kW} \end{cases} \tag{43}$$

In order to evaluate the operating time of the motion base, the energy demand is presented as average power demand:

$$P_{\text{mean}} = \frac{E}{\Delta t} \tag{44}$$

3.4 Control Architecture

The aim of the control is to improve the driving experience of a subject sitting on top of the platform. As mentioned previously, humans do not perceive velocity directly; the driving experience in DS is represented by acceleration forces. Therefore, the presented control setup is implemented on the acceleration level and differs from common control setups which are usually trajectory based.[167,168] The closed-loop control shows feedback of the actual control signals a_x, a_y, and $\ddot{\psi}$. The feedback control of these signals is implemented as shown in Figure 3.14. The coordinate transformation between the vehicle COS and the earth fixed COS (V2E and E2V) is necessary in order to integrate the velocity from the acceleration signal. The choice of the control parameters of the PI-controller for the WMDS depends on a trade-off between system dynamics and stability. The selected parameters of the PI-controller are presented with the test maneuver they are tuned for (Table 4.1 in section 4.1.2). The concept presented in this section was published in Betz et al.[169].

[167] Meulen: Validation VeHIL, 2004.

[168] de Schrihver: Over-actuated mobil robot VeHIL, 2009.

[169] Betz et al.: Driving dynamics control of WMDS, 2013.

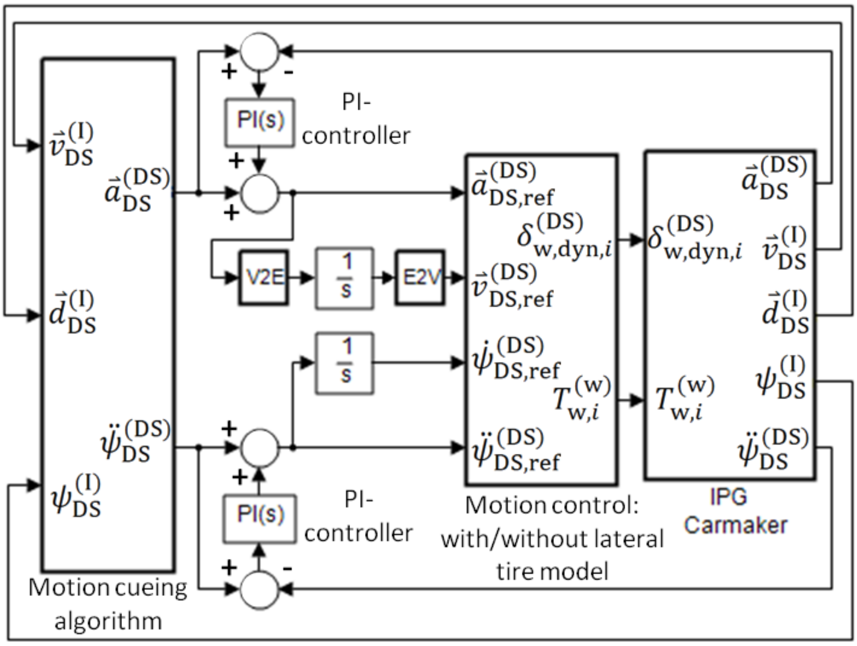

Figure 3.14: Block diagram of the control architecture[170]

In total, four control setups are designed. All setups are based on the block diagram of Figure 3.14 and the corresponding algorithms of sections 3.2 and 3.3. The control setups differ in two properties – with/without PI-controller (open-loop/closed-loop) and model with/without lateral tire dynamics. By varying these properties, the four setups are derived as shown in Table 3.3. It is expected that the impact of the more advanced control setups will increase with rising acceleration tasks of demanding driving maneuvers. This expectation derives from the increased slip level caused by higher acceleration amplitudes.

Table 3.3: Applied control setups

	Open-Loop Control	**Closed-Loop Control**
No model of lateral tire dynamics	kinOLC	kinCLC
Linear model of lateral tire dynamics	dynOLC	dynCLC

[170] cf. Betz et al.: Driving dynamics control of WMDS, 2013.

3.5 Architecture and Design of the WMDS

The present project enables hardware testing and prepares for validating the analytical and numerical results as well as the safety architecture. The hardware prototype is realized for validating purposes only. Thus, some properties are scaled. The design of the following subsections applies for the representative WMDS in general. The derived specific results for the created prototype are summarized at the end of each subsection. The final structure is shown in Figure 3.15. The position of the cabin is illustrated by a racing cockpit from the entertainment industry. Because it does not encapsulate the vehicle mock-up, it is not intended to carry subjects for DS studies. Before any work toward enhancement of the cabin of the hardware prototype should take place, open questions with respect to WMDS feasibility must be answered. To reach the overall objective of the WMDS, the presented setup with the racing cockpit is used for test drives with measuring equipment and for the experience of important properties of the wheeled motion base by expert drivers.

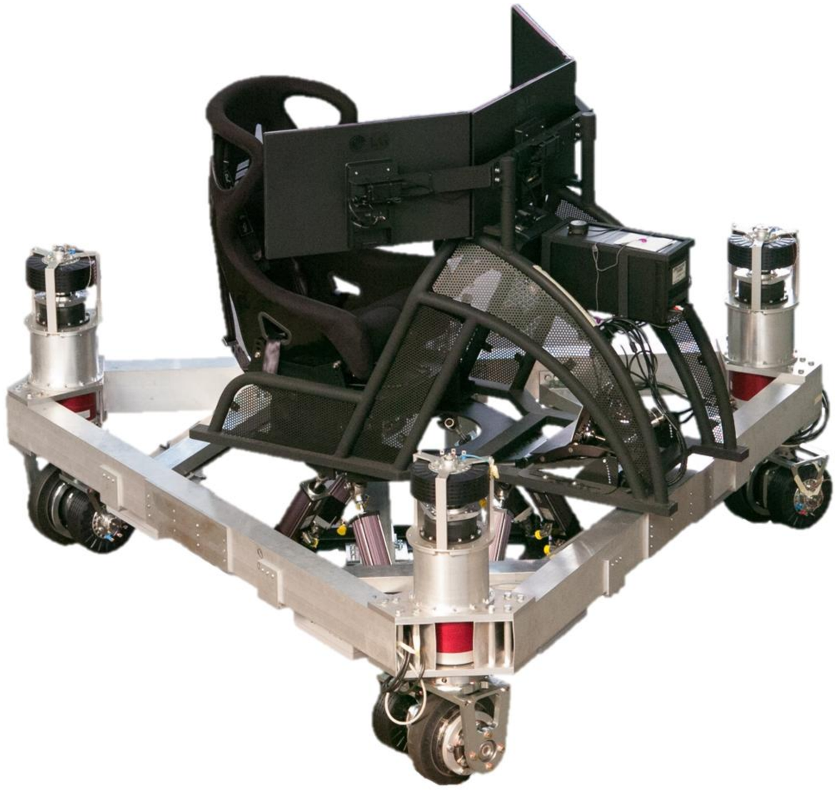

Figure 3.15: Picture of the hardware prototype of the representative WMDS

3.5.1 System Architecture

The decomposed WMDS is presented in the following figures. The system architecture in Figure 3.16 illustrates the distribution of the power signals between the system components. The power signals are distinguished by the applied voltage.

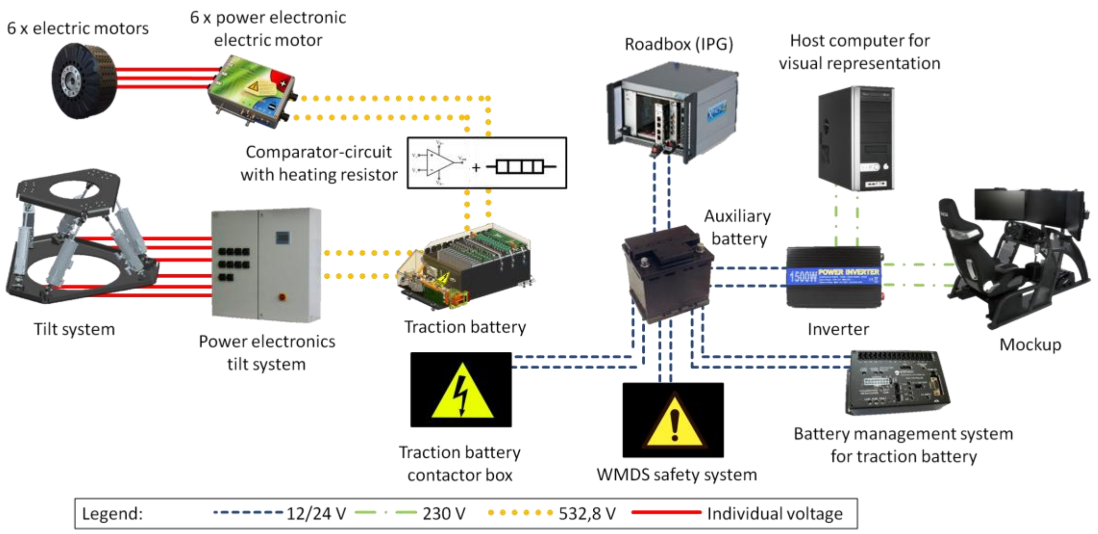

Figure 3.16: WMDS architecture of the power signals[171]

In Figure 3.17 the system architecture of the data transfer is presented. The utilized information standards are shown.

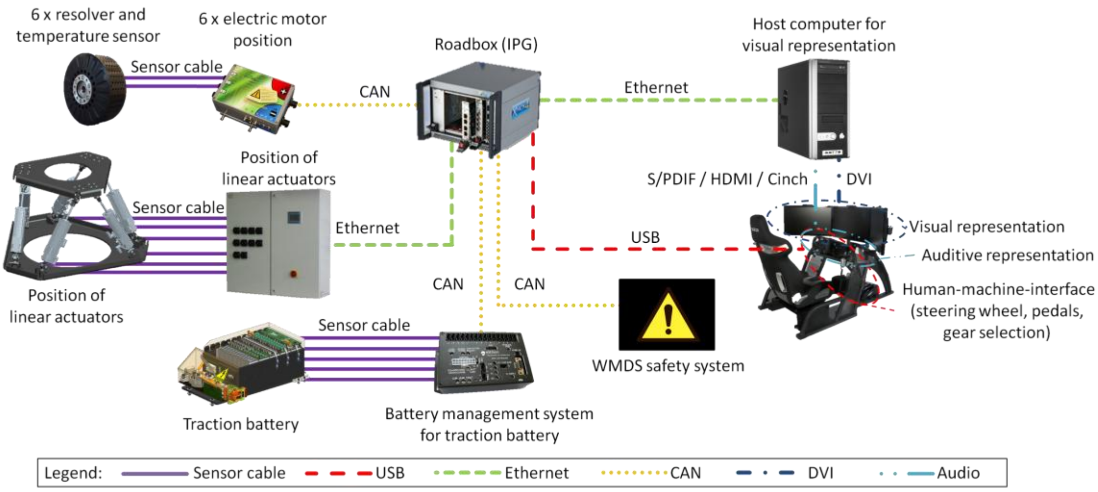

Figure 3.17: WMDS architecture of the information signals[171]

[171] cf. Wagner: WMDS, Master's thesis supervised by Betz, 2013.

3.5.2 Assembly of the Drive Unit

The information presented in this subsection was presented in Wagner et al.[172], if not referenced differently. As introduced in Figure 3.1 (section 3.1, p. 47), the assembly provides three drive units. Each drive unit (C) consists of a steer unit (B) and a traction unit (A) in order to perform horizontal tire forces by wheel hub torque and slip angle. The assembly of the drive unit is illustrated in Figure 3.18. In general, the body movement of a DS (heave, pitch and roll) must suit the driving maneuver of the virtual vehicle. Hence, the body movements of a DS that are caused by inertial forces are strongly unwanted. In order to counteract these unwanted body movements press-on band tires are applied. These tires are known from forklift trucks and provide increased vertical spring stiffness over conventional pneumatic tires. Thus the unwanted body movement is reduced significantly.

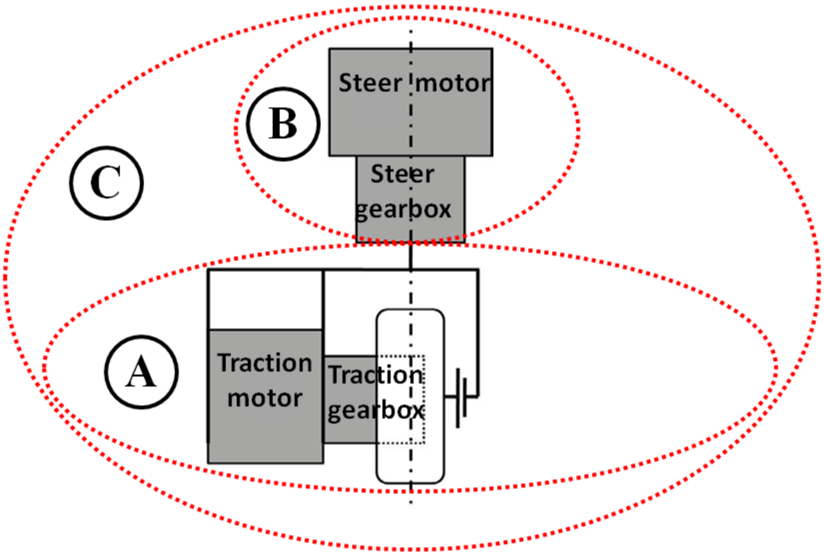

Figure 3.18: Assembly of the components of the drive unit[173]

The dimensioning of the drive unit must cope with the validating purpose of the hardware prototype. The realized acceleration performance is determined to 1 *g* according to the Daimler DS because the Daimler DS provides highest acceleration amplitudes of all introduced DS[174]. The maximum operating velocity is determined to provide peak acceleration phases of about 1 s. Increased acceleration phases are not expected to provide

[172] Wagner et al.: Conception of a WMDS, 2014.

[173] In the style of a Figure of a student project advised by the author: ADP 46/13, p. 11.

[174] Higher acceleration performance is only provided by centrifuge systems but is not used for simulating maneuvers of passenger vehicles for two reasons: First, vehicle dynamics is limited by tire friction forces to about 1 *g*; second, the workspace of centrifuge systems that are used for DS is strongly limited (Wentink: centrifuge curve driving, 2008).

additional gain of system understanding but might be of interest for future DS applications. The dimensioning of the steer motor is more complicated because the performance demands are hardly researched concerning tolerated response time and the rare occurrence of demanding steer tasks as presented later in section 5.2.3. Fang et al.[175] specify the phase delay of common, enhanced DS to be in a range of 32 to 157 ms. The presented range gives a rough estimate of the dimension of the tolerated response delay. The steer unit of the hardware prototype utilizes the same motor and gearbox as the traction unit. This decision is made based on three reasons:

- There is insufficient information concerning tolerated response delay for acceleration simulation.
- Reduced effort is realized by utilizing same motors for traction and steer task.
- The expected steer performance of the utilized components allows conducting the worst case 90° steer step within about 100 ms[176]. The performance created is in the range introduced by Fang et al.[177] and seems to be promising for learning more about the steer task and the tolerated response delay in future hardware tests.

The specifications of the utilized components of the prototypical WMDS are presented in Table 3.4.

[175] Fang et al.: Motion cueing delay, 2011.

[176] The calculation is according to the eq. (75), (76), and (77) with the parameters of Table 3.4 and Table 3.8 ($T_{\mathrm{steer,max}} = 1{,}200$ Nm; $\Theta_{zz,\mathrm{steer}} = 2.1\ \mathrm{kgm}^2$).

[177] Fang et al.: Motion cueing delay, 2011.

Table 3.4: Specifications of the drive unit of the final prototype[178]

Property	**Unit**	**Value**
Electric motors[179]		
Peak power	kW	100
Peak torque	Nm	240
Mass	kg	11.8
Gearbox[180]		
Transmission ratio	./.	5
Peak torque all-time	Nm	1200
Peak torque short-time	Nm	1500
Mass	kg	12.9
Power electronics[181]		
Rated supply voltage	V (DC)	700
Rated output voltage	V (AC)	to 450
Continuous current	A	125
Peak current	A	250
Mass	kg	5.8
Accumulator (Lithium-Polymer)		
Number of cells	./.	144
Maximum voltage	V (DC)	604,8
Nominal voltage	V (DC)	532,8
Capacity	Ah	10
Mass	kg	35
Tire[182]		
Radius	m	0.15
Width	m	0.075
Vertical tire stiffness[183]	N/mm	1036

[178] cf. Wagner et al.: Conception of a WMDS, 2014.

[179] ENSTROJ – virtual: EMRAX AC, http://www.enstroj.si/, last access: May 27th 2014.

[180] Neugart – virtual: PLFN 140-5, http://www.neugart.de/index.php/de, last access: May 27th 2014.

[181] Unitek – virtual: BAMOCAR-D3-700-250, http://www.unitek-online.de/, last access: May 27th 2014.

[182] Gumasol – virtual: Press-on band tire, http://www.gumasol.de/, last access: May 27th 2014.

[183] Vertical tire stiffness according to experimental test on the GUMASOL test facility (28.06.2013): 1036 N/mm (linearized spring rate).

3.5.3 Traction Battery

The traction battery used is a clone of the one used in the theta 2013 racing car of the TU Darmstadt Racing Team e.V. (DART)[184]. The Formula Student Electric racing car utilizes the same propulsion and power electronics; hence, the battery clone is suitable for the validating purpose of the present work. The battery meets the safety standards of the Formula Student Electric regulation[185,186]. The specifications are presented in Table 3.4. The traction battery is illustrated in Figure 3.19. Further details concerning internal setup and design can be found in DART[184].

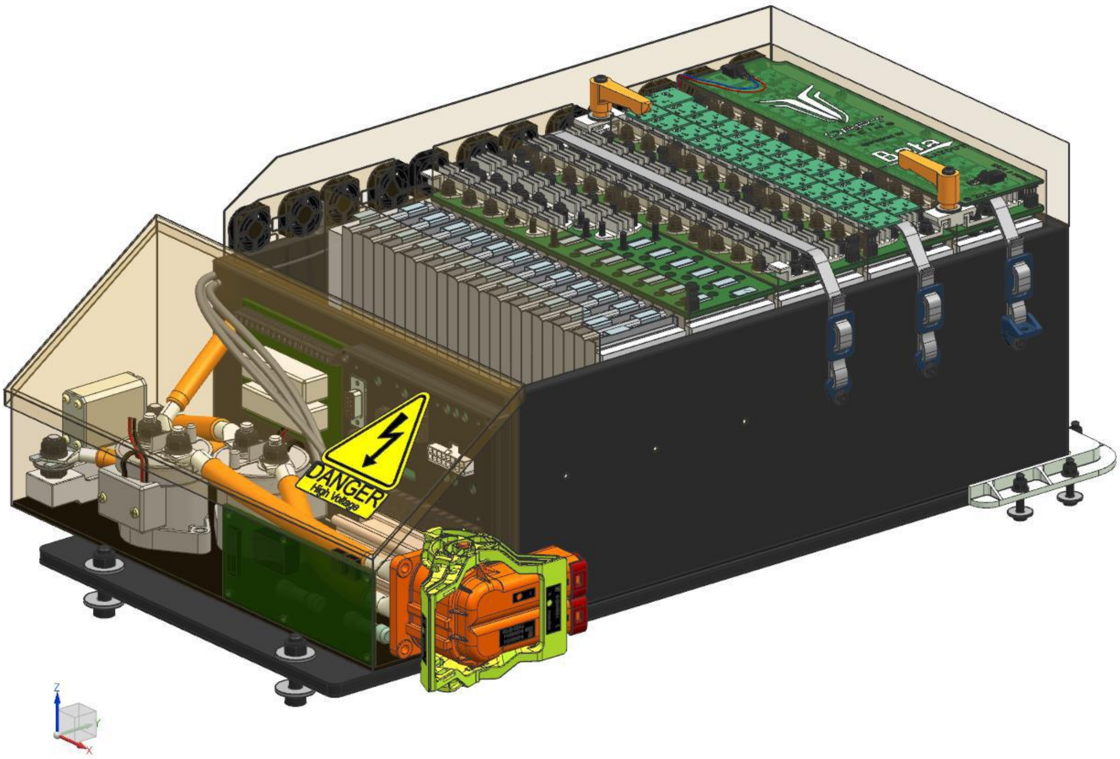

Figure 3.19: CAD assembly of the utilized traction battery[184]

3.5.4 Geometric Dimensioning of the WMDS

The sizing of the motion base is patterned on the principles of rollover prevention. At maximum acceleration it must be assured that the WMDS does not roll over. Rollover

---

[184] DART: Electric system form, 2013.

[185] Formula Student Electric – virtual: rules 2013, http://www.formulastudent.de/fse/2013/rules/, 2013, last access: May 28th 2014.

[186] SAE International – virtual: Rules Formula Electric, http://students.sae.org/cds/formulaseries/, 2013, last access: May 30th 2014.

can be put on the same level as wheel lift, which occurs when the wheel load becomes smaller than zero. The chosen triangular setup is only one imaginable setup. Among all setups utilizing more than three wheels, the triangular setup has an unambiguous wheel load distribution, because the number of wheel loads matches the number of unknown variables and available equations (see equation (21), p. 61). The disadvantage of the increased footprint (for equal rollover prevention), compared to setups with more than three wheels, is negligible because the typical workspace of a WMDS is significantly larger by more than one magnitude as presented later in section 5.2.1. Figure 3.20 illustrates the geometrical relationships. The necessary footprint of the equilateral triangle becomes a function of the maximum friction coefficient and the height of the CG. The equation is derived by setting up the balance of forces and calculating the momentum equilibrium around point 2.

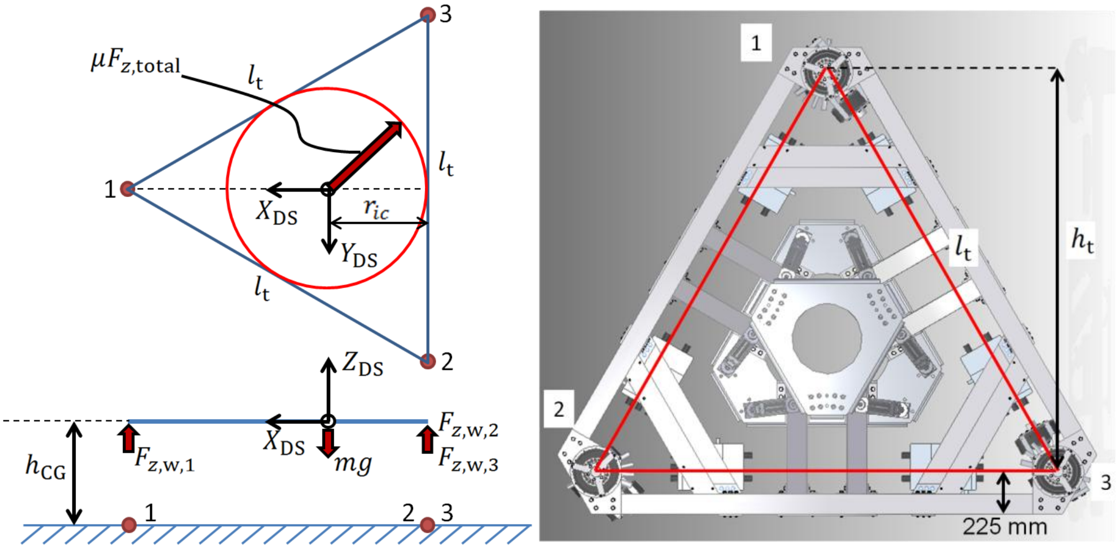

Figure 3.20: Relationship of sizing and rollover[187]

$$\begin{gathered}\sum_{(2)} M = 0 = m \cdot g \cdot (\mu_{max} \cdot h_{CG} - r_{ic}) + h_t \cdot F_{z,wheel,1} \\ r_{ic} = \frac{1}{3} h_t = \frac{1}{2\sqrt{3}} l_t \\ h_t = \frac{\sqrt{3}}{2} l_t\end{gathered} \tag{45}$$

Applying the geometric relationship of Figure 3.20, rollover stability is ensured by complying with the following equation:

[187] cf. Wagner: WMDS, Master's thesis supervised by Betz, 2013.

$$F_{z,wheel,1} = \frac{2 \cdot m \cdot g \cdot \left(\frac{1}{2\sqrt{3}} l_t - \mu_{max} \cdot h_{CG}\right)}{\sqrt{3} \cdot l_t} > 0 \qquad (46)$$
$$\rightarrow l_t > 2\sqrt{3} \cdot \mu_{max} \cdot h_{CG}$$

The geometric relationships of equations (45) and (46) lead to relevant information about mass, height of CG, and geometric design. The relationships are applied for the structure of the WMDS prototype. The results are summarized in Table 3.5 and Table 3.6.

Table 3.5: Mass distribution of the final WMDS prototype

Component	**Mass in kg**	**Height of CG in mm**
Wheeled motion base	576	428
Hexapod	145	310
Mock-up	72	1246
Subject	101	1146
Traction battery	34	252
Power electronics traction and steer	49	329
Power electronics hexapod	100	250
Control and simulation computers	26	551
WMDS safety system	200	331
	Σ 1302	481

Table 3.6: Geometric specifications of the final WMDS prototype

Parameter	**Unit**	**Value**
h_{CG}	mm	481
μ_{max}	./.	1
l_{t}	mm	2300
h_{t}	mm	1992
Safety factor against rollover	./.	1.38

3.5.5 Specifications of the Final WMDS Prototype and Derived Estimation for the Full-Scale WMDS

The differences between the prototype and a full WMDS with enhanced visual representation for DS studies result mainly from the differences in DS cabins. While the prototype's cabin is simplified as an unenclosed mock-up, the full DS requires an encapsulated cabin with an enhanced visual system. In order to consider the constraints of the full WMDS setup for the feasibility analysis, a mass estimation of the required WMDS cabin is made. The estimation is based on the PSA DS[188] as discussed in Betz et al.[189]. The mass distribution of the cabin of the PSA DS is adapted to the full-scale WMDS according to Table 3.7.

Table 3.7: Mass distribution of the DS cabin[189]

Major components of cabin	**PSA[190] in kg**	**Estimation of full-scale WMDS cabin in kg**	
		Best-case	**Worst-case**
Visual system (projectors etc.) including retro vision	30	10	30
Composite honeycomb structure	250	150	210
Fixation device, bushings	40	30	30
Vehicle cab (body shell)	160	0	100
Vehicle standard equipment (dashboards, seats, etc.)	150	40	100
Acoustic reduction material	30	30	30
Passive force feedback system	30	30	30
Steering wheel feedback system	20	20	20
Overall cabin mass	710	310	550

A worst and best case (WC and BC) estimation is assumed. The worst case results mainly from a conservative point of view, which utilizes state-of-the-art visual systems (projector and screen). The best case results from a perspective of what could be achieved in the near future when using enhanced head mounted displays and virtual reality. The honeycomb structure is the heaviest component of the cabin and must provide sufficient stiffness for moving its first eigenfrequency above the operating frequency bandwidth.[191] Hence, its mass decreases with reduced cabin mass and size. The body shell and vehicle standard equipment is reduced to its minimum. The technological progress in the field of visual systems is expected to compensate for leaking impression caused by the simplified vehicle mock-up. The overall mass reduction allows reducing the expected mass of fixation devices and bushings. Further components listed in Table 3.7 are transferred unchanged. In total the cabin shows an expected mass of about 310 (BC) to 550 kg (WC), depending on the degree of virtualization discussed.

The difference in cabin mass should be considered for the conducted feasibility analysis because it influences some of the evaluated falsification aspects such as the power and energy demand (section 1.2). The increase of cabin mass influences the dimensioning of

---

[188] Chapron; Colinot: PSA DS, 2007.

[189] Betz et al.: Motion analysis of WMDS, 2012.

[190] Chapron; Colinot: PSA DS, 2007.

[191] Murano et al.: Toyota DS, 2009.

the other WMDS components which are then affected themselves and cause a disproportional rise of mass. The final increase is the result of an iterative process which is not conducted for the present estimation due to its minor importance for the focus of research – the general feasibility of a WMDS. Instead, the estimation assumes a linear increase of the overall system mass because it must be considered that the prototype itself is an exemplary structure that contains several unfulfilled possibilities for mass reduction. Considering the mass of the prototype's mock-up (72 kg), the WC assumption leads to an additional 478 kg (ratio: $(1302\ \mathrm{kg} + 478\ \mathrm{kg})\ /\ (1302\ \ \mathrm{kg}) = 1.4$) while the BC causes an increase of only 238 kg (ratio: $(1182\ \mathrm{kg} + 238\ \mathrm{kg})\ /\ (1182\ \ \mathrm{kg}) = 1.2$). The final system performance of the created WMDS prototype and the expected full DS setups are summarized in Table 3.8. The results of section 5.1 and 5.2 are based on this information.

Table 3.8: Specifications of the final WMDS prototype and the full-scale WMDS

Properties	**Prototype with reduced visual representation system for validation purpose** (motion base research)	**Estimation of Full-Scale WMDS with enhanced visual representation system for DS studies** (DS application: studies with test person)	
		BC	**WC**
Additional cabin mass	-	238 kg	478 kg
Overall mass	1,302 kg	1,786 kg[192]	2,272 kg[193]
Height of CG	0.48 m	Factor: 1.2	Factor: 1.4
l_t	2.3 m	Factor: 1.2	Factor: 1.4
$\Theta_{zz,\mathrm{DS}}$	1,177 kgm²	Factor: 1.2	Factor: 1.4
$\Theta_{zz,\mathrm{steer}}$	2.1 kgm²	Factor: 1.2	Factor: 1.4
Wheel radius	0.15 m	Factor: 1	Factor: 1
Traction motor power	300 kW (Peak-Sum)	see section 5	see section 5
Steering motor	300 kW (Peak-Sum)	see section 5	see section 5
90° steer step delay	< 0.1 s	Factor: 1	Factor: 1
Max. acceleration	> 1 g	see section 5	see section 5
Max. velocity	> 10 m/s	see section 5	see section 5

3.5.6 Safety Architecture

The safety architecture is a vital element of a DS. It must cope with carrying subjects on a motion base while providing safety for the users, the system, and the surroundings. The unbound characteristic of the WMDS increases the complexity of the safety archi-

[192] $(1{,}302\ \mathrm{kg} - 72\ \mathrm{kg}) \cdot 1.2 + 310\ \mathrm{kg} = 1{,}786\ \mathrm{kg}$.

[193] $(1{,}302\ \mathrm{kg} - 72\ \mathrm{kg}) \cdot 1.4 + 550\ \mathrm{kg} = 2{,}272\ \mathrm{kg}$.

tecture compared to rail guided DS. The increase arises because conventional stop dampers cannot be provided for all possible impact angles and positions of the unbound system. The requirements of the safety architecture are derived by a failure mode and effects analysis (FMEA) and the failure tree analysis (FTA). The FTA is based on a critical top event for a countermeasure found by the FMEA. The FTA is described at the end of this section whereas the FMEA is not presented because of its complexity.

Most of the components used in the prototype are themselves prototypical, little researched, or custom-made items. Hence, most components are not cleared for safety-critical applications. Even the chosen tires have been only sparsely researched although they are sourced from volume production in the forklift truck industry. These circumstances are considered in the FMEA in order to create a safety architecture that countermeasures the number of evaluated failures and allows first test drives with the WMDS prototype, which is unprecedented worldwide.

Concept Idea

The results of the FMEA lead to the conclusion that an additional system is required to avoid the potential failure modes of the overall WMDS prototype. The idea is to lift the system off the ground in order to decouple the drive units from the ground. Thus, the drive train of the WMDS is cut. This helps to prevent consequences of corrupt or incorrect motor action independently of other manifold error sources such as software, data transfer or hardware.

Still, there is a potential hazard from the kinetic energy of the WMDS as long as the system is in motion. The safety architecture relocates the contact forces from the wheels to new elements of the lifting system. In order to provide deceleration these elements must generate horizontal force in an opposite direction to the velocity vector of the contact point. It must be taken into consideration that the new contact patches assume the responsibility for rollover safety. Hence, the number (at least three) and position of the new contact patches underlie similar constraints as the positioning of the drive units (section 3.5.4). The question arises how the system lift and the decelerating force are generated. It must be stressed that no existing example of the safety architecture presented is known. Thus, the hardware structure is expected to serve as a research prototype that accelerates the gain of system understanding using hardware tests. The representative solution is introduced in the following.

Representative Solution

The representative solution utilizes friction forces of the new contact patches. Therefore, friction pads are used. These forces result from contact forces and sliding friction caused by velocity of the new contact patches with respect to the ground. According to

Figure 3.21, the contact force is created by a knee lever that is actuated by a spring. In order to ensure the lifting even in case of an electrical outage, the spring is preloaded before the start of operation and is held actively by electromagnetic clamps. If any internal functional error (software or electrical) or fault is detected, the tolerated workspace is left, or any of the emergency stops is activated, the electrical circuit of the magnets is cut and the passive lifting task is initiated. Figure 3.21 illustrates the hold (left) and emergency position (right) of the lifting system.

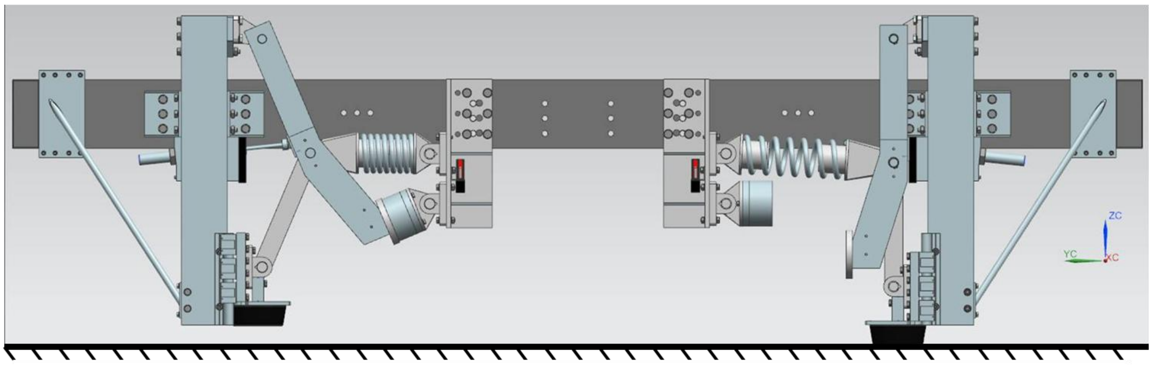

Figure 3.21: CAD model of the lifting system (left: active hold; right: discharged)

The inverting of the activation logic increases the reliability of the safety architecture but causes continuous power demand for holding the prestressed spring. The force demand for lifting the WMDS is not linear with respect to vertical displacement; thus, a conventional spring with its linear characteristics is not the most suitable component, as shown in Figure 3.22 by an exemplarily chosen spring characteristic providing the demanded force at maximum lifting stroke. In the active hold position, the lifting system has a desired initial force of zero because no contact force at the friction element exists. This relation is valid for about 10 mm because this space is required as ground clearance during operation (see left side of Figure 3.21). After the gap has been closed by the safety system, the friction pad touches the ground and lifting force is thereby generated. After the gap has been closed, the created lifting force of the friction elements reduces the wheel loads. This phase of the lifting procedure is approximated by a linear characteristic[194]. The maximum desired lifting force is derived by a worst case assumption concerning maximum wheel load (8688 N) due to assumed peak tire friction ($\mu_{max} \approx 1.45$). As soon as all wheels have lost their ground contact, no further increase of lifting force is required. However, further lift is desired to cause a defined tire-ground clearance for the emergency brake phase. As mentioned previously, the force demand discussed does not meet conventional spring characteristics (Figure 3.22). The overall stroke of the lifting system is about 39 mm.

[194] Vertical tire stiffness according to experimental test on the GUMASOL test facility (28.06.2013): 1036 N/mm (linearized spring rate).

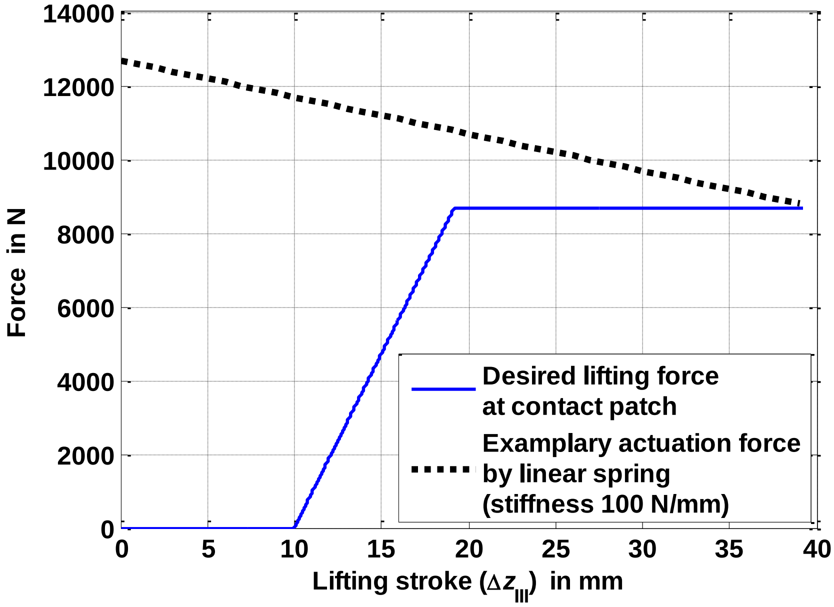

Figure 3.22: Desired lifting force at contact patch and actuation force

The desired force characteristic is imitated by a conventional spring that acts on a knee lever. The variable transmission ratio of the knee lever in combination with a linear spring results in a non-linear force characteristic with respect to the lifting stroke. According to Figure 3.23, the corresponding equations (47) to (64) apply.

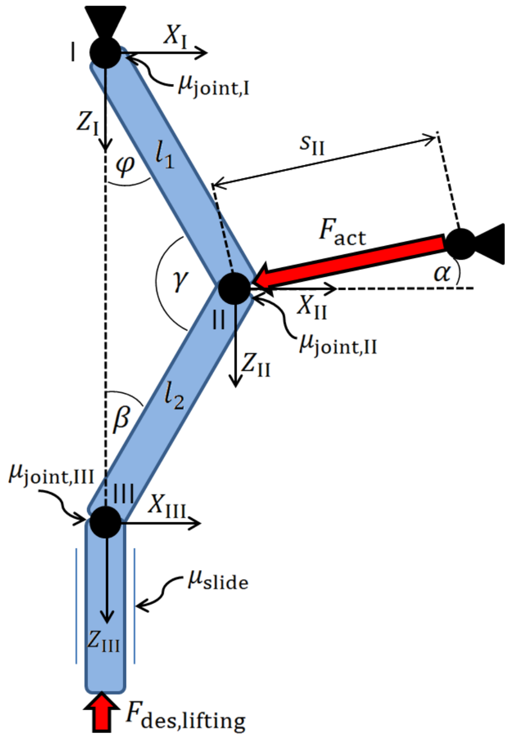

Figure 3.23: Knee lever setup with lifting force and actuation force

The following relationship is derived using the law of energy conservation and accounts only for the discharge motion of the safety architecture:

$$\mathrm{d}z_{\mathrm{III}} \cdot F_{\mathrm{des}} = F_{\mathrm{act}} \cdot \mathrm{d}s_{\mathrm{II}} \tag{47}$$

Considering friction and the angle of the actuation force, equation (47) leads to equations (48) to (52).

$$\begin{aligned} F_{\mathrm{des}} \cdot \mathrm{d}z_{\mathrm{III}} + F_{\mathrm{frict,slide}} \cdot \mathrm{d}z_{\mathrm{III}} + M_{\mathrm{fric,joint,I}} \cdot \mathrm{d}\varphi + M_{\mathrm{fric,joint,III}} \cdot \mathrm{d}\beta \\ + M_{\mathrm{fric,joint,II}} \cdot \mathrm{d}\gamma = F_{\mathrm{act}}\, [\cos(\alpha) \cdot \mathrm{d}x_{\mathrm{II}} + \sin(\alpha) \cdot \mathrm{d}z_{\mathrm{II}}] \end{aligned} \tag{48}$$

$$F_{\mathrm{frict,slide}} = \mu_{\mathrm{slide}} F_{x,\mathrm{III}} \tag{49}$$

$$M_{\mathrm{fric,joint,I}} = \mu_{\mathrm{joint}} \frac{D}{2} F_{l1} \tag{50}$$ [195]

$$M_{\mathrm{fric,joint,II}} = \mu_{\mathrm{joint}} \frac{D}{2} F_{\mathrm{act}} \tag{51}$$ [195]

$$M_{\mathrm{fric,joint,III}} = \mu_{\mathrm{joint}} \frac{D}{2} F_{l2} \tag{52}$$ [195]

The unknown forces of equation (53) (54) and (55) are derived by a free-body diagram in the appendix F.2:

$$F_{x,\mathrm{III}} = F_{\mathrm{act}}(\cos(\alpha) - u_1) \tag{53}$$

$$F_{l1} = F_{\mathrm{act}} u_2 + F_{\mathrm{des}} \cos(\varphi) \tag{54}$$

$$F_{l2} = F_{\mathrm{act}} u_3 + F_{\mathrm{des}} \cos(\beta) \tag{55}$$

$$u_1 = \frac{\cos(\alpha + \beta)}{\cos(\varphi)\, l_1 + \cos(\beta)\, l_2} l_2 \tag{56}$$

$$u_2 = \sin(\varphi) u_1 + \cos(\varphi) \cdot (\mu_{\mathrm{slide}}(\cos(\alpha) - u_1) - \sin(\alpha)) \tag{57}$$

$$u_3 = (\cos(\alpha) - u_1)(\sin(\beta) + \mu_{\mathrm{slide}} \cos(\beta)) \tag{58}$$

[195] Kerle et al.: Gear technology, p. 119, 2012.

Equations (48) to (58) lead to the final relation of the actuation force (59). The differential displacements are unambiguously related by geometrical constraints of the knee lever and result in variable transmission with respect to the state of the knee lever – φ (equations (60) to (64)).

$$F_{\mathrm{act}} = \frac{F_{\mathrm{des}}\left[\mathrm{d}z_{\mathrm{III}} + \mu_{\mathrm{joint}}\frac{D}{2}(\cos(\beta)\,\mathrm{d}\beta + \mathrm{d}\varphi)\right]}{\cos(\alpha)\mathrm{d}x_{\mathrm{II}} + \sin(\alpha)\mathrm{d}z_{\mathrm{II}} - \mu_{\mathrm{slide}}(\cos\,(\alpha) - u_1)\mathrm{d}z_{\mathrm{III}} - \mu_{\mathrm{joint}}\frac{D}{2}[u_2 \cdot \mathrm{d}\varphi + u_3 \cdot \mathrm{d}\beta + d\gamma]} \tag{59}$$

$$x_{\mathrm{II}} = \sin(\varphi)\,l_1 \tag{60}$$

$$z_{\mathrm{II}} = \cos\,(\varphi)l_1 \tag{61}$$

$$z_{\mathrm{III}} = \cos(\varphi)l_1 + \sqrt{l_2^2 - (\sin(\varphi)\,l_1)^2} \tag{62}$$

$$\sin\,(\beta) = \sin(\varphi)\frac{l_1}{l_2} \tag{63}$$

$$\gamma = \pi - \beta - \varphi \tag{64}$$

Parameter design of the safety architecture is done by numerical analysis and complies with required performance demands and relationships found:

- Required performance demands
  - Minimum required lifting stroke: 39 mm
  - Desired lifting force at contact patch: Figure 3.22 (solid graph)
- Relationships found using numerical analysis
  - The longer the knee levers, the weaker the required actuation force
  - Equal length of the levers leads to decreased spring stiffness: $l_1 = l_2$
  - The length of the levers is limited by the WMDS height and accessible linkage: $l_1 + l_2 < 540$ mm

The dimensioning is conducted based on the constraints found. The results are summarized in Table 3.9.

Table 3.9: Final design of the safety architecture

Parameter	Unit	Value
$\boldsymbol{l_1}$	mm	270
$\boldsymbol{l_2}$	mm	270
$\boldsymbol{D_{\mathrm{joint}}}$	mm	20
$\Delta \boldsymbol{s_{\mathrm{II,max}}}$	mm	102
$\boldsymbol{\alpha_{\mathrm{max}}}$	°	3
$\boldsymbol{\alpha_{\mathrm{min}}}$	°	0
$\boldsymbol{\varphi_{\mathrm{max}}}$	°	22
$\boldsymbol{\varphi_{\mathrm{min}}}$	°	0
$\boldsymbol{c_{\mathrm{spring}}}$	N/mm	67.58
$\boldsymbol{F_{\mathrm{des,max}}}$	N	8,688[196]
$\boldsymbol{F_{\mathrm{spring,max}}}$	N	6,970
$\boldsymbol{\mu_{\mathrm{slide}}}$	./.	0.1[197]
$\boldsymbol{\mu_{\mathrm{joint}}}$	./.	0.1[198]

The derived force transmission of the knee lever leads to the transformed desired lifting force (dashed graph) and actuation force of the linear spring used (dotted) as shown in Figure 3.24. The created lifting system enables the application of a conventional spring while reducing the actuation force due to the knee lever's transmission of force. Therefore, the effort for actively holding the preloaded spring is reduced significantly.

---

[196] Maximum wheel load with μ = 1.45.

[197] http://www.igus.de/wpck/2328/iglidur_Reibwerte, last access: May 2014.

[198] http://www.igus.de/wpck/2328/iglidur_Reibwerte, last access: May 2014.

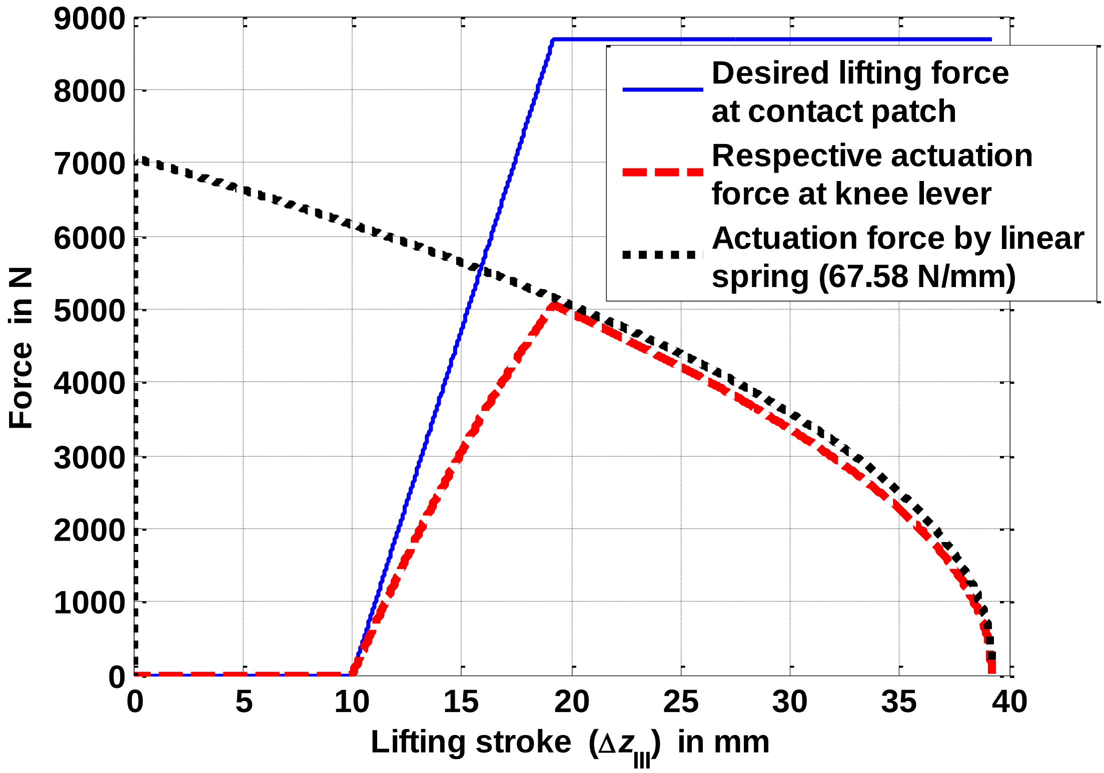

Figure 3.24: Knee lever influence on force transmission ratio (knee levers: $l_1 = l_2 = 270$ mm)

The specifications of the previously introduced safety architecture are summarized in Table 3.10.

Table 3.10: Specifications of the safety architecture

Parameter	**Unit**	**Value**
Lever arm of magnet	mm	470
Lever arm of spring	mm	250
Maximum magnetic force	N	4600
Actual magnetic force with applied anchor plate	N	4100
Supply voltage (of magnetic clamp)	V	24
Rated power (of magnetic clamp)	W	21
Maximum stroke of friction pad	mm	39
Shore hardness of friction pad	Shore A	70°
Diameter of Frictionpad	mm	125

FTA of Representative Solution

In the safety architecture, the friction force created as well as the support force of the mountings are subject to friction coefficient, contact force, and force transmission. Therefore, the top event of the FTA must treat the event chain of these forces. The result of the FTA is presented in Figure 3.25.

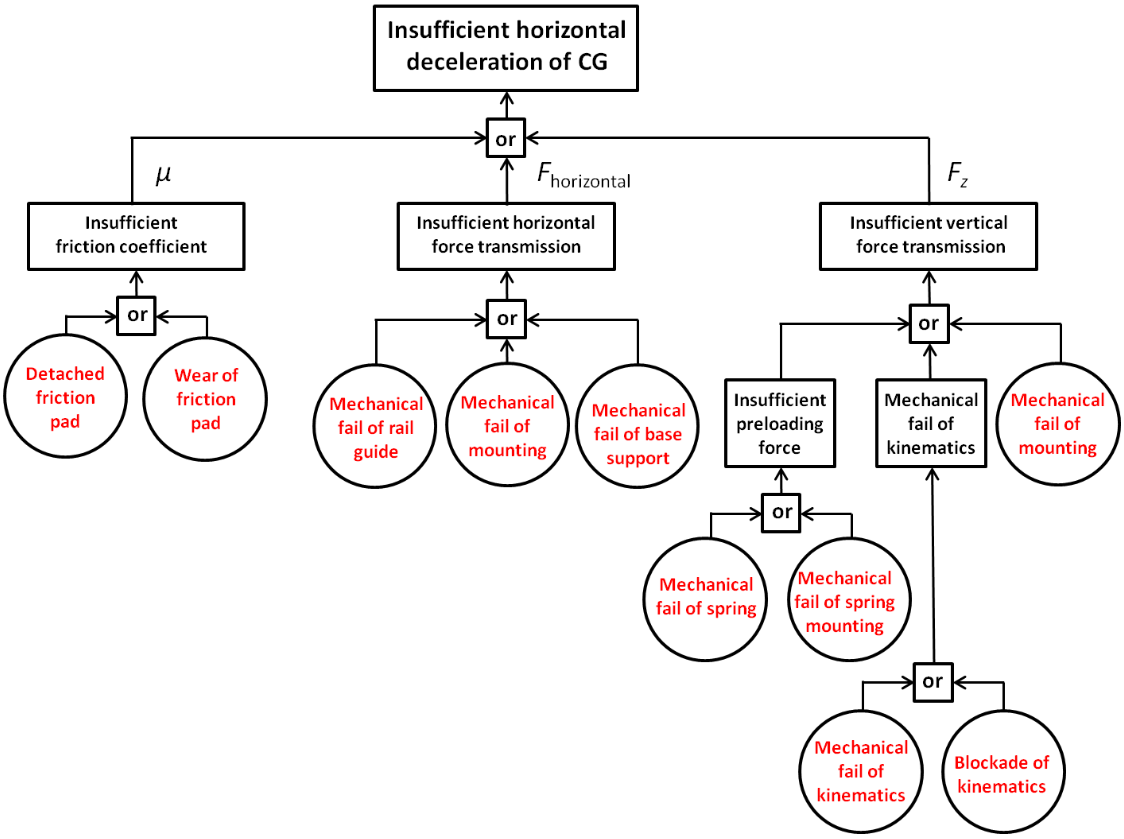

Figure 3.25: FTA of critical top event

The controllability of the critical failures that cause the top event is realized by safety factors in the dimensioning process and a redundancy of the utilized number of lifting systems. Hence, six lifting systems are applied (two at each edge of the triangle) instead of the minimum required number of three systems.

4 Evaluation Tools

4.1 Test Maneuver

4.1.1 Single Test Maneuver – T-Junction

The selected traffic maneuver is introduced in the motivation of the present work (section 1.1, Figure 1.1). It is a representative 90° turn which incorporates approaching and leaving the intersection. The maneuver leads to high DS requirements because it causes the acceleration vector to turn by about 90° yaw angle resulting in significant horizontal motion demand. The maneuver is used to determine DS motion requirements for a common urban traffic situation of passenger cars. Thus, an MCA in the aforementioned form of section 3.2 is applied. The initial velocity is 50 km/h in accordance with common speed limitations of urban traffic. The chosen deceleration and acceleration for approaching and leaving the intersection is ±3 m/s² according to appendix C.1, Figure 6.2[199]. The reference signals are calculated and presented in Figure 4.1. The selected corner radius of 10 m corresponds to the minimum allowed radius for urban cornering on access roads with speed limits below 50 km/h.[200] The applied parameterization of the MCA is commensurate with section 3.2.

[199] Murano et al.: Toyota DS, 2009.

[200] RAST06: Guidelines for the construction of roads, p. 76, 2006.

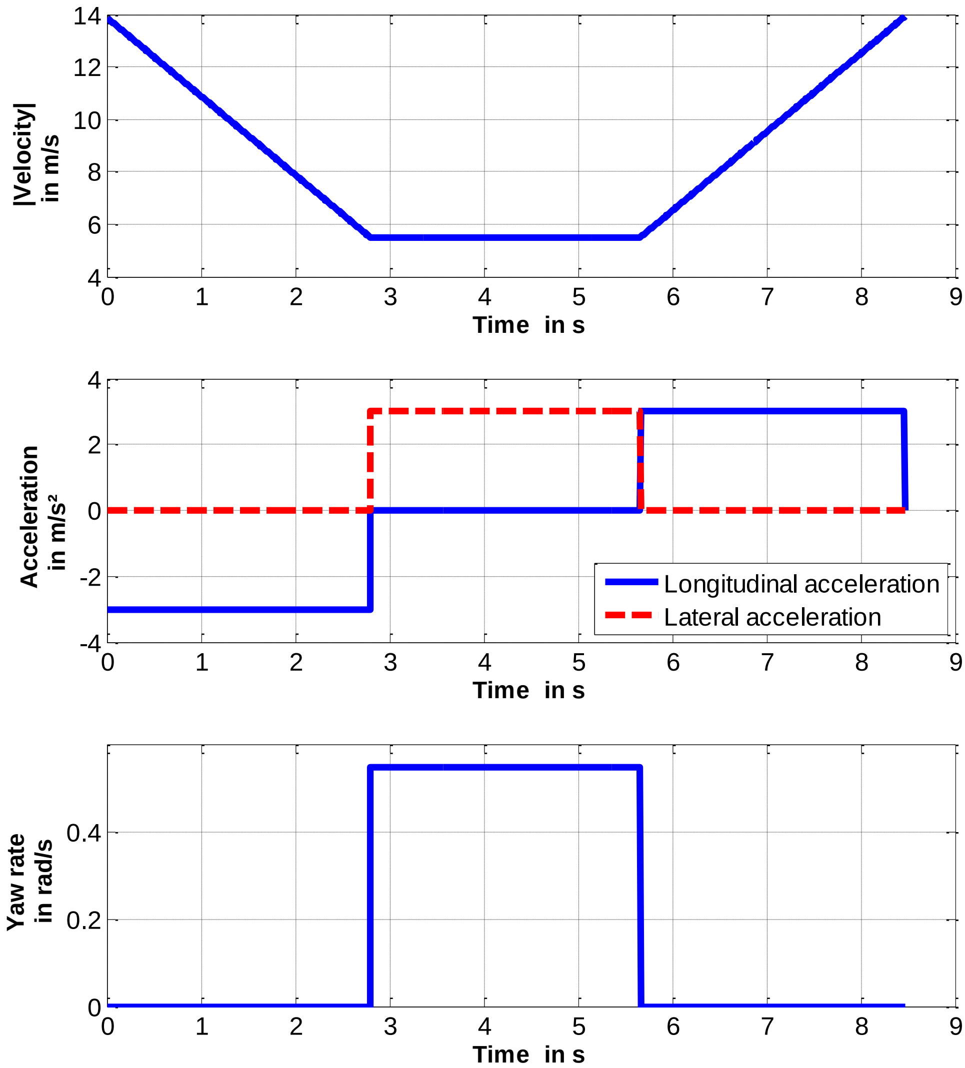

Figure 4.1: Reference signals of a passenger car for the T-junction maneuver (COS (V))

4.1.2 Single Test Maneuver – 8-Track

The horizontal 8-track is not a use case for DS studies; rather, it is used for evaluating the motion control and the control architecture of the wheeled motion base. The information presented in this section was published in Betz et al.[201]. This maneuver is conducted at constant velocity. Lateral dynamics and the transient change from cornering from left side to right side are contained. The boundary conditions of this maneuver are chosen to operate the tires in their non-linear, friction-slip range. Table 4.1 summarizes

[201] Betz et al.: Driving dynamics control of WMDS, 2013.

the determined conditions of the test maneuver as well as the iteratively derived parameterization of the control setup. Because this maneuver is conducted to examine the behavior of the controlled system, no MCA is applied. The DS itself performs the 8-track without washout or tilt coordination. Contrary to the T-junction maneuver, here the reference signals are not derived by calculations but by an *IPG CarMaker* simulation (section 4.2). Therefore, the reference signals show typical vehicle behavior such as side slip and transient cornering onset (Figure 4.2).

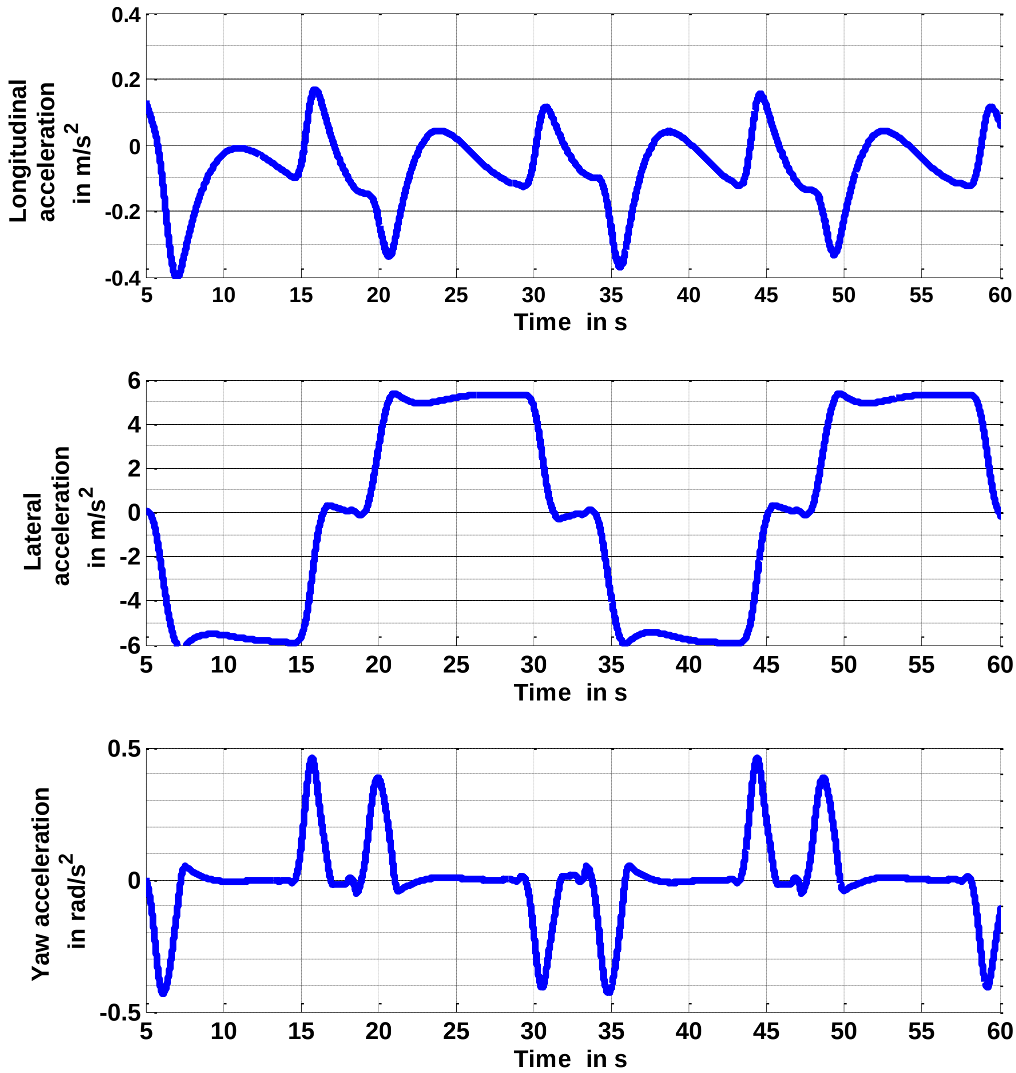

Figure 4.2: Reference signals of the 8-track maneuver[202]

[202] The x axis starts at $t = 5$ s because the target vehicle velocity must be reached before the described maneuver can be conducted.

Table 4.1: Properties and control gains of the 8-track maneuver

Property	Unit	Value
Corner radius	m	25
Constant velocity	m/s	12.2
Maximum lateral acceleration	m/s²	±6
KP_a control gain	1	0
$KP_{\ddot{\psi}}$ control gain	1	0
KI_a control gain	1/s	5
$KI_{\ddot{\psi}}$ control gain	1/s	5

4.1.3 Representative Urban Traffic Circuit

The urban traffic circuit is used to identify DS motion requirements caused in urban traffic by normal drivers. Thus, the MCA is applied and its parameterization complies with section 3.2. The information presented in this section is based on Graupner[203] and was published in Betz et al.[204].

All test drives are done during the day but off-hour. Each test drive is performed by a different driver. The driver base is not representative of the general public. All drivers are familiar with the urban traffic circuit, resulting in higher vehicle dynamics compared to normal driving behavior. Hence, the gained performance demands are assumed to be an over-estimation covering at least the performance demands of normal driver behavior. The test drives are performed in a VW Golf VI R (equipped car with 2 passengers has 1780 kg mass; 199 kW; all-wheel drive) which is equipped with a *GeneSys ADMA G*[205] measurement unit, logging translational accelerations and rotational rates at a rate of 100 Hz.

The urban traffic circuit is based on an analysis of 130 randomly chosen traffic situations situated in Darmstadt, Germany. The analysis determines the relative frequency of traffic situation categories: crossroads, T-crossroads, bends, lane splitting, and merge. The characteristic properties of these categories are analyzed: lane width, number of lanes, speed limit, curvature, distance of road splitting/merging, and priority signs. The most representative ones are assembled to make up the Darmstadt urban traffic circuit, taking relative frequency into account. In total, 25 representative traffic situations are selected and fitted into a road map. The connection of the relevant situations is determined by *Google Maps* and is slightly adapted in order to improve practicability. The

[203] cf. Graupner: Urban traffic circuit, Bachelor’s thesis supervised by Betz, 2011.

[204] Betz et al.: Motion analysis of WMDS, 2012.

[205] Genesis – virtual: ADMA G, http://www.genesys-adma.de/, last access: May 26th 2014.

urban traffic circuit is 21 km long and takes about one hour to complete. In total, four urban test drives are analyzed. Further details concerning the selected situations and the precise course of the road are shown in appendix G.1.

The relevant vehicle motions ($a_{x,\mathrm{V}}$, $a_{y,\mathrm{V}}$, and $\dot{\psi}_{\mathrm{V}}$) are presented as cumulative distribution function (CDF) in Figure 4.3. The four subjects do not cause serious differences in the vehicle signals considered. As discussed, the presented collectives are expected to contain at minimum the components of normal driver behavior.

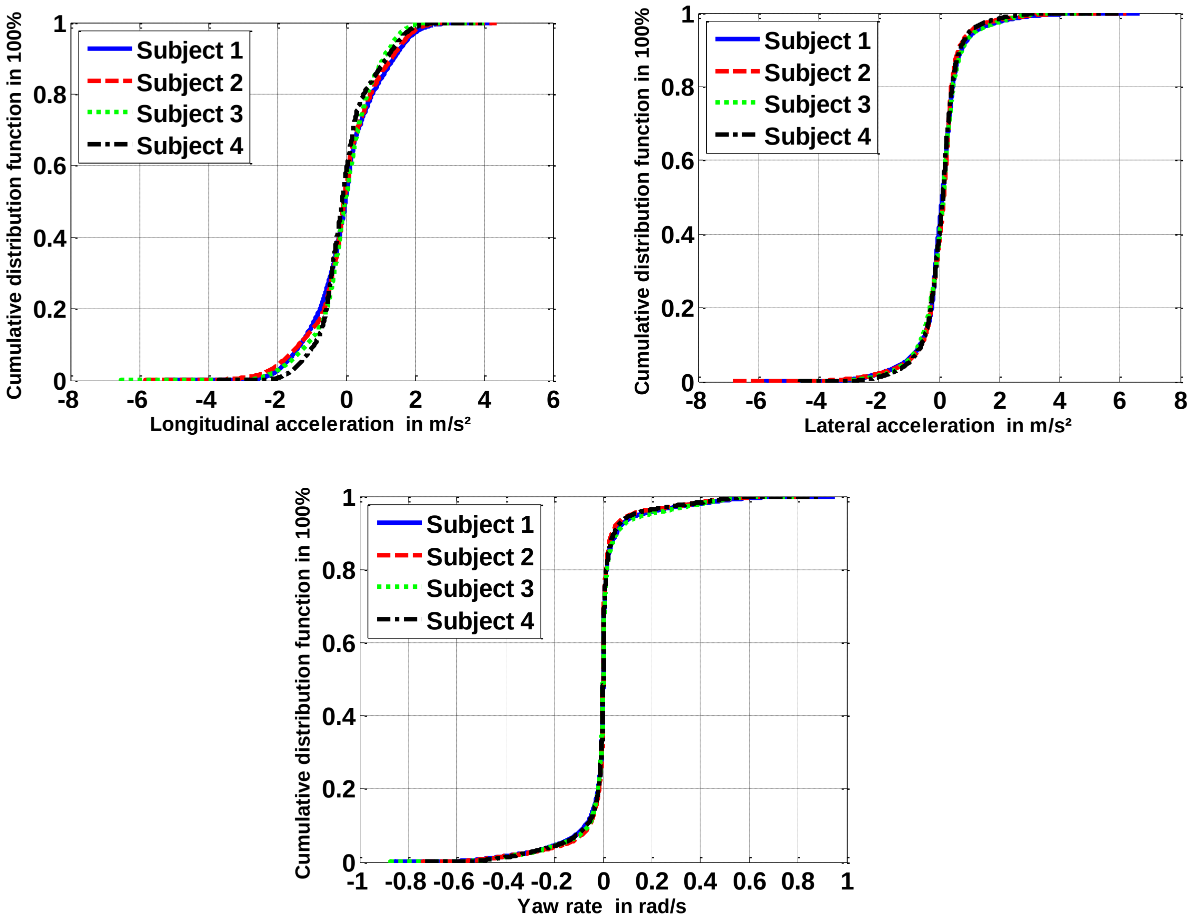

Figure 4.3: CDF plots of relevant vehicle motions – urban circuit[206]

4.1.4 Emergency Stop

The validation of the safety architecture is done experimentally by test drives utilizing the hardware structure. The WMDS is accelerated to an initial velocity of about 3 m/s. The emergency stop is activated while the WMDS is coasting freely on a straight asphalt concrete test track at the test facility close to Darmstadt, Germany (August-Euler-

[206] Not presented in Betz (Betz et al.: Motion analysis of WMDS, 2012).

Flugplatz, Griesheim). Further details concerning the asphalt concrete pavement are found in Seipel[207]. The activation is realized by a wireless emergency stop system[208] that cuts the energy supply from the electromagnetic clamps in order to release the actuation force of the preloaded springs. For validation of the general idea of the safety architecture, only the minimum number of three lifting systems[209] is utilized as this test case creates the maximum mechanical stress for the safety system in terms of horizontal and vertical forces.

The acceleration signals that are logged by a GeneSys ADMA G[210] measurement unit are evaluated in terms of maximum and mean deceleration. The measurement is supported by a Correvit sensor[211] that measures the absolute velocity. The measurements are done at a sampling rate of 250 Hz. The increased sampling rate compared to the conducted urban test drives (100 Hz) is enabled by reducing the number of logged signals.

4.2 DS Dynamics Model

The goal of the driving dynamics analysis is the numerical validation of the motion control system (section 3.3) and the control architecture (section 3.4). Thus, the numerical validation is conducted on the basis of the 8-track maneuver with disabled MCA (no tilt coordination and no washout as described in section 4.1.2). The driving dynamics behavior of the WMDS is simulated using IPG CarMaker[212]. CarMaker provides a parameter-based, multi-body vehicle model and is linked to MathWorks Matlab/Simulink[213] by a control interface. The first-order Euler method is used with a fixed step size of 1 ms. This simulation parameter is required by CarMaker. Because CarMaker is mainly used for analysis of passenger cars, some workarounds have to be implemented to build a three-wheeled motion base with unlimited steer angles as re-

207 Seipel: Tire marks, 2013.

208 SR-TEC – virtual: FS 600, http://www.sr-tec.de/, last access: May 28th 2014.

209 The overall safety architecture is designed to provide six lifting systems in total for the sake of redundancy as presented in section 3.5.6.

210 Genesis – virtual: ADMA G, http://www.genesys-adma.de/, last access: May 26th 2014.

211 Datron – virtual: Correvit S-400, http://www.corrsys-datron.com/, last access: May 28th 2014.

212 IPG – virtual: CarMaker software, http://ipg.de/de/simulationsolutions/carmaker/, last access: May 26th 2014.

213 MathWorks – virtual: Matlab/Simulink softwarehttp://www.mathworks.de/products/simulink/, last access: May 26th 2014.

quired to represent the introduced WMDS. One wheel is suppressed by minimizing its size and placing it above ground without ground contact. The information presented in this section was published in Betz et al.[214]

4.2.1 Tire

Conventional tires of passenger cars are used for the multi-body analysis because no suitable tire model for the applied group of press-on band tires was found in the literature. The dynamics of the class of press-on band tires is hardly researched because conventional applications such as forklift trucks are not designed and optimized towards advanced vehicle handling. The numerical simulation of press-on band tires will be of interest in future research of the WMDS in order to gain insights into the behavior of the controlled system and the computational tuning of the control architecture.

The simulation of the tire behavior is based on Pacejka's Magic Formula[215] (version 5.2). The tire data is provided as ADAMS tir-file of a conventional 195/65R15 tire.[216] The tire dimension is adjusted in order to fit the geometry of the WMDS. The relevant excerpt of the tire properties is presented in Table 4.2.

Table 4.2: Excerpt of relevant properties of the pneumatic tire[217]

Property	**Unit**	**Value**
Wheel radius	m	0.15
Cornering stiffness	kN/rad	67
Nominal wheel load	kN	4
Vertical stiffness	kN/m	200
Vertical damping	Ns/m	50

4.2.2 Geometric Specifications

The WMDS is designed as an equilateral triangle with point masses in the center of the platform and in each wheel center. The relevant specifications are listed in Table 4.3. The specifications differ from the final WMDS prototype design (section 3.5.5, Table 3.8) because the multi-body analysis bases on a preceding investigation. Due to the

[214] Betz et al.: Driving dynamics control of WMDS, 2013.

[215] Pacejka: Tire and Vehicle Dynamics, 2012.

[216] MSC Software Corporation: MD ADAMS 2011, tire file "pac2002_195_65R15.tir", 2011.

[217] Betz et al.: Driving dynamics control of WMDS, 2013.

negligible changes, the conclusions reached are expected to remain unchanged; hence, the multi-body analysis of Betz[217] is not updated.

Table 4.3: Geometric specifications of the multi-body model of the WMDS[217]

Property	Unit	Value
Edge length of equilateral triangle	m	2.54
Height of CG	m	0.48
Total mass	kg	1,200
Total inertia torque about z-axis	kgm²	945
Inertia torque about z-axis of steer units	kgm²	1.09

4.2.3 Chassis Geometry

The chassis geometry differs from that of conventional passenger cars. The WMDS has only three wheels. They are designed to be fully steerable (infinite rotation about the vertical axis). The chassis properties like camber, toe, kingpin inclination, and offset are designed to be zero in order to meet the final WMDS design. These properties do not vary with wheel lift. While most of the characteristic chassis design of the WMDS is well represented in the multi-body model, one design mismatch must be tolerated. The body spring and damper cannot be dropped off the multi-body model due to numerical issues of the applied software tool. Therefore, the stiffness of the body spring is 25 kN/m and the constant of the body damper is 2.5 kNs/m (compression and rebound). Future research will be required to solve this problem in order to gain further insights into the controlled system of the WMDS by enhancing the comparability of hardware prototype and the numerical multi-body simulation.

4.2.4 Motor Model

The traction and steer motors are implemented according to Scholz[218] using differential equations of the electric circuit. The maximum torque output of the traction and steer units is limited to 1200 Nm. Maximum rotational speed of the motors does not need to be limited because the operational field of the motors stays below the magnetic field weakening. The part beyond the field weakening is not of interest, because the WMDS does not have a friction brake; thus, the motor torque must be sufficient to provide full acceleration and deceleration up to maximum operational velocity. The electrical machines are parameterized accordingly to Table 4.4.

[218] cf. Scholz: WMDS, Master's thesis supervised by Betz, 2013.

Table 4.4: Specifications of the model of the electric motors[219]

Property	Unit	Value
Stator resistance	mΩ	19
Inductance in q axis	mH	0.18
Torque constant	Nm/A	0.673
Maximum torque	Nm	1,200

[219] Betz et al.: Driving dynamics control of WMDS, 2013.

5 Results

5.1 Evaluation of T-Junction Maneuver

The T-junction maneuver mentioned previously is one vital test case of DS research in urban traffic areas. The maneuver leads to high DS requirements because it causes the acceleration vector to turn by about 90° yaw angle resulting in significant horizontal motion demand. The test case is evaluated using the system design presented in section 3.2 (Motion Cueing) and 3.3 (Motion Control). The applied scaling factor of the vehicle's acceleration task is 1, and the WMDS specifications of the WC mass assumption[220] (section 3.5.5, Table 3.8) are applied. Due to the short time span of the single test maneuver ($t = 8.5$ s), the results are presented as time plots. At the end of this subsection, a summary of the identified requirements is presented in Table 5.1. The table also provides results for the exemplarily increased dynamic of the treated maneuver (6 m/s² instead of the original 3 m/s²).

5.1.1 Velocity and Acceleration Demand

The trajectory of the DS for performing the aforementioned maneuver is shown in Figure 1.1 of section 1.1. The corresponding velocity and acceleration profiles of the DS are presented in Figure 5.1 and Figure 5.2. The acceleration demand reaches about 5.7 m/s² and is higher than the maximum acceleration amplitude occurring in the T-junction maneuver (see section 4.1.1: 3 m/s²) of the virtual vehicle. The maximum required velocity of the DS stays below 21 m/s. It becomes obvious that the DS task is not done after the last demanded acceleration of the virtual vehicle at $t = 8.5$ s. At this time, the vehicle's maneuver is finished but the DS is still in motion ($v(t = 8.5\text{ s}) = 21\text{ m/s}$). Thus, the washout algorithm makes allowance for the DS position and velocity by causing tilt in order to return to initial position. Because washout motion is based on tilt coordination, the occurring peak accelerations are limited to about 4 m/s² (section 2.2). The minor task causes fewer performance demands, as shown by Figure 5.1 and Table 5.1 (p. 105). Only the workspace demand keeps rising after the maneuver of the virtual vehicle is completed because of the velocity state of the DS.

[220] $m_{\text{total,WC}} = 2{,}272$ kg, $h_{\text{CG}} = 0.67$ m, $l_{\text{t}} = 3.22$ m, $\Theta_{zz,\text{DS}} = 1{,}648\text{ kgm}^2$, $\Theta_{zz,\text{steer}} = 2.94\text{ kgm}^2$.

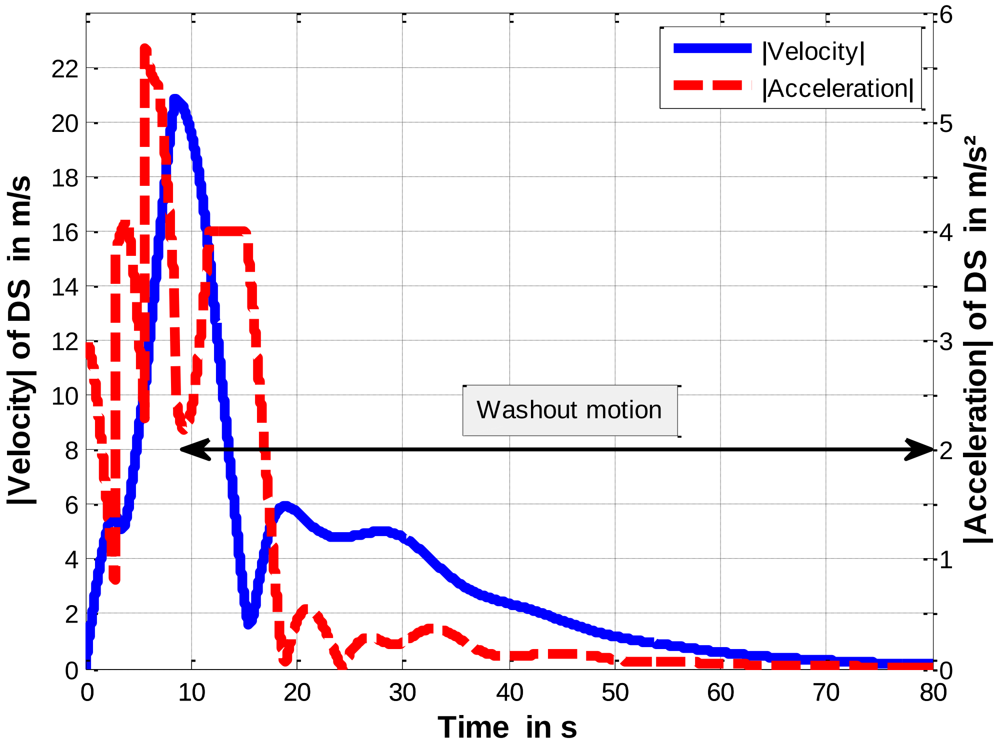

Figure 5.1: Velocity and acceleration of the DS (earth fixed COS) – T-junction + washout motion

The most demanding part of this maneuver occurs within the first 8.5 s; Figure 5.2 presents the absolute velocity and acceleration of the WMDS for this time span in more detail. This figure shows the divergent tasks of the DS and the virtual vehicle created by the MCA as well as the initial states of the two considered systems: The DS velocity increases as well in the acceleration as in the brake phase of the virtual car.

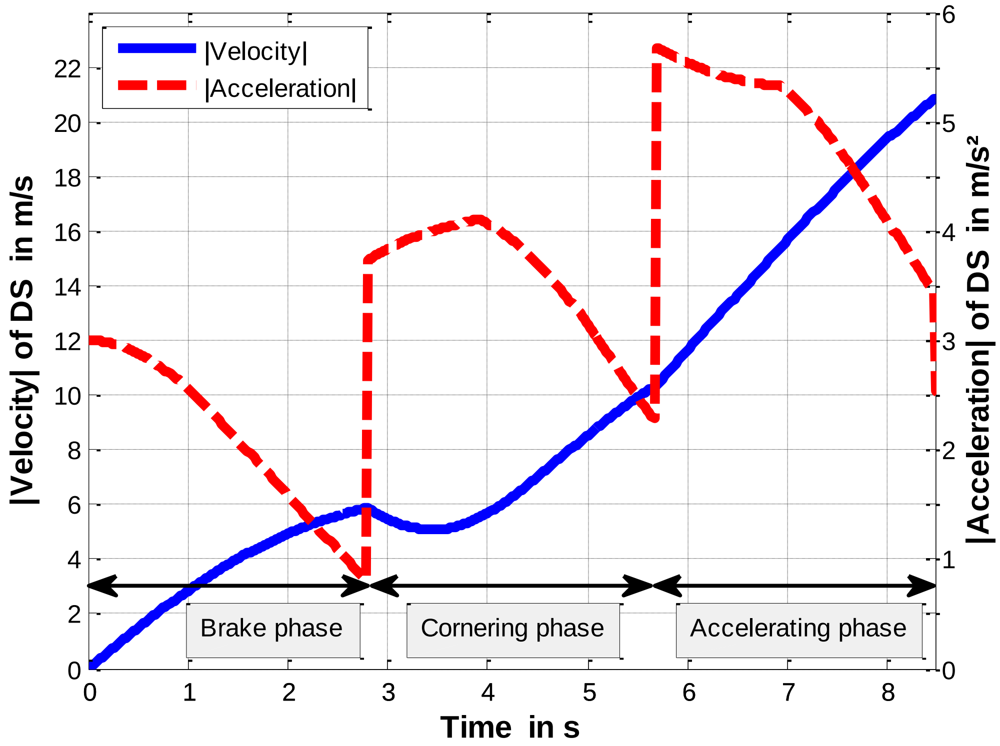

Figure 5.2: Excerpt of velocity and acceleration of the DS (earth fixed COS) – T-junction

In the following subsections, the focus of the figures is also aimed at the demanding part of the conducted T-junction maneuver.

5.1.2 Power Demand

In order to perform the trajectory of the DS, the drive unit must provide tire forces. These forces are generated by both the traction motors and the slip angles. The slip angles are controlled by the steer motors. The power demand of the traction motors reaches about 70 kW as presented in Figure 5.3. The wheels differ in their power demand due to wheel load change from geometric relations and the superposition of the translational and yaw task (section 3.3). The peaks at $t \approx 2.8$ s and $t \approx 5.7$ s are caused by a sudden rise of the artificial reference signal of the yaw acceleration. Hence, the exaggeration does not occur in real-world situations and is only inherited from the artificial nature of the reference signal.

The subsequent motion of the washout is not presented in the figure because it causes moderate power demand due to the limitation of acceleration by cabin tilt (section 2.2) as aforesaid.

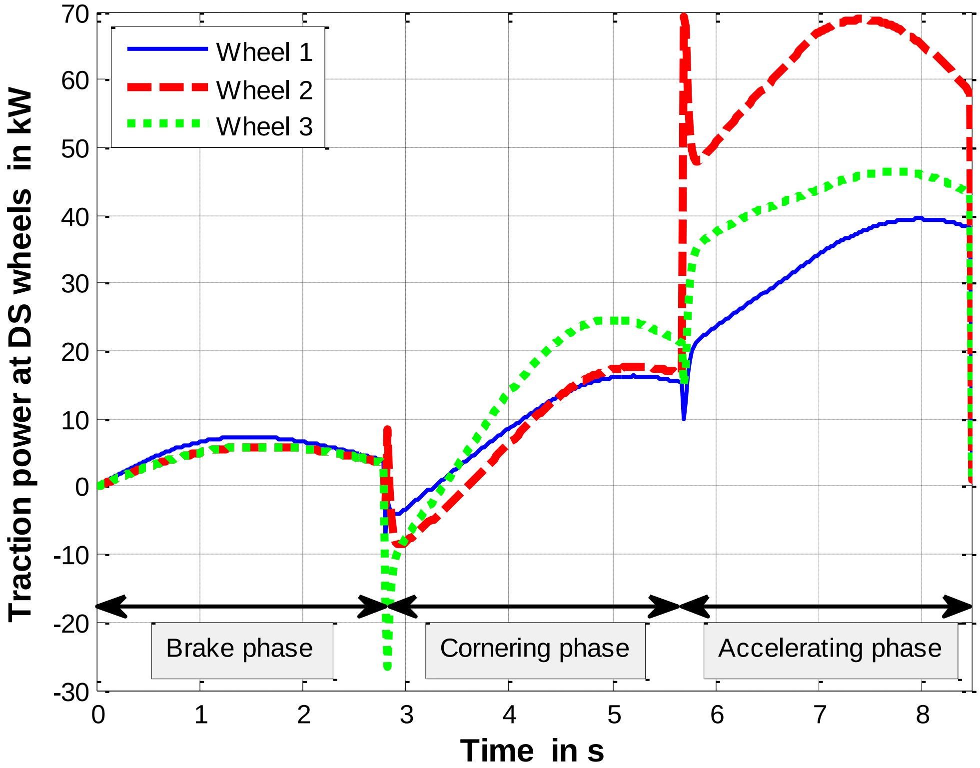

Figure 5.3: Power demand of traction motors – T-junction

In contrast to the traction task, the results of Figure 5.4 show a low steer power demand; it is less than 4 kW for the introduced T-junction maneuver. It seems that the steer task causes a significantly smaller power demand than the traction motor task. As previously mentioned, the peaks at $t \approx 2.8$ s and $t \approx 5.7$ s are caused by the artificial nature of the steep yaw acceleration rise. Besides the two peaks, the power demand of the steer task is negligible. Therefore, the average power demand is negligible. It should be emphasized that the onset of acceleration in this example is in the x-direction of the WMDS as the wheels are oriented in initial condition. If the wheels were oriented perpendicular to the onset direction, the worst case of a 90° steer step would occur as discussed in the urban circuit evaluation of the following subsection 5.2. In any case, according to the results, the average power demand of the steer task is assumed to be moderate compared to the traction task. It should be stressed that although the selected wheels have no designed caster, there might be disturbances in the steer task caused by horizontal forces and dynamic caster originating from deformation of the contact patch of the tire. This topic requires further research in future works.

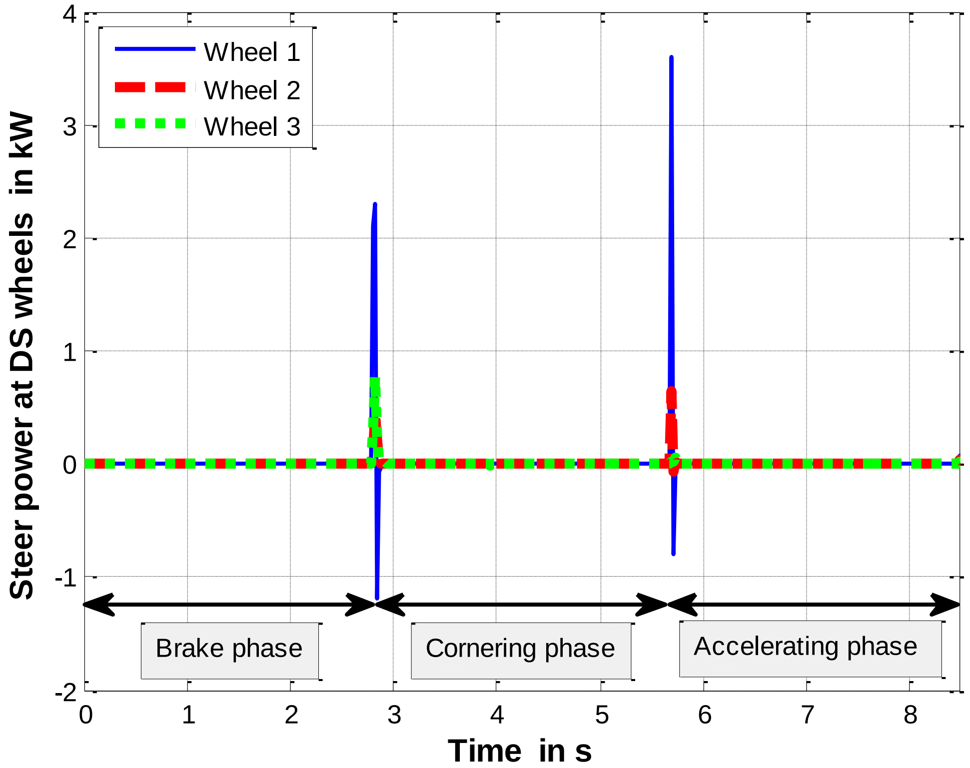

Figure 5.4: Power demand of the steer motors – T-junction

5.1.3 Friction Coefficient Demand

The friction coefficient demand reaches a peak value of 1, according to Figure 5.5. Recalling the suddenly occurring yaw task of the artificial reference signal allows the conclusion that the peak value of a real-world T-junction maneuver would be lower. The directly following friction plateau (in Figure 5.5; see vertical auxiliary line) of about 0.57 gives a good estimation of the expected peak value of the real-world application. Differences in the friction coefficient demand between the wheels occur only if yaw acceleration is applied (at 2.8 s and 5.7 s). The other parts of the test case show equal friction coefficient demand of the wheels as intended by the motion control (section 3.3).

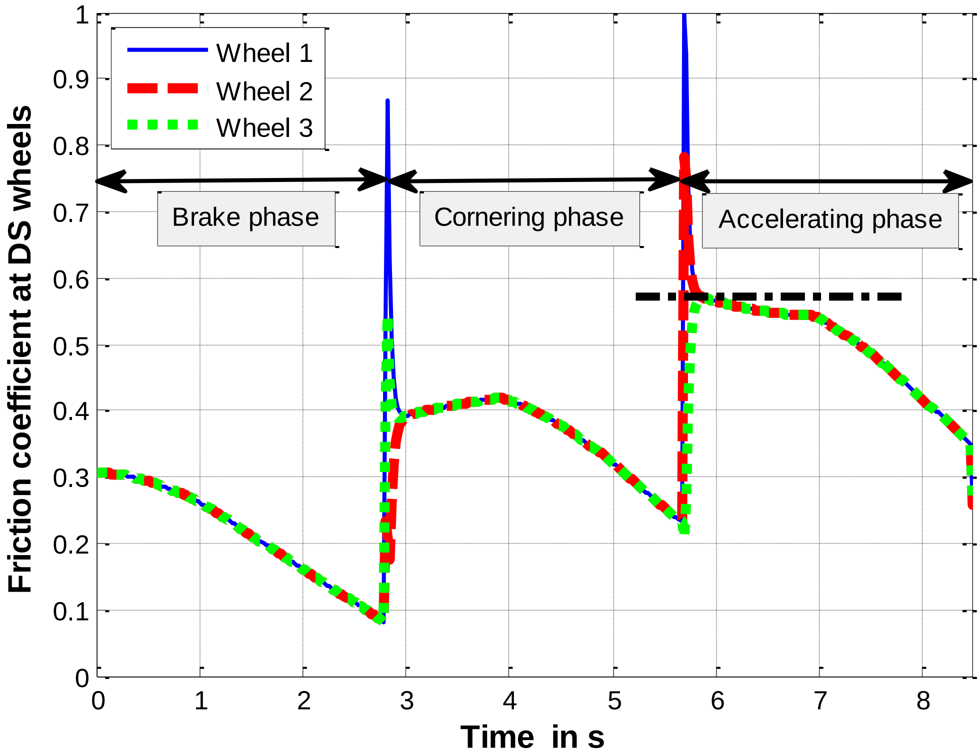

Figure 5.5: Friction coefficient demand at the wheels of the WMDS – T-junction

5.1.4 Summary of the T-Junction Evaluation

The requirements determined for the introduced T-junction maneuver are summarized in Table 5.1. The average power demand of the traction motors strongly depends on the DS task as substantiated by the results including the washout motion to initial position. Including the moderate washout motion decreases the average power demand by more than one magnitude. The steer task does not influence the energy demand of the overall system noticeably. While most DS requirements are not influenced by the washout motion, the displacement shows significant increase. Thus, the returning to initial position boosts the required workspace demand.

Most of the falsification aspects rise when the acceleration amplitudes of the test maneuver are increased from 3 m/s² to 6 m/s²[221] as presented in Table 5.1. The acceleration demand reaches 7.4 m/s² and again is larger than the reference signal. However, the maximum displacement and the maximum occurring velocity are reduced significantly. The unexpected reduction is the result of the changed time span of the reference signals and the superposition with the unchanged constraints of the tilt coordination. Further details concerning the influence of mass and acceleration scaling are discussed with

[221] Maximum acceleration amplitude of normal drivers according to conducted test drives (section 4.1.3)

respect to the urban traffic circuit in the following subsection (5.2) as it provides a broader view of this topic owing to the more complex test maneuver.

Table 5.1: Requirements of falsification aspects – T-junction

		Value $\boldsymbol{a = \pm 3\ \mathrm{m/s^2}}$ Scaling factor 1		**Value** $\boldsymbol{a = \pm 6\ \mathrm{m/s^2}}$ Scaling factor 1	
Falsification aspects	**Unit**	T-junction only *t*=[0, 8.5 s]	+ Washout to initial position *t*=[0, 80 s]	T-junction only *t*=[0, 8.5 s]	+ Washout to initial position *t*=[0, 80 s]
d_{max}	m	61.2	139.2	37.7	100.9
v_{max}	m/s	20.8	20.8	18.4	18.4
a_{max}	m/s²	5.7	5.7	7.4	7.4
$P_{\mathrm{traction},i,\mathrm{max}}$	kW	69.3	69.3	116.5	116.5
$P_{\mathrm{steer},i,\mathrm{max}}$	kW	3.6	3.6	6.4	6.4
$P_{\mathrm{traction,avg}}$	kW	75.3	6.0	125.3	4.4
$P_{\mathrm{steer,avg}}$	kW	0.0	0.0	0.0	0.0
μ_{plateau}	1	0.57	0.57	0.75	0.75

5.2 Evaluation of Urban Traffic Circuit

The urban test drives conducted provide test cases of normal drivers in urban traffic areas. The urban traffic circuit promotes high DS requirements because the course of road is not optimized for DS studies and lasts for about 1 h. The test drives are evaluated using the system design presented in section 3.2 (Motion Cueing) and 3.3 (Motion Control). For the presented figures a scaling factor of 1 and the WMDS specifications of the WC mass assumption[222] are applied. Owing to the long time span of the test drives, time plots are avoided. Instead, the results are presented as CDF plots. The data basis of the CDF plots contains all four test drives. At the end of each subsection, the results of the CDF plots are summarized in a table. In addition to a summary, the tables contain further results such as the influence of the DS setup (WC and BC: section 3.5.5, Table 3.8) and the exemplarily chosen scaling factors (1, 0.7, and 0.5) of the acceleration simulation.

[222] Table 3.8: $m_{\mathrm{total,WC}} = 2{,}272$ kg, $h_{\mathrm{CG}} = 0.67$ m, $l_{\mathrm{t}} = 3.22$ m, $\Theta_{zz,\mathrm{DS}} = 1{,}648\ \mathrm{kgm^2}$, $\Theta_{zz,\mathrm{steer}} = 2.94\ \mathrm{kgm^2}$.

5.2.1 Workspace Demand

The workspace demand (Figure 5.6) of the exemplary long lasting test drive shows roughly 300 x 210 m². Figure 5.6 suggests that higher displacements are rare compared to smaller ones. The assumption is confirmed by the probability of presence illustrated by the exemplarily chosen circles (80 %. 90 % and 95 % quantile). While the maximum displacement is about 210 m, only 20 % of the trajectory has a displacement of more than 41 m. The illustrated circles underline the tendency of a circular workspace, but small shares of the trajectory violate the described behavior and cause a significant increase of workspace demand.

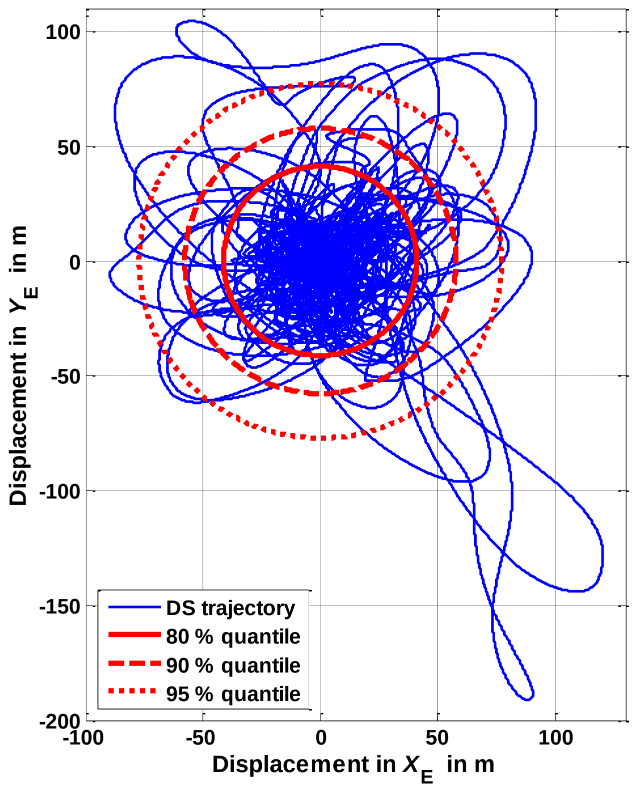

Figure 5.6: XY-plot of an exemplary test drive – urban circuit

The trajectory results from the mandatory acceleration profiles of the virtual vehicle and the MCA. Hence, the trajectory is not subject to the systems mass or geometry as shown in Table 5.2. The WC and BC setup does not affect the trajectory of the DS. However, the scaling factors affect the underlying acceleration profile. Thus, the trajectory is influenced. Table 5.2 encourages the use of scaling factors for reducing the workspace demand significantly. A precise relationship between the scaling factors and the displacement is not found due to the superposition of the acceleration of the virtual vehicle with the tilt coordination and the washout.

A comparison of the characteristic values from Table 5.2 in the form of a log-log plot yields almost linear slope as substantiated by the regression lines in Figure 5.7. Therefore, the found correlation has the characteristics of a power function. In this case, it is almost a quadratic correlation (range: 2 - 2.39).

Table 5.2: Displacement and the influence of scaling – urban circuit

			Scaling Factor		
			1	**0.7**	**0.5**
Displacement in m	Mean	WC/BC	18.37	8.88	4.91
	Q90	WC/BC	50.67	25.31	13.62
	Max	WC/BC	269.82	116.92	51.40

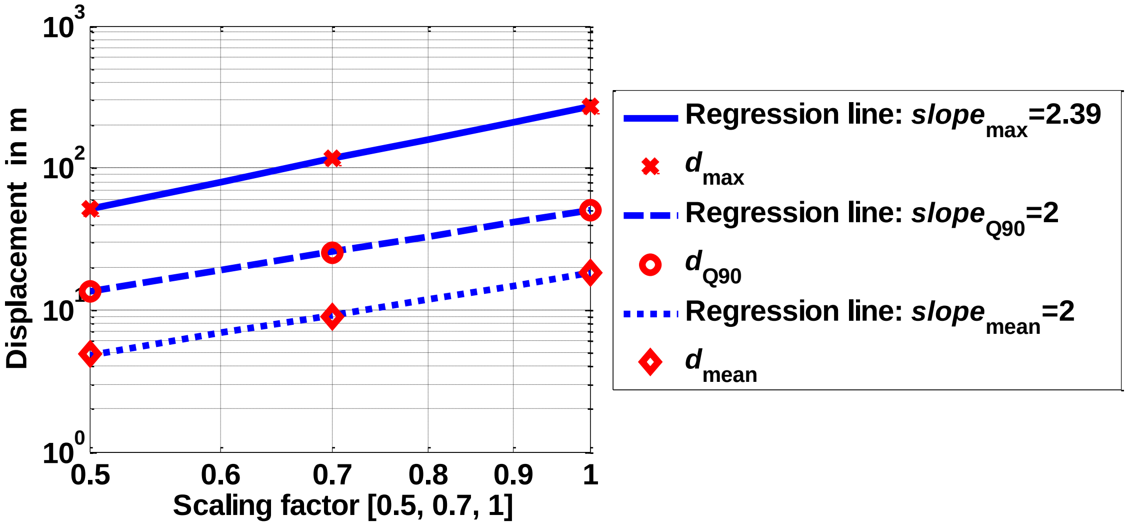

Figure 5.7: Regression lines for displacement and scaling factor – urban circuit

5.2.2 Velocity and Acceleration Demand

The corresponding velocity and acceleration demand of the DS trajectory is presented in Figure 5.8. The maximum velocity is 25 m/s while 90 % stay below 7.5 m/s. The maximum occurring acceleration is about 7.1 m/s². It must be stressed that only 1 % of the acceleration demand exceeds the expected range of the linear tire characteristic[223].

[223] General assumption of linear tire characteristics of pneumatic tires up to 4 m/s² – cf. Schramm et al.: linear single-track model, p. 244, 2010.

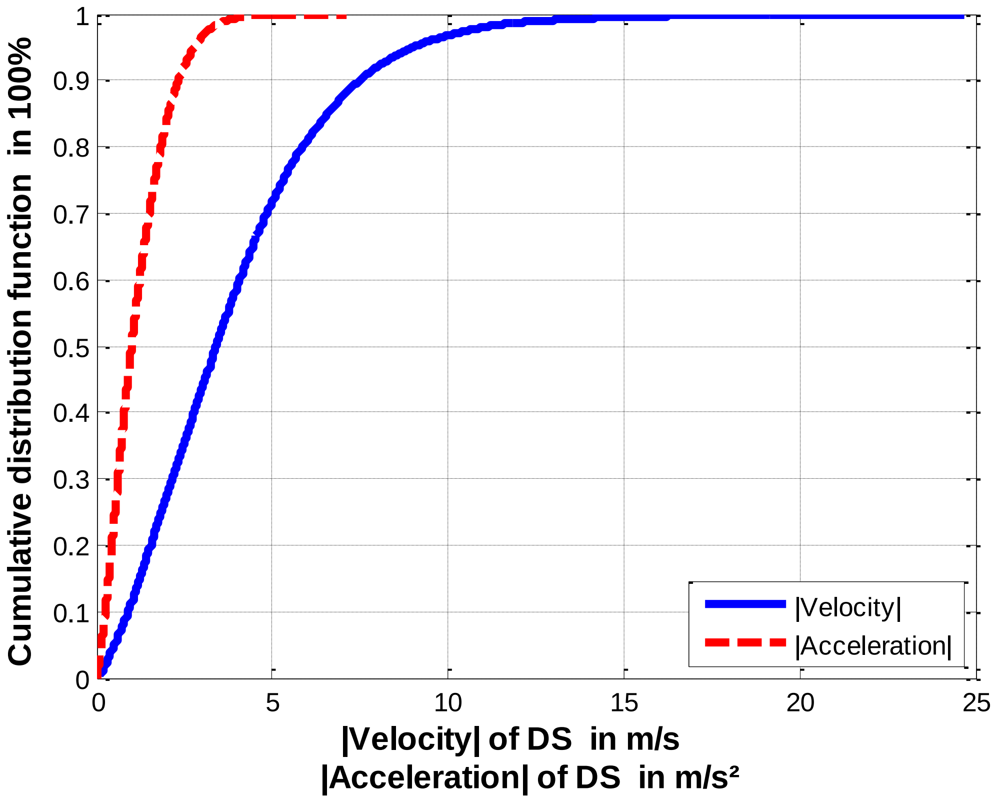

Figure 5.8: CDF plot of velocity and acceleration of the WMDS – urban circuit

As described, the trajectory is not influenced by the mass or geometry of the system. The same applies for the acceleration and velocity demand of the DS. Again, the influence of the scaling factors is significant but cannot be derived precisely because of the superposition of the acceleration of the virtual vehicle with the tilt coordination and the washout. In accordance with Table 5.3, the log-log plot in Figure 5.9 and Figure 5.10 yields almost linear slope for the characteristic values of acceleration and velocity (range for acceleration: 1.19 - 1.46; range for velocity: 1.82 - 1.96).

Table 5.3: Influence of scaling and mass onto velocity and acceleration demand – urban circuit

			Scaling factor		
			1	**0.7**	**0.5**
Velocity in m/s	Mean	WC/BC	3.41	1.71	0.88
	Q90	WC/BC	7.52	3.92	2.13
	Max	WC/BC	24.67	12.00	6.75
Acceleration in m/s²	Mean	WC/BC	1.00	0.59	0.36
	Q90	WC/BC	2.34	1.53	1.01
	Max	WC/BC	7.14	4.91	3.13

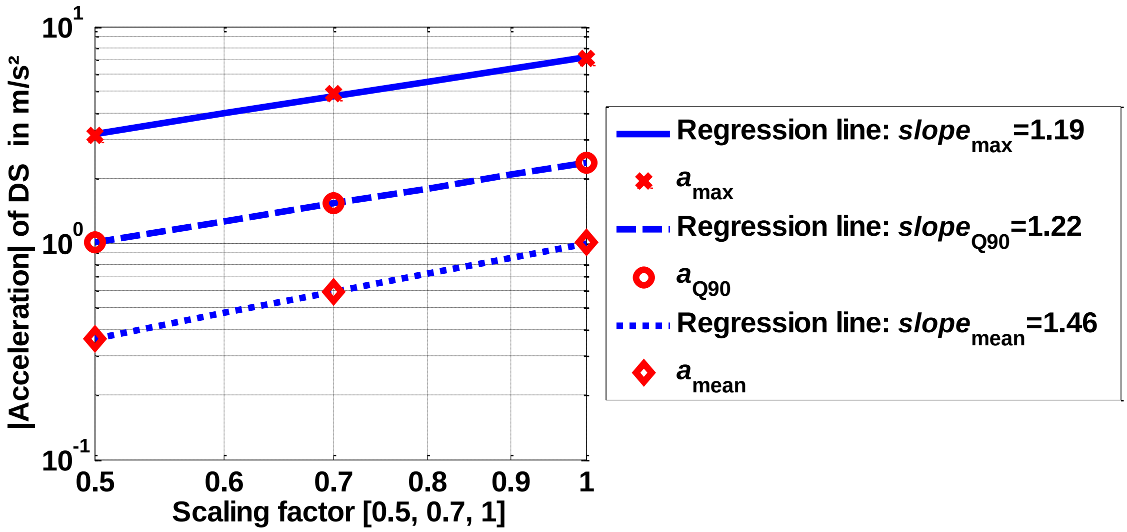

Figure 5.9: Regression lines for acceleration and scaling factor – urban circuit

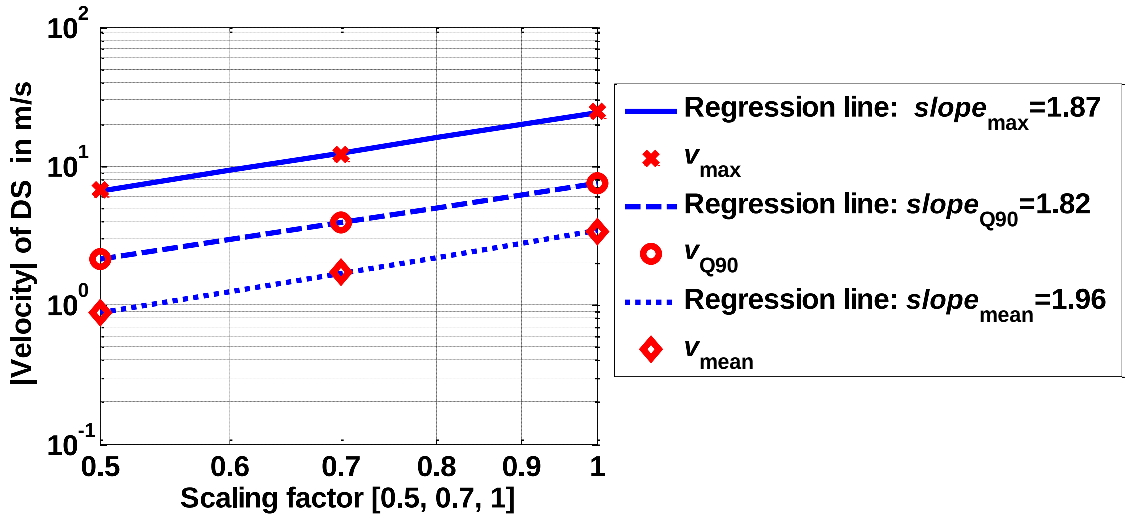

Figure 5.10: Regression lines for velocity and scaling factor – urban circuit

5.2.3 Power and Energy Demand

The power demand of the traction and steer motors differs significantly as shown in Figure 5.11. The results also show that the individual drive units do not differ in power demand; this is true for both the traction motors and the steer motors. The minimum and maximum median of the three steer units differ by about 5%; for the traction units it is about 3%. The peak power demand of the traction motors reaches about 94 kW. The steer motors cause higher peak demands, reaching about 900 kW at each motor. While the peak power demand of the steer motors is about one magnitude higher compared to the demand of the traction motors, the largest share (98.5 %) of the occurring steer power is smaller by more than two orders of magnitude. Only 0.01% of the steer task requires more power than the traction task. Hence, the average power demand, yielding the energy demand, mainly results from the traction motors as confirmed by Figure 5.11 and Table 5.4. Although the drill moment and the friction of the steer unit are disregarded, it becomes obvious that the peak performance requires a system dimensioning that is greatly inflated for the largest share of the steer task. The rare occurrence of high power demands is confirmed by the average power demand of only 2.12 kW for the whole drive unit. According to Table 5.4 the largest average power demand of 2.12 kW is caused by the WC setup without acceleration scaling. Use of state-of-the-art traction batteries of electric vehicles (cf. section 2.7) allows operation of the wheeled mobile platform for several hours by on-board energy supply. Even the traction battery of the prototype has enough capacity to provide an operation time span of about 2.5 h.

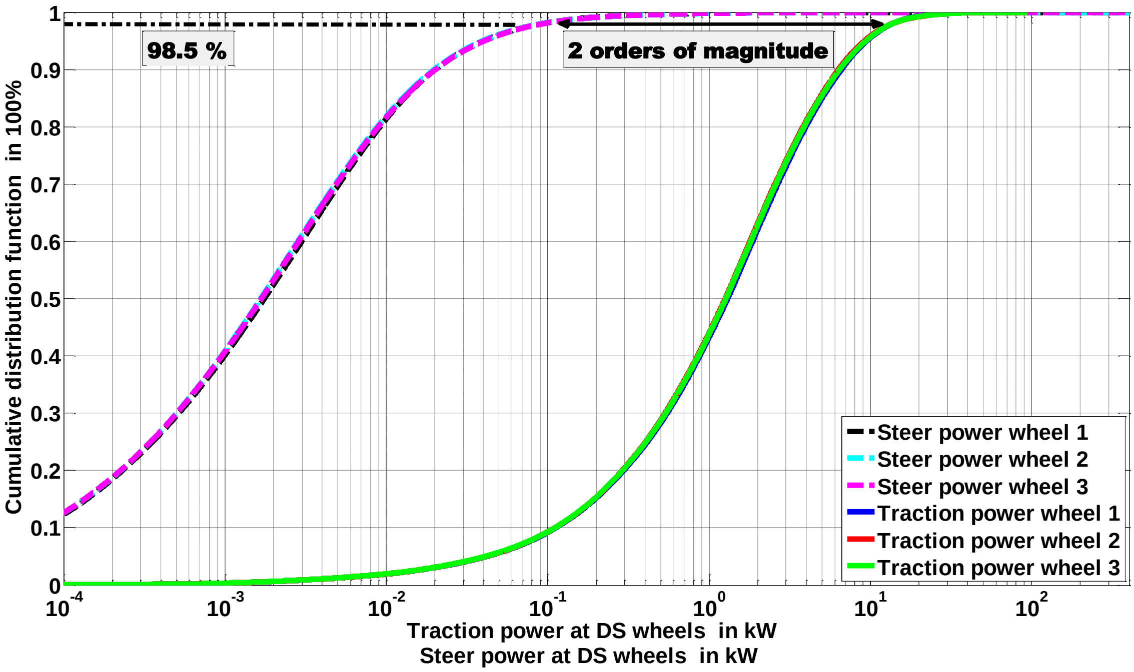

Figure 5.11: Semi-logarithmic CDF plot of the traction and steer power demand – urban circuit

The peak power demand of about 900 kW of the steer task is not unexpected as shown by equation (65) and the following description. Further analysis of the results shows that maximum values of the steer power occur only when wheel velocities are close to 0. This condition turns out to be necessary but not sufficient for causing an extreme task for the steer motor. The reason for this is that absence of horizontal velocity does not allow for providing acceleration due to changing the direction of motion. Hence, the absence of velocity requires fully reorienting the conventional wheel to face in the direction of the prescribed acceleration, in order to accelerate the wheel in that direction. Thus, an extreme steer task occurs when the wheel velocity is low and the demanded wheel force vector has a component perpendicular to the wheel orientation. The worst case occurs if the wheel must be reoriented by 90° in order to perform the requisite acceleration of the WMDS. Steer angle steps of more than 90° are not necessary because the direction of rotation can be chosen freely in standstill. Concluding, it should be stressed that the maximum steer power demand is caused by a 90° steer step considering the moment of inertia of the steer unit and the assumed response time. Hence, the step size of 20 ms must be considered when interpreting the peak power demand that is derived by the numerical simulation. According to equation (65) the power demand is inversely proportional by the power of three to the tolerated response time. Therefore the dimensioning of the steer motors strongly depends on the tolerated response time of the subject and needs further research in future works.

$$P_{\text{steer},i,\max} = \ddot{\delta}_i \theta_{zz,\text{steer}} \dot{\delta}_i \approx \frac{\pi/2}{(0.02\ \text{s})^2} \cdot 2.94\ \text{kgm}^2 \cdot \frac{\pi/2}{0.02\ \text{s}} = 907\ \text{kW} \qquad (65)$$

The mass and system geometry affect some of the observed falsification aspects presented in Table 5.4 (compare: WC and BC setup). Recalling the considered mass of the WC and BC assumption, a mass ratio of 1.27 is evident ($2272\ \text{kg}/1786\ \text{kg}$). It should be stressed that the mass increase is assumed to be accompanied by linear adaptation of the geometry of the DS (the height of CG and the edge length of the DS's foot print). Hence, the behavior of the wheel load change stays untouched.

Comparing the ratio of the traction power demands of the WC and BC setup shows linear dependence between the mass and the geometry increase.[224] The average traction power demand is also affected by the WC and BC setup. The dependence is close to the previously observed linear relation.[225]

The only influence of the WC and BC setup on the steer power is found for the maximum value. The other characteristic values of the steer unit are below 0.1 kW and therefore not of interest. The reason for the dependence of the maximum steer power results from the assumed linear increase of the moment of inertia of the steer unit.[226] Further potential influence of the mass and geometry setup on power demand of the steer unit is expected from wheel load increase because this causes rise of drill moment at low velocities.

Beside the influence of the WC and BC setup, the effect of the acceleration scaling is observed. The power demand of the traction motors yields the dependence of a power

---

224 $\frac{P_{\text{drive,mean,WC}}}{P_{\text{drive,mean,BC}}} = \frac{P_{\text{drive,Q90,WC}}}{P_{\text{drive,Q90,BC}}} = \frac{P_{\text{drive,max,WC}}}{P_{\text{drive,max,BC}}} \approx 1.27;$ for $scaling\ factor\ \in [1, 0.7, 0.5]$.

225 $\frac{P_{\text{avg,drive,WC}}}{P_{\text{avg,drive,BC}}} \approx 1.31;$ for $scaling\ factor\ \in [1, 0.7, 0.5]$.

226 Ratio of moment of inertia: $\theta_{zz,\text{steer,WC}} = \theta_{zz,\text{steer,BC}} \cdot 1.17 \quad \left(\frac{factor_{\text{WC}}}{factor_{\text{BC}}} = \frac{1.4}{1.2} = 1.17\right)$ $\rightarrow \frac{P_{\text{steer,max,WC}}}{P_{\text{steer,max,BC}}} \approx 1.17;$ for $scaling\ factor\ \in [1, 0.7, 0.5]$.

function on the exemplarily chosen scaling factors as presented in Figure 5.12. The log-log plot shows almost linear slope as confirmed by the regression lines. Hence, the slope of the regression lines gives an indication of the power (range: 3.1 - 3.48). As expected, these values correlate well with the sum of the slopes of the regression lines for acceleration and velocity shown in Figure 5.9 and Figure 5.10.

Table 5.4: Influence of scaling and mass on power and energy demand – urban circuit

Falsification aspects			Scaling factor					
			1		0.7		0.5	
Traction power in kW	Mean	WC	1.28		0.38		0.13	
		BC		1.00		0.30		0.10
	Q90	WC	6.46		2.10		0.75	
		BC		5.08		1.65		0.59
	Max	WC	93.84		27.36		8.78	
		BC		74.07		21.72		6.63
Steer power in kW	Mean	WC	<0.01		<0.01		<0.01	
		BC		<0.01		<0.01		<0.01
	Q90	WC	0.02		0.02		0.03	
		BC		0.01		0.02		0.02
	Max	WC	897.91		903.19		910.53	
		BC		770.65		775.47		775.55
Average traction power in kW		WC	2.08		0.60		0.21	
		BC		1.56		0.46		0.16
Average steer power in kW		WC	0.03		0.06		0.10	
		BC		0.02		0.05		0.09

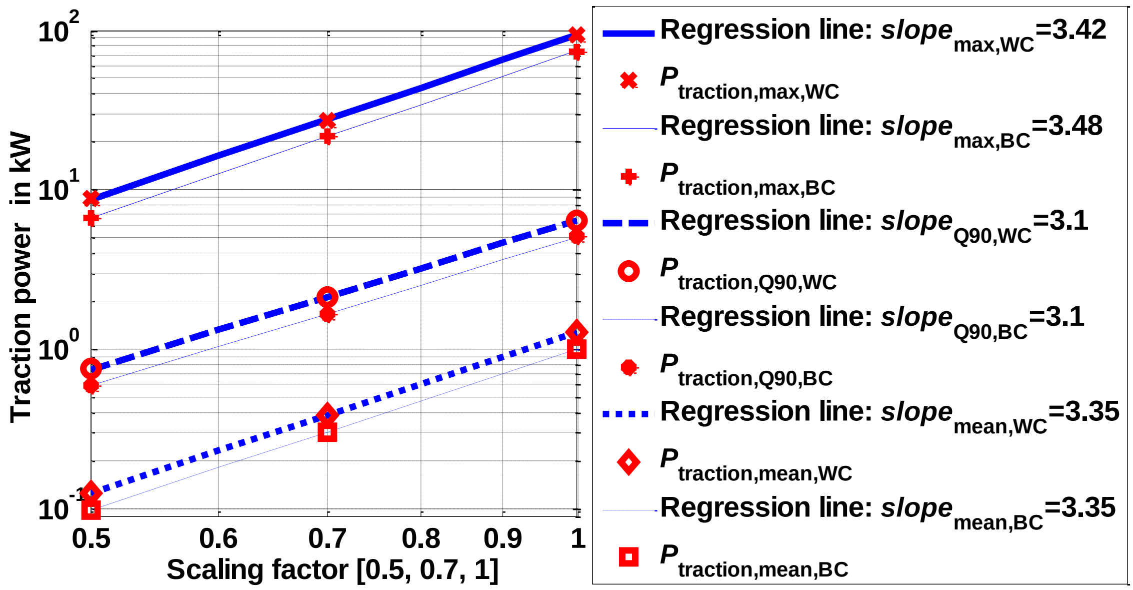

Figure 5.12: Regression lines for traction power and scaling factor – urban circuit

5.2.4 Friction Coefficient Demand

The friction coefficient demand reaches maximum values of about 0.75. The friction coefficient demand of the urban traffic circuit shows no difference between the drive units (Figure 5.13). Because the same relationship is found for the power demands of the drive units (Figure 5.11), the performed motion has equal omnidirectional requirements; thus, no preferred direction exists. For further details concerning characteristic values and the influence of scaling factors, see Table 5.5.

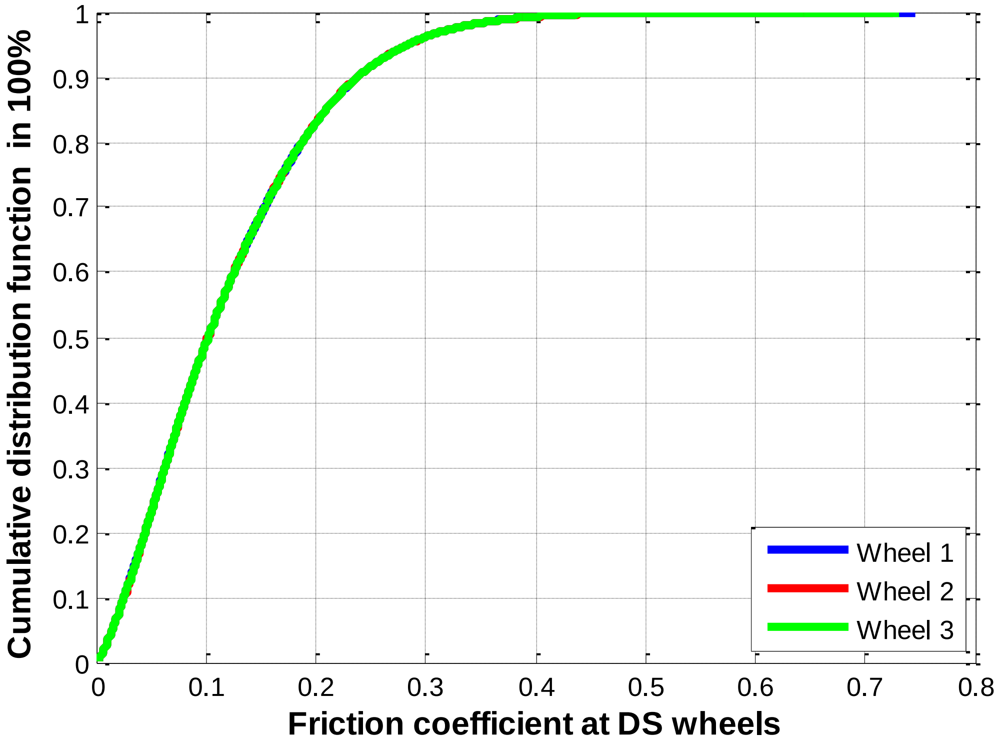

Figure 5.13: CDF plot of friction coefficient demand of the wheels – urban circuit

The influence of the scaling factor and the mass increase is unexpected at first sight. The results in Table 5.5 attest that the occurring peak values of the friction coefficient are greater for the BC than for the WC setup. This unexpected result is caused by the different characteristics of the translational as opposed to the yaw task. In accordance with the developed motion control of section 3.3, the translational forces are distributed under consideration of the wheel loads. The specific wheel load is only dependent on the mass (m_{total}), the height of the CG (h_{CG}), and the edge length (l_{t}) as corroborated exemplarily for one wheel of the WMDS by equation (66). Because h_{CG} and l_{t} are scaled equally in the treated BC and WC setups, the wheel load is a linear function of the mass increase. The translational force is also a linear function of the mass as shown in equation (67). As a result, the friction coefficient demand of the translational task is not influenced by the two setups.

$$F_{z,\mathrm{w},2} = \frac{-F_{\mathrm{CG},x} \cdot h_{CG}}{\sqrt{3} \cdot l_{\mathrm{t}}} + \frac{F_{\mathrm{CG},y} \cdot h_{\mathrm{CG}}}{l_{\mathrm{t}}} + \frac{m_{\mathrm{total}} \cdot g}{3}$$
$$\rightarrow F_{z,\mathrm{w},2} = m_{\mathrm{total}} \left(\frac{-a_{\mathrm{CG},x} \cdot h_{CG}}{\sqrt{3} \cdot l_{\mathrm{t}}} + \frac{a_{\mathrm{CG},y} \cdot h_{\mathrm{CG}}}{l_{\mathrm{t}}} + \frac{\cdot g}{3} \right) \tag{66}$$

$$\left|\vec{F}_{\mathrm{CG,trans}}\right| = \sqrt{{F_{\mathrm{CG},x}}^2 + {F_{\mathrm{CG},y}}^2}$$
$$\rightarrow \left|\vec{F}_{\mathrm{CG,trans}}\right| = m_{\mathrm{total}} \sqrt{{a_{\mathrm{CG},x}}^2 + {a_{\mathrm{CG,y}}}^2} \tag{67}$$

As a consequence the odd effect of the different setups is expected to be caused by the yaw task of the DS which distributes the wheel forces equally, not considering the wheel load distribution as described in section 3.3. The wheel force of the yaw task is not influenced by the BC and WC setup, as confirmed by equation (68), because $\Theta_{zz,\mathrm{DS}}$ and l_{t} are scaled equally. At second sight it becomes clear that the friction coefficient demand of the BC setup must be greater compared to the WC setup as the yaw force takes a greater share with respect to the different wheel loads of the setups and the corresponding translational force.

$$F_{\mathrm{yaw},i} = \frac{\left|\vec{M}_{\mathrm{CG,yaw}}\right|}{\sqrt{3} \cdot l_{\mathrm{t}}} = \frac{\Theta_{zz,\mathrm{DS}} \cdot \ddot{\psi}_{\mathrm{DS,ref}}}{\sqrt{3} \cdot l_{\mathrm{t}}} \tag{68}$$ [227]

The unexpected influence of the acceleration scaling is presented in Figure 5.14. The slopes of the presented regression lines differ significantly for the various characteristic values. One reason for this is the fact that the scaling factor is only applied onto the horizontal acceleration as aforementioned in section 3.2. The yaw acceleration is not scaled. Thus, the wheel forces for the yaw task are not affected by the applied scaling factor, so that only a part of the wheel forces is influenced. Hence, the DS requirements decrease if the yaw motion is also scaled. Future research should investigate the potential of scaling the yaw task.

[227] According to Table 3.8 (p. 74), the parameters $\Theta_{zz,\mathrm{DS}}$ and l_{t} are scaled equally.

Table 5.5: Influence of scaling and mass on friction coefficient demand – urban circuit

Falsification aspects			**Scaling factor**					
			1		**0.7**		**0.5**	
Friction coefficient	Mean	WC	0.10		0.06		0.04	
		BC		0.10		0.06		0.04
	Q90	WC	0.24		0.16		0.10	
		BC		0.24		0.16		0.10
	Max	WC	0.75		0.64		0.57	
		BC		0.86		0.75		0.68

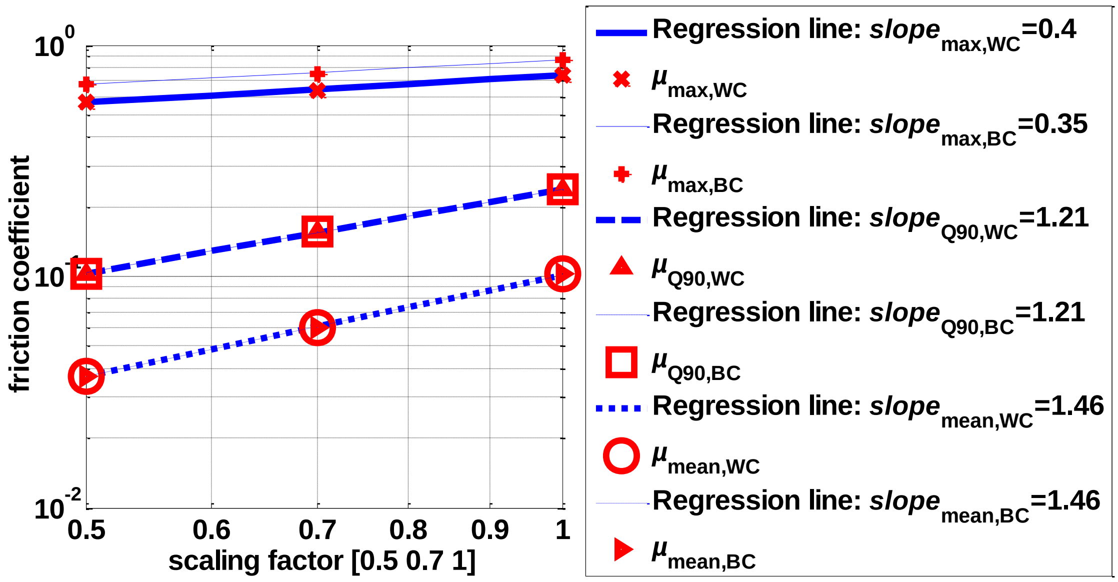

Figure 5.14: Regression lines for friction coefficient and scaling factor – urban circuit

5.3 Evaluation and Validation of the Control Architecture

In order to compare the four analyzed control setups, the error in a_x. a_y and $\ddot{\psi}$ is observed. The errors are presented as CDF plots allowing for a comprehensive comparison of the various control setups. The evaluation is conducted for the reference signal derived by the IPG CarMaker simulation of an 8-track as introduced in section 4.1.2 (no MCA). The results presented in this section were published in Betz et al.[228].

Figure 5.15 shows the CDF plot for the errors occurring in the described 8-track maneuver. The errors are defined as shown in equations (69) to (71). It occurs that the

[228] Betz et al.: Driving dynamics control of WMDS, 2013.

open-loop control setups in general show greater error than the closed-loop control setups. As expected, the dynamic algorithms allow for improvements in the acceleration simulation. Combining the dynamic algorithm with the closed-loop control to the so-called dynCLC setup causes the smallest error of all investigated control setups as substantiated in Figure 5.15. No other treated setup is able to perform better in any part of the CDF plot. Furthermore, no signal drift is observed for the dynCLC as presented in Figure 6.8 of appendix H.

$$a_{x,\mathrm{err}} = a_{x,\mathrm{ref}} - a_{x,\mathrm{sim}} \quad (69)$$

$$a_{y,\mathrm{err}} = a_{y,\mathrm{ref}} - a_{y,\mathrm{sim}} \quad (70)$$

$$\ddot{\psi}_{\mathrm{err}} = \ddot{\psi}_{\mathrm{ref}} - \ddot{\psi}_{\mathrm{sim}} \quad (71)$$

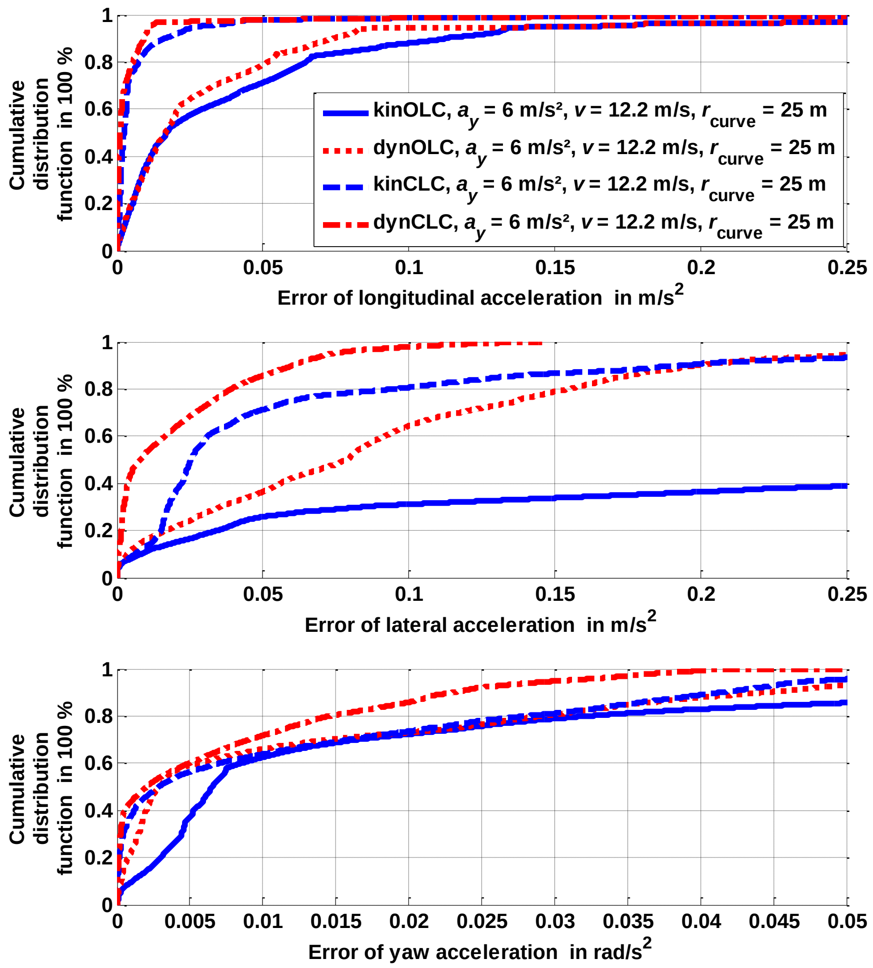

Figure 5.15: CDF plot of the acceleration errors with different control setups – 8-track[229]

[229] Betz et al.: Driving dynamics control of WMDS, 2013.

In order to analyze the influence of the maneuver's degree of dynamic on the created driving experience, a comparison for the 8-track maneuver is conducted using different constant velocities. The aforementioned test maneuver was simulated with a constant velocity of 12.2 m/s ($a_{y,\max} = 6\ \mathrm{m/s^2}$). Those results are compared in Figure 5.16 with a less dynamic 8-track maneuver using the same trajectory but only 7.1 m/s ($a_{y,\max} = 2\ \mathrm{m/s^2}$). The comparison is provided for only two of the analyzed control setups for the sake of readability. The best (dynCLC) and worst (kinOLC) control setups of the results of Figure 5.15 are selected. The results of Figure 5.16 show that the driving experience in terms of acceleration error is impeded by increased dynamics, but the dynCLC still provides promising results.

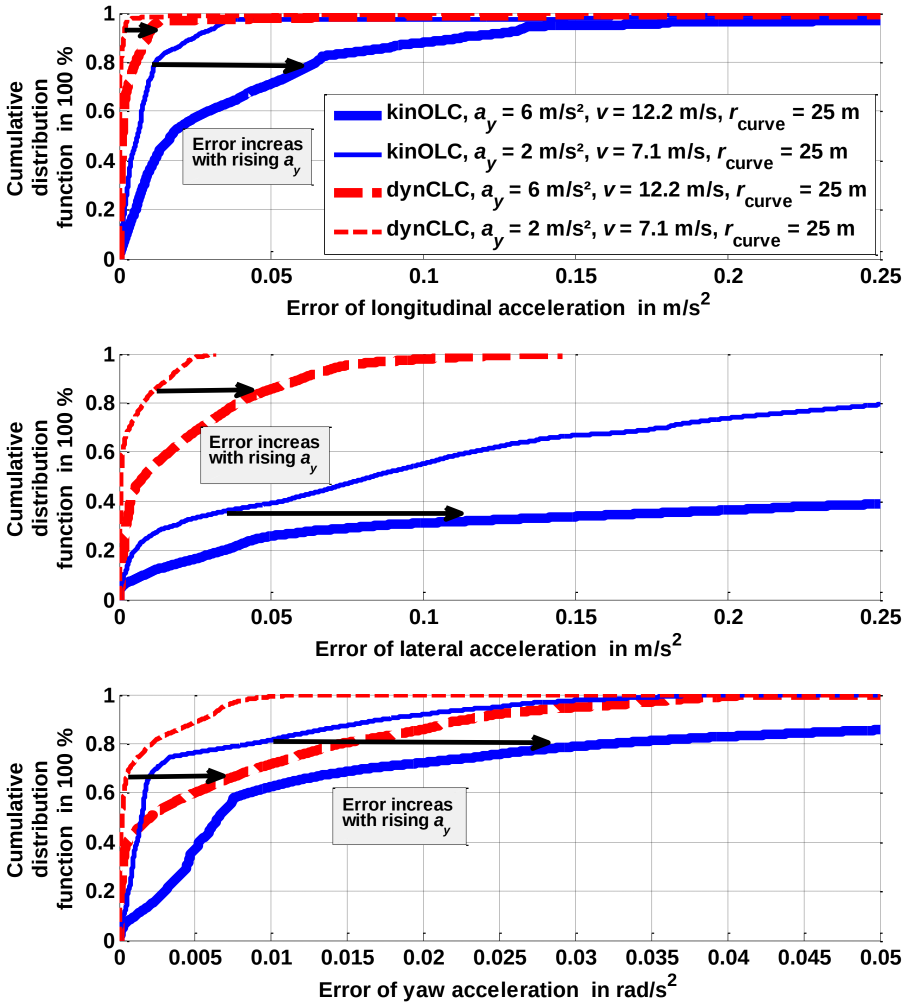

Figure 5.16: Comparison of the dynCLC and kinOLC setup – 8-track[230]

[230] cf. Betz et al.: Driving dynamics control of WMDS, 2013.

It should be stressed that the expected improvements of the advanced control setups in terms of reduced acceleration error are numerically validated. For the best analyzed control approach (dynCLC), the absolute error of the controlled variables is summarized in Table 5.6. The absolute error of the 99 % quantile meets the magnitude of human perception thresholds. According to Figure 5.15 and Figure 5.16, the generated error is reduced significantly. Hence, an improved driving experience is assumed.

Table 5.6: Absolute error of the controlled variables – dynCLC

	Error		
	$a_{x,\mathrm{err}}$ **in m/s²**	$a_{y,\mathrm{err}}$ **in m/s²**	$\ddot{\psi}_{\mathrm{err}}$ **in rad/s²**
Mean	0.001	0.008	0.002
Q90	0.009	0.06	0.023
Q99	0.135	0.119	0.039

5.4 Validation of the Safety Architecture

The concept of the safety architecture is validated by test drives utilizing the hardware prototype. The results are explained by one exemplary test drive. As shown in Figure 5.17, the prototype is accelerated to about 3 m/s. After acceleration of the system, a deceleration phase caused by coasting occurs before the mechanisms of the safety architecture are discharged. The measurement is conducted by a Correvit sensor and an acceleration based internal measurement unit (IMU). In Figure 5.17 the minimum velocity limit of the Correvit of 0.3 m/s and a drift of the integrated velocity signal is confirmed. In the following the evaluation considers the velocity values of the Correvit and the acceleration values of the IMU.

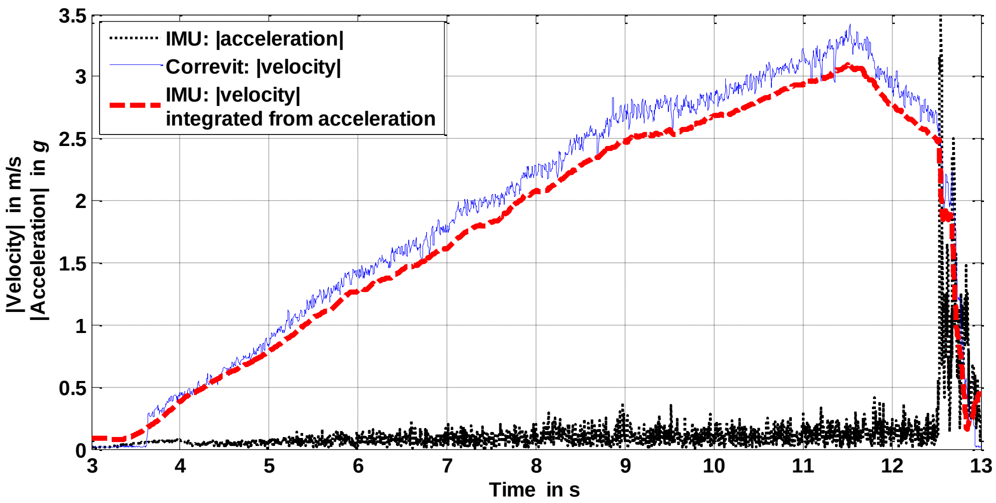

Figure 5.17: Exemplary test of the safety architecture

The relevant part of the measurement is presented in Figure 5.18. The deceleration due to the safety architecture starts at about 12.53 s. The acceleration signal shows a steep onset. At approx. 12.57 s the strong deceleration is paused for about 90 ms. The interruption is the result of a jump of the WMDS. For roughly 90 ms all contact patches are lifted from the ground due to the released energy of the safety architecture. The deceleration continues as soon as the friction pads are in ground contact again. The emergency stop lasts roughly 300 ms for the initial velocity of 2.4 m/s[231]. If the full emergency stop is considered, a mean deceleration of 7 m/s² is reached. If the jump can be avoided, the mean deceleration is expected to be increased towards 10 m/s². One possible approach to avoid the jump is optimized damping of the knee lever design. This measure is also expected to reduce the peak deceleration as the dynamic wheel load change of the friction elements is narrowed, causing less peak friction force. In Table 5.7 the results of the validation tests are summarized.

Table 5.7: Results of the exemplary validation tests of the safety architecture

Property	**Unit**	**Value**
Initial velocity at discharge of the safety system	m/s	2.4
Duration of emergency stop (to $v_{\text{correvit,min}} = 0.3\ \text{m/s}$)	ms	300
Duration of jump	ms	90
Mean deceleration	m/s²	7
Possible mean deceleration (no jump)	m/s²	up to 10
Peak deceleration	m/s²	35

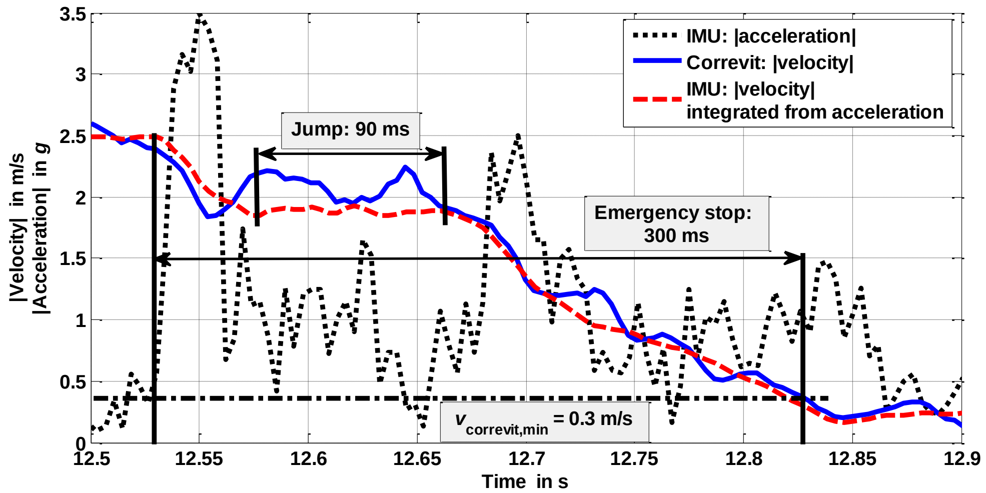

Figure 5.18: Deceleration phase of the exemplary test

231 Emergency stop at $v_{\text{initial}} = 2.4\ \text{m/s}$ to $v_{\text{correvit,min}} = 0.3\ \text{m/s}$ thus, 2.1 m/s are decelerated within 300 ms.

6 Conclusion and Outlook

6.1 Conclusion

This work provides a fundamental and systematic analysis of the WMDS approach. Bringing together the working hypothesis of section 1.2 and the presented results of section 5 creates the scientific merit of the present work.

H1: The wheeled motion base of a WMDS with its dynamics limited by friction forces is capable of simulating the horizontal dynamics of urban traffic for normal driver behavior considering common scaling factors.

Hypothesis H1 is evaluated with respect to the introduced falsification aspects by four test cases: the single T-junction maneuver, the representative urban traffic circuit, the 8-track maneuver, and the emergency stop.

I. Power demand[232]:
The power demand of the traction motors is confirmed by the T-junction maneuver and the urban traffic maneuver to be feasible with state-of-the-art technology as demonstrated by the hardware components of the created prototype. The ease achieved by use of conventional acceleration scaling does not have to be taken advantage of but may be used in order to reduce the requirements. The steer task turns out to yield the most critical challenge. While the biggest share of the steer task is less demanding than the drive task, the peak values of about 900 kW are tremendous. Those peak steer power demands may be fulfilled by some state-of-the-art electric motors but cause significant increase of system mass and costs. The results of the numerical analysis underlie the influence of the computing step size. Hence, the presented results of the steer task must be interpreted with respect to the chosen computing step size of 20 ms. If greater response delays are tolerated by the subject, the derived peak values will be reduced significantly[233]. It must be stressed that scaling brings no relief to the steer task because it causes reduced velocity profiles of the DS and thus more critical steer tasks due to standstill of the wheels. In any case, the contradictory characteristic of the steer task requires further research in order to identify methods for avoiding the

[232] see sections 5.1.2 and 5.2.3.

[233] According to equation (41) and (65) the power demand of the worst-case steer step is inversely proportional by the power of three to the tolerated response time.

occurrence of the critical steer tasks (90° steer step at low wheel velocities) or alternative approaches as shown by the caster wheels of Slob (section 2.6.2). This problem is of major importance for the industrialization of the WMDS because the overall system mass is affected by it, causing additional effort, costs, and loss of motion performance. The rare occurrence of the critical steer tasks and the leak of validated human perception models require hardware tests concerning tolerable compromise between required steer power and steer response at low velocities.

II. Energy demand[234]:
The long-term, real-world test drives in the representative urban traffic circuit are conducted by normal drivers and yield information about the average power demand of the wheeled motion base. The identified energy demand can be provided by state-of-the-art, on-board traction batteries of electric vehicles. Even the traction battery used in the prototype has enough capacity to provide an operation time span of about 2.5 h. The ease gained by utilizing conventional acceleration scaling does not have to be taken advantage of but can be used in order to reduce the energy demand.

III. Friction coefficient demand[235]:
The T-junction maneuver as well as the urban traffic circuit show friction coefficient demand that is below 0.75 and thus can be provided by conventional tire compounds[236]. The applicability of the specific tire compound of the press-on band tires used is not validated yet but seems to be promising regarding the coefficient of sliding friction identified in Wagner[237]. The ease achieved through utilizing conventional acceleration scaling does not have to be taken advantage of but can be used in order to reduce the friction coefficient demand.

IV. Motion control[238]:
The multi-body analysis of the 8-track maneuver validates the developed motion control and control architecture numerically. The developed coordination of the simulated traction and steer motors enables the acceleration task of the WMDS in numerical simulation. The introduced closed-loop control with linear slip an-

[234] see section 5.2.3.

[235] see sections 5.1.3 and 5.2.4.

[236] Seipel: Tire marks, p. 58-59, 2013.

[237] cf. Wagner: WMDS, p. 61, Master's thesis supervised by Betz, 2013.
Sliding friction test with tire compounds of the press-on band tire used: $\mu_{\text{sliding}} \in [0.61,\ 0.81]$ for sliding speed 100 – 2,000 mm/s and contact pressure 0.93 – 1.34 N/mm².

[238] see section 5.3.

gle estimation is also numerically validated to bring the expected reduction of the acceleration error in the three considered DOF $a_{x,\mathrm{err}}$, $a_{y,\mathrm{err}}$, and $\ddot{\psi}_{\mathrm{err}}$.

V. Safety architecture[239]:
The safety architecture is validated by hardware test. The clamping force enables the active hold of the preloaded spring. The knee lever reduces the required spring force and enables vertical stiffness when fully straightened (final position of knee lever in case of emergency stop). The utilized friction elements provide the friction coefficient as expected in the range between 0.7 and 1. The created mean deceleration of 7 m/s² is sufficient to stop the WMDS within an acceptable run-off area in case of an emergency. The wear of the elements must be observed further. The grit behavior seems to be promising because no spotty wear occurs. The grit has powdery characteristic and can be blown off. No significant marks remain. The first hardware tests show system jumps where the friction pads temporarily lose ground contact. Hence, future research will have to optimize the lifting process by suitable damping in order to reduce occurring wheel load change and thus create continuous friction force. The reduction of the peak deceleration yields reduced exposure of the subject and less mechanical stress for the safety system. Far-reaching improvements in terms of average power demand of the clamping task could be gained from alternative lifting concepts utilizing self-reinforcement. The basic idea of this improved safety architecture is prepared to be applied for a patent and will be analyzed in future research.

Further conclusions are drawn from the research of the present work:

- It becomes obvious that the conducted test drives of the urban traffic circuit cannot be realized in conventional DS halls without scaling the acceleration simulation due to enormous workspace demand. It is emphasized that real DS studies are conducted with scaling factors, optimized course of road, and further arrangements like shift of initial position or enforced vehicle stops by optical signaling systems. These measures optimize the usage of the available workspace and washout. Alternatively, outdoor tests on proving grounds might be considered if the available ground quality is sufficient. The requirements concerning tire-ground pairing should be researched in detail by hardware tests. If operation of the system at various locations is under consideration, the created independence of the infrastructure in terms of the WMDS's on-board energy supply and safety architecture will be highly advantageous.
- The analysis of the motion control function shows a minor effect of yaw forces on friction coefficient demand,[240] which supports the decision for the introduced

[239] see section 5.4.

[240] Betz et al.: Concept analysis of WMDS, 2012.

wheel force distribution that decouples the translational from the yaw task (section 3.3).

- The applied control architecture is only one representative solution. The multibody analysis validates the algorithm of the motion control and corroborates the expected improvement due to the model based closed loop control (Figure 5.15, p. 116). More advanced control approaches might exist that take advantage of knowledge of the behavior of the controlled system. These state-of-the-art methods should be analyzed with respect to the WMDS application in order to identify the potential improvements for the created driving experience.
- No preferred direction of the WMDS has been found. The drive units do not differ in relevant falsification aspects such as power and friction demand. Hence, the realized equilateral footprint of the WMDS is appropriate and will be retained.
- Only 1 % of the acceleration demand that occurred in the urban traffic circuit exceeds the expected range of the linear tire characteristic[241].

For the first time, the physical feasibility of a WMDS and its system limitations are scientifically investigated and enable an attempt into the sparsely researched state of factual information on the new class of DS. As shown by the insights gained into the WMDS, its feasibility is promising. Of all conducted effort of the present work, none has been able to falsify hypothesis H1. Therefore, H1 can be seen as proven. Because the numerical methods seem to be exhausted, the final effort of hardware validation is worthwhile for the sake of the overall validation of the WMDS. The hardware prototype and the safety architecture developed are unprecedented worldwide and thus enable the research of the pending objectives as presented in the following.

6.2 Outlook

The understanding gained of the WMDS system, the numerical models developed, and the hardware prototype created pave the way for the ongoing hardware validation of the WMDS and the following upcoming research goals:

- Analysis of the vertical behavior of the tire-ground pairing and the deducible ground requirements.

[241] General assumption of linear tire characteristics of pneumatic tires up to 4 m/s² – cf. Schramm et al.: linear single-track model, p. 244, 2010.

- Identification of the controlled system and the press-on band tire in order to optimize the models of the hybrid research environment consisting of numerical and experimental elements.
- Development of methods that prevent standstill of the wheels in order to reduce the peak requirements of the steer task.[242]
- Influence of the induced forces of the tilt system on the handling of the wheeled platform and vice versa. This task is of special interest if high-frequency hexapod motion is applied as it might be used for avoiding the wheel standstill.
- Investigation of the potential of reducing the WMDS requirements by scaling the yaw task.
- Transferability of the WMDS motion performance onto the driving simulation of single-track vehicles like motorbikes.
- Reduction of the average power demand of the safety architecture by utilizing the principle of self-reinforcement of the friction forces.
- Optimization of the lifting process of the safety architecture in terms of continuous friction force, thus avoiding peak decelerations for the subject and the mechanical system.[243]
- Hardware validation of the optimized safety architecture for the maximum operating velocity of the WMDS.

As a result of the present work, necessary insights into the new class of WMDS are gained. The technical challenges for the next generation of DS are identified, and the essential research goals that are required to advance missing system understanding are presented. The hardware prototype created will be helpful for acquiring information on elements that are difficult to simulate numerically, such as vertical excitation of the press-on band tires, system response and operating noise. Thus, the required research environment for meeting future scientific goals is created within the present work. Following this plan of action is expected to lead to the optimized design of a full-scale WMDS. The new DS architecture allows for far-reaching improvements of DS studies and is accompanied by cost reductions that enable a wider researcher base and the superior goal of traffic safety.

[242] First ideas suggest enhancing the washout algorithm in order to avoid wheel standstill by superimposed WMDS motion below human perception thresholds. A more dynamic measure would be to utilize the high-frequency translational motion of the hexapod in order to force the wheeled motion base to counteract the wheel standstill. Alternatively, the potential of caster wheels as illustrated by Slob (Slob: WMDS, 2009) could be analyzed.

[243] The suggested damping must be tuned for the redundant design of the safety architecture and the potential fail of up to 50% of the lifting systems.

A Limitations of Tilt Coordination

The limitations of the tilt coordination result from human perception thresholds of rotational rate and acceleration (pitch: $\dot{\varphi}_{\text{limit}}$. $\ddot{\varphi}_{\text{limit}}$; roll: $\dot{\vartheta}_{\text{limit}}$. $\ddot{\vartheta}_{\text{limit}}$). The derivation is exemplarily conducted for pitch motion.

$$a_x = \sin(\varphi)\, g = \sin(\omega t)\, \hat{a}_{\text{max}} \tag{72}$$

In order to solve the relation small angels for φ are assumed: $\sin(\varphi) = \varphi$.

$$\varphi \frac{1}{\text{rad}} g \approx \sin(\omega t)\, \hat{a}_{\text{max}}$$

$$\left|\dot{\varphi}_{\text{limit}} \frac{1}{\text{rad}} g\right| \approx |\omega \cos(\omega t)\, \hat{a}_{\text{max}}| \rightarrow for\ t = 0 \rightarrow\ \omega \approx \dot{\varphi}_{\text{limit}} \frac{g}{\hat{a}_{\text{max}}} \tag{73}$$

$$\rightarrow\ f_{\text{rot}.\dot{\varphi}} \approx \frac{g}{2\pi \hat{a}_{\text{max}}} \dot{\varphi}_{\text{limit}}$$

$$\left|\ddot{\varphi}_{\text{limit}} \frac{1}{\text{rad}} g\right| \approx |-\omega^2 \sin(\omega t)\, \hat{a}_{\text{max}}|$$

$$for\ \omega t = \frac{\pi}{2} \rightarrow\ \omega \approx \sqrt{\ddot{\varphi}_{\text{limit}} \frac{g}{\hat{a}_{\text{max}}}} \tag{74}$$

$$\rightarrow\ f_{\text{rot}.\ddot{\varphi}} \approx \frac{1}{2\pi} \sqrt{\ddot{\varphi}_{\text{limit}} \frac{g}{\hat{a}_{\text{max}}}}$$

B MCA

Table 6.1: Resulting type of filter in the optimal control algorithm[244]

Type of filter			Type of filter		
W_{22}	a_x	HP of 4th order	W_{11}	φ	$H \approx 1$
	a_y	HP of 4th order		θ	$H \approx 1$
	a_z	HP of 3rd order		ψ	HP of 3rd order
W_{12}	a_x, θ	LP of 5th order	W_{21}	φ, a_y	$H \approx 0$
	a_y, φ	LP of 5th order		θ, a_x	$H \approx 0$

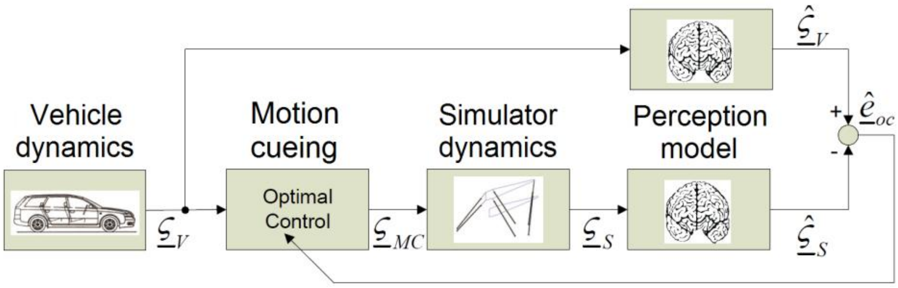

Figure 6.1: Optimization structure of the optimal control algorithm[245]

[244] cf. Nahon; Reid: MCA, 1990.

[245] cf. Fischer: MCA DLR, p. 30, 2009.

C State-of-the-Art DS

C.1 Toyota DS

Toyota's goal is to provide real-world driving experience up to 0.3 *g* and at least 4 Hz considering the provided information about ordinary driving (Figure 6.2 and Figure 6.3). According to Murano et al.[246] the acceleration amplitude of ±0.3 *g* fulfills 85-90 % of the analyzed driving experiences. This relationship accounts for various traffic characteristics around the world (Japan, US, Europe, Australia) as shown in Figure 6.2.

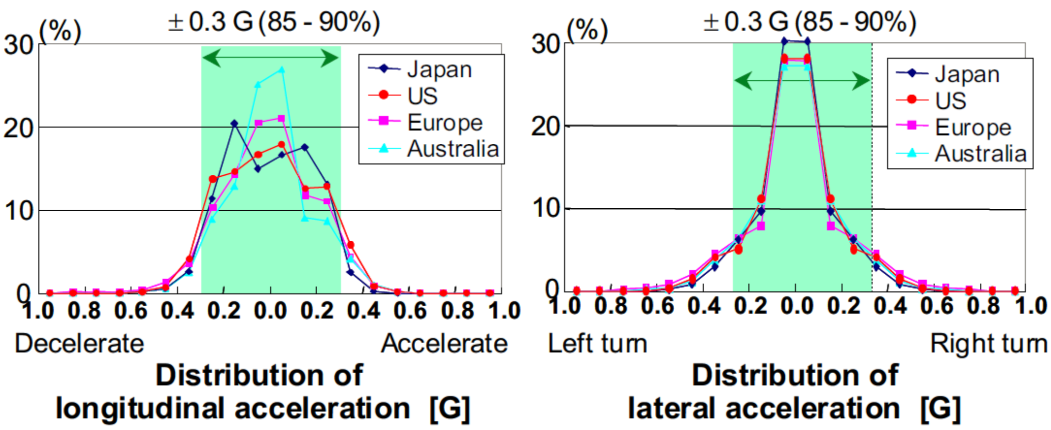

Figure 6.2: Acceleration in ordinary diving[246]

[246] Murano et al.: Toyota DS, 2009

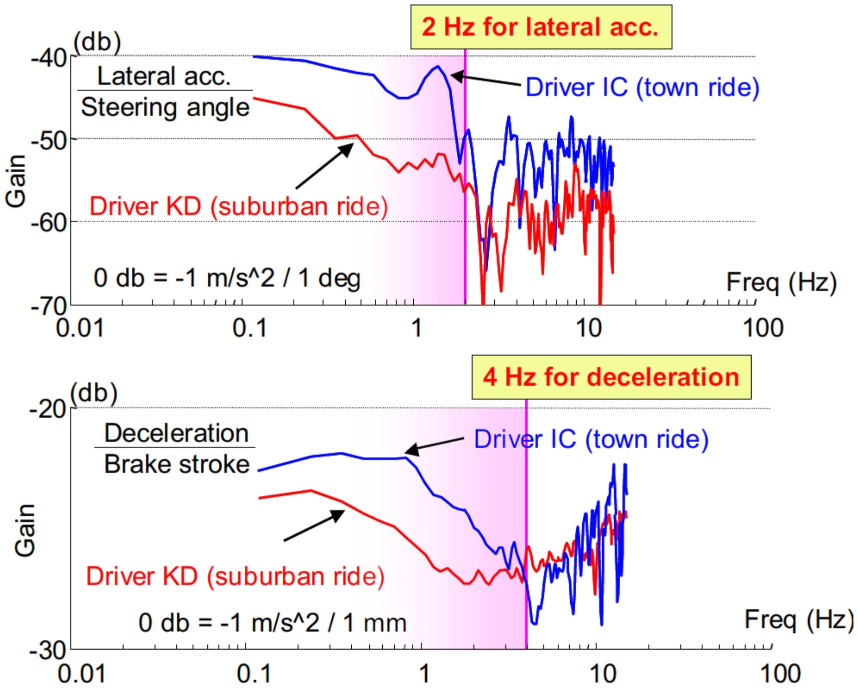

Figure 6.3: Frequency response on ordinary driving[247]

C.2 TNO VeHIL

This subsection contains the specification sheets of the TNO VeHIL steer motor and calculations concerning the steer performance.

[247] Murano et al.: Toyota DS, 2009

Technical Specifications

ALL CHARACTERISTICS MEASURED AT 25°C AMBIENT TEMPERATURE	SYMBOLS	UNITS	MSA-2	MSA-2	MSA-8	MSA-8	MSA-22	MSA-22	MSA-45
			220 VAC	400 VAC	220 VAC	400 VAC	220 VAC	400 VAC	400 VAC
MAX MECHANICAL SPEED	n	rpm	10000	10000	6500	6500	6000	6000	4500
STALL TORQUE (1) ±10%	M_S	Nm	1.9	1.9	9	9	26	26	44
STALL CURRENT	A	A	5.48	3.54	9.12	9.12	27.85	15.97	26.19
PEAK TORQUE ±10%	M_J	Nm	7.6	7.6	36	36	104	104	176
TORQUE-WEIGHT RATIO	T_W	Nm/kg	0.70	0.70	1.125	1.125	1.48	1.48	1.63
EMF CONSTANT ±5%	K_E	Vs/rad	0.20	0.31	0.57	0.57	0.54	0.94	0.97
TORQUE CONSTANT ±5%	K_T	Nm/A	0.35	0.54	0.99	0.99	0.93	1.63	1.68
RELUCTANCE TORQUE (Respect to the Stall Torque)	T_R	Nm	<1.5%	<1.5%	<1.5%	<1.5%	<1.5%	<1.5%	<1.5%
WINDING RESISTANCE ±5%	R	Ω	2.90	7.07	1.50	1.50	0.26	0.78	0.41
WINDING INDUCTANCE ±5%	L	mH	11.50	28.00	15.00	15.00	5.56	14.00	10.90
ROTOR INERTIA	J	kg m² 10^{-3}	0.05	0.05	0.45	0.45	2.3	2.3	4
MECHANICAL TIME CONSTANT	τ_M	ms	2.09	2.12	1.20	1.20	1.19	1.17	1.01
ELECTRICAL TIME CONSTANT	τ_E	ms	3.97	3.96	10.00	10.00	21.38	17.95	26.59
MASS (Motor with resolver)	M	kg	2.7	2.7	8	8	17.6	17.6	27
RADIAL LOAD	F_R	N	218	218	410	410	600	600	700
AXIAL LOAD	F_A	N	218	218	225	225	400	400	400
INSULATION			CLASS-F	CLASS-F	CLASS-F	CLASS-F	CLASS-F	CLASS-F	CLASS-F
PROTECTION			IP-65	IP-65	IP-65	IP-65	IP-65	IP-65	IP-65
(1) With an aluminium heat sink plate			300x300x10		400x400x10		700x700x20		

Figure 6.4: Specifications of the steer motor of the TNO VeHIL[248]

According to the specification sheet of the steer motor used (MAVILOR MSA-2. Figure 6.4) and the gear ration of the gearbox used (Sumitomo Cyclo Europe FC-A 15, $i = 59$)[249] the peak steer torque is 448.4 Nm[250]. The moment of inertia of the steer unit around the steer-axis is 2.7 kgm² [249]. Disregarding the drill moment of the tire, the maximum rotational acceleration is estimated in accordance with equation (75).

$$\theta_{z.\text{steer}}\ddot{\delta}_{\text{steer}} = T_{\text{steer}}$$
$$\rightarrow \ddot{\delta}_{\text{steer.max}} = \frac{T_{\text{steer.max}}}{\theta_{zz.\text{steer}}} = \frac{\text{T}_{\text{steer.motor.max}} \cdot i}{\theta_{zz.\text{steer}}} = \frac{7.6\ \text{Nm} \cdot 59}{2.7\ \text{Kgm}^2} = 166\,\frac{\text{rad}}{s^2} \qquad (75)$$

The 90° steer step is divided in an acceleration phase (first 45°) and a deceleration phase (last 45°). Assuming constant acceleration, the duration for the 45° motion is calculated in accordance with equation (76) and results in a time delay of 0.198 s for the overall goal of the 90° steer step. Because the drill moment was disregarded it must be stressed

[248] MAVILOR - virtual: http://www.mavilor.es/pdf_products/msa_series_sc.pdf, MSA-2, last access: May 26th 2014.

[249] Meulen: validation VeHIL, 2004.

[250] Peak torque of MAVILOR MSA-2 is 7.6 Nm. Transmission ratio of Sumitomo Cyclo Europe FC-A 15 is 59. According to MAVILOR, the MSA-2 is identical to the MSA-02 as used by VeHIL (e-Mail correspondence February 2014). The differing specifications are corrections. The specification sheet of the MSA-2 contains the correct values.

that the estimated time delay is a best-case assumption. The required maximum angular velocity of 16.4 rad/s (equation (77)) is provided by the steer unit.[251]

$$\delta = \frac{1}{2} \cdot \ddot{\delta} \cdot \Delta t^2$$

$$\rightarrow \Delta t_{45°.\mathrm{min}} = \sqrt{\frac{2 \cdot \delta}{\ddot{\delta}_{\mathrm{max}}}} = \sqrt{\frac{2 \cdot 45°}{166 \cdot \frac{180}{\pi} \frac{°}{\mathrm{s}^2}}} = 0.099\ \mathrm{s} \tag{76}$$

$$\rightarrow \Delta t_{90°\mathrm{step.min}} = 2 \cdot \Delta t_{45°.\mathrm{min}} = 0.198\ \mathrm{s}$$

$$\dot{\delta}_{\mathrm{steer.max}} = \ddot{\delta}_{\mathrm{steer.max}} \cdot \Delta t_{45°.\mathrm{min}} = 16.4 \frac{\mathrm{rad}}{\mathrm{s}} \tag{77}$$

[251] The maximum mechanical speed of *MAVILOR MSA-2* is 10,000 rpm → $1047\ 1/s$. Considering the gear ratio of the *Sumitomo Cyclo Europe FC-A 15* of $i = 59$ results in a maximum angular velocity of $\dot{\delta}_{steer,max} = 17.75 \frac{\mathrm{rad}}{\mathrm{s}}$.

D MCA: Tuning of the Feed Back Gains of the Washout

The gain of the open-loop is the basis of the tuning of the feedback gains according to the Nyquist criterion.

$$G_{\text{loop}} = \left(\frac{1 + s\tau_d}{s^2\tau_d\tau_v}\right)\frac{1}{1 + 2dTs + T^2\text{s}^2} = -c \tag{78}$$

$$\frac{1}{c\tau_d\tau_v} + \frac{1}{c\tau_v}j\omega - \omega^2 - 2dTj\omega^3 + T^2\omega^4 = 0 \tag{79}$$

$$\frac{1}{c\tau_d\tau_v} + \frac{1}{c\tau_v}j\omega - \omega^2 - 2dTj\omega^3 + T^2\omega^4 = 0 \tag{80}$$

Decomposing equation (87) into the imaginary and real part leads to:

$$\text{Imag: } \frac{1}{c\tau_v}j\omega - 2dTj\omega^3 = 0$$
$$\rightarrow \omega^2 = \frac{1}{c\tau_v 2dT} \tag{81}$$

$$\text{Real: } \frac{1}{c\tau_d\tau_v} - \omega^2 + T^2\omega^4 = 0, \omega^2 = \Omega$$
$$\frac{1}{c\tau_d\tau_v T^2} - \frac{1}{T^2}\Omega + T^2\Omega^2 = 0 \tag{82}$$
$$\rightarrow \Omega = \frac{1}{2T^2} \pm \sqrt{\frac{c\tau_d\tau_v - 4T^2}{4T^4 c\tau_d\tau_v}}$$

Expecting Ω to be real leads to the following constraint for the feedback gains:

$$\text{c}\tau_d\tau_v - 4T^2 > 0$$
$$\rightarrow \tau_d\tau_v > \frac{4T^2}{c} \tag{83}$$

E Motion Control: Influence of Translational Forces on the Yaw Task

The analytical analysis of the influence of the translational wheel forces on the yaw task is conducted in Mathematica. The result shows that the translational wheel force distribution introduced in section 3.3.1 has no influence on the yaw task.

In[1]:= $h_t = \text{Sqrt}[\text{Abs}[l_t]^\wedge 2 - (\text{Abs}[l_t] / 2)^\wedge 2]$

Out[1]= $\frac{1}{2}\sqrt{3}\,\text{Abs}[l_t]$

In[2]:= $F_{CG,x} = F_{CG,trans} * \text{Cos}[\rho]$

$F_{CG,y} = F_{CG,trans} * \text{Sin}[\rho]$

Out[2]= $\text{Cos}[\rho]\,F_{CG,trans}$

Out[3]= $\text{Sin}[\rho]\,F_{CG,trans}$

In[4]:= $F_{z,w,1} = m * g / 3 + F_{CG,x} * h_{cg} / h_t$

$F_{z,w,2} = F_{CG,y} * h_{cg} / \text{Abs}[l_t] + m * g / 3 - F_{CG,x} * h_{cg} / (2 * h_t)$

$F_{z,w,3} = -F_{CG,y} * h_{cg} / \text{Abs}[l_t] + m * g / 3 - F_{CG,x} * h_{cg} / (2 * h_t)$

$F_z = \text{FullSimplify}[F_{z,w,1} + F_{z,w,2} + F_{z,w,3}]$

Out[4]= $\frac{g\,m}{3} + \frac{2\,\text{Cos}[\rho]\,h_{cg}\,F_{CG,trans}}{\sqrt{3}\,\text{Abs}[l_t]}$

Out[5]= $\frac{g\,m}{3} - \frac{\text{Cos}[\rho]\,h_{cg}\,F_{CG,trans}}{\sqrt{3}\,\text{Abs}[l_t]} + \frac{\text{Sin}[\rho]\,h_{cg}\,F_{CG,trans}}{\text{Abs}[l_t]}$

Out[6]= $\frac{g\,m}{3} - \frac{\text{Cos}[\rho]\,h_{cg}\,F_{CG,trans}}{\sqrt{3}\,\text{Abs}[l_t]} - \frac{\text{Sin}[\rho]\,h_{cg}\,F_{CG,trans}}{\text{Abs}[l_t]}$

Out[7]= $g\,m$

In[8]:= $\mu_{trans} = \text{Sqrt}[F_{CG,x}^\wedge 2 + F_{CG,y}^\wedge 2] / (m_{total} * g)$

Out[8]= $\frac{\sqrt{\text{Cos}[\rho]^2\,F_{CG,trans}^2 + \text{Sin}[\rho]^2\,F_{CG,trans}^2}}{g\,m_{total}}$

In[9]:= $F_{trans,1} = \mu_{trans} * F_{z,w,1}$

$F_{trans,2} = \mu_{trans} * F_{z,w,2}$

$F_{trans,3} = \mu_{trans} * F_{z,w,3}$

Out[9]= $\left(\left(\frac{g\,m}{3} + (2\,\text{Cos}[\rho]\,h_{cg}\,F_{CG,trans}) \Big/ \left(\sqrt{3}\,\text{Abs}[l_t]\right)\right)\sqrt{\left(\text{Cos}[\rho]^2\,F_{CG,trans}^2 + \text{Sin}[\rho]^2\,F_{CG,trans}^2\right)}\right) \Big/ (g\,m_{total})$

Out[10]= $\left(\left(\frac{g\,m}{3} - \frac{\text{Cos}[\rho]\,h_{cg}\,F_{CG,trans}}{\sqrt{3}\,\text{Abs}[l_t]} + \frac{\text{Sin}[\rho]\,h_{cg}\,F_{CG,trans}}{\text{Abs}[l_t]}\right)\sqrt{\left(\text{Cos}[\rho]^2\,F_{CG,trans}^2 + \text{Sin}[\rho]^2\,F_{CG,trans}^2\right)}\right) \Big/ (g\,m_{total})$

Out[11]= $\left(\left(\frac{g\,m}{3} - \frac{\text{Cos}[\rho]\,h_{cg}\,F_{CG,trans}}{\sqrt{3}\,\text{Abs}[l_t]} - \frac{\text{Sin}[\rho]\,h_{cg}\,F_{CG,trans}}{\text{Abs}[l_t]}\right)\sqrt{\left(\text{Cos}[\rho]^2\,F_{CG,trans}^2 + \text{Sin}[\rho]^2\,F_{CG,trans}^2\right)}\right) \Big/ (g\,m_{total})$

In[12]:=
$$M_{yaw,F_{trans,1}} = \mathtt{FullSimplify[Sin[}\rho\mathtt{]} * F_{trans,1} * 2 / 3 * h_t\mathtt{]}$$
$$M_{yaw,F_{trans,2}} = \mathtt{FullSimplify[Sin[}\rho - 120 / 180 * \mathtt{Pi]} * F_{trans,2} * 2 / 3 * h_t\mathtt{]}$$
$$M_{yaw,F_{trans,3}} = \mathtt{FullSimplify[Sin[}\rho - 240 / 180 * \mathtt{Pi]} * F_{trans,3} * 2 / 3 * h_t\mathtt{]}$$
$$M_{yaw,\text{from trans}} = M_{yaw,F_{trans,1}} + M_{yaw,F_{trans,2}} + M_{yaw,F_{trans,3}}$$

Out[12]=
$$\left(\mathrm{Sin}[\rho]\sqrt{F_{CG,trans}^2}\left(\sqrt{3}\,g\,m\,\mathrm{Abs}[l_t] + 6\,\mathrm{Cos}[\rho]\,h_{cg}\,F_{CG,trans}\right)\right) \Big/ \left(9\,g\,m_{total}\right)$$

Out[13]=
$$\left(\mathrm{Cos}\left[\frac{\pi}{6} - \rho\right]\sqrt{F_{CG,trans}^2}\left(-g\,m\,\mathrm{Abs}[l_t] + \left(\sqrt{3}\,\mathrm{Cos}[\rho] - 3\,\mathrm{Sin}[\rho]\right)h_{cg}\,F_{CG,trans}\right)\right) \Big/ \left(3\sqrt{3}\,g\,m_{total}\right)$$

Out[14]=
$$\left(\mathrm{Cos}\left[\frac{\pi}{6} + \rho\right]\sqrt{F_{CG,trans}^2}\left(g\,m\,\mathrm{Abs}[l_t] - \left(\sqrt{3}\,\mathrm{Cos}[\rho] + 3\,\mathrm{Sin}[\rho]\right)h_{cg}\,F_{CG,trans}\right)\right) \Big/ \left(3\sqrt{3}\,g\,m_{total}\right)$$

Out[15]=
$$\left(\mathrm{Sin}[\rho]\sqrt{F_{CG,trans}^2}\left(\sqrt{3}\,g\,m\,\mathrm{Abs}[l_t] + 6\,\mathrm{Cos}[\rho]\,h_{cg}\,F_{CG,trans}\right)\right) \Big/ \left(9\,g\,m_{total}\right) +$$
$$\left(\mathrm{Cos}\left[\frac{\pi}{6} - \rho\right]\sqrt{F_{CG,trans}^2}\left(-g\,m\,\mathrm{Abs}[l_t] + \left(\sqrt{3}\,\mathrm{Cos}[\rho] - 3\,\mathrm{Sin}[\rho]\right)h_{cg}\,F_{CG,trans}\right)\right) \Big/ \left(3\sqrt{3}\,g\,m_{total}\right) +$$
$$\left(\mathrm{Cos}\left[\frac{\pi}{6} + \rho\right]\sqrt{F_{CG,trans}^2}\left(g\,m\,\mathrm{Abs}[l_t] - \left(\sqrt{3}\,\mathrm{Cos}[\rho] + 3\,\mathrm{Sin}[\rho]\right)h_{cg}\,F_{CG,trans}\right)\right) \Big/ \left(3\sqrt{3}\,g\,m_{total}\right)$$

In[16]:=
$$\mathtt{FullSimplify[}M_{yaw,\text{ from trans}}\mathtt{]}$$

Out[16]= 0

F Hardware Assembly

F.1 Drive Unit

The assembly of the drive unit is illustrated in Figure 6.5.

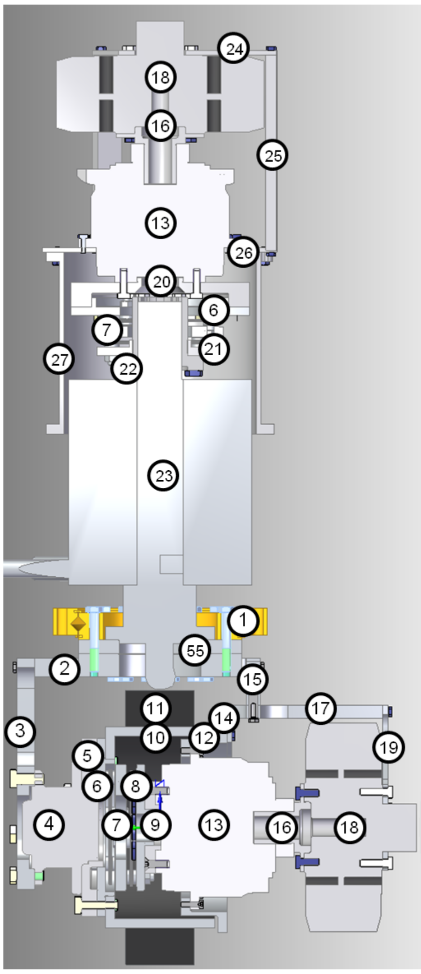

1 System bearing
2 Cross beam system bearing
3 Strut wheel hub
4 Wheel hub
5 Adapter wheel hub
6 Adapter rim
7 coupling
8 Outer adapter drive gearbox
9 Inner adapter drive gearbox
10 Rim
11 Tire
12 Sleeve drive gearbox
13 Gearbox
14 Strut drive gearbox
15 Strut drive motor
16 Adapter electric motor
17 Cross beam drive motor
18 Electric motor
19 Strut drive motor
20 Adapter steering gearbox
21 Adapter slip ring
22 Adapter spline shaft
23 Slip ring
24 Bracket steering motor
25 Strut steering frame
26 Bracket steering gearbox
27 Sleeve steering frame
55 Spacer slip ring

Figure 6.5: Final assembly of the drive unit[252]

[252] cf. Wagner: WMDS, Master's thesis supervised by Betz, 2013.

F.2 Safety Architecture

The following equations are derived in accordance with Figure 6.6.

Sum of moments about III:

$$\begin{aligned} F_{x.\mathrm{I}} \cdot (\cos(\varphi) \cdot l_1 + \cos(\beta) \cdot l_2) \\ = F_{\mathrm{act}} \cdot \cos(\alpha)\cos(\beta) \cdot l_2 - F_{\mathrm{act}} \cdot \sin(\alpha)\sin(\beta) \cdot l_2 \\ \rightarrow\ F_{x.\mathrm{I}} := F_{\mathrm{act}} \cdot \frac{\cos(\alpha)\cos(\beta) - \sin(\alpha)\sin(\beta)}{\cos(\varphi) \cdot l_1 + \cos(\beta) \cdot l_2} \cdot l_2 = F_{act} \cdot u_1 \end{aligned} \tag{84}$$

Sum of forces in x-direction:

$$\begin{aligned} F_{x.\mathrm{I}} + F_{x.\mathrm{III}} = F_{\mathrm{act}} \cdot \cos(\alpha) \\ F_{x.\mathrm{III}} = F_{\mathrm{act}}\left(\cos(\alpha) - \frac{\cos(\alpha)\cos(\beta) - \sin(\alpha)\sin(\beta)}{\cos(\varphi) \cdot l_1 + \cos(\beta) \cdot l_2} \cdot l_2\right) \\ \rightarrow\ F_{x.\mathrm{III}} = F_{\mathrm{act}}(\cos(\alpha) - u_1) \end{aligned} \tag{85}$$

Sum of forces in z-direction:

$$\begin{aligned} F_{z.\mathrm{I}} = F_{\mathrm{des}} + \mu_{\mathrm{slide}} F_{x.\mathrm{III}} - \sin(\alpha) F_{\mathrm{act}} \\ = F_{\mathrm{des}} + F_{\mathrm{act}}(\mu_{\mathrm{slide}}(\cos(\alpha) - u_1) - \sin(\alpha)) \end{aligned} \tag{86}$$

Sum of forces in F_{l1}-direction:

$$\begin{aligned} F_{l1} = \sin(\varphi) \cdot F_{x.\mathrm{I}} + \cos(\varphi) \cdot F_{z.\mathrm{I}} = \sin(\varphi) \cdot F_{\mathrm{act}} \cdot u_1 + \cos(\varphi) \cdot F_{\mathrm{des}} \\ + \cos(\varphi) \cdot F_{\mathrm{act}}(\mu_{\mathrm{slide}}(\cos(\alpha) - u_1) - \sin(\alpha)) \\ = F_{\mathrm{act}}(\sin(\varphi) u_1 + \cos(\varphi) \cdot (\mu_{\mathrm{slide}}(\cos(\alpha) - u_1) - \sin(\alpha))) + \cos(\varphi) \\ \cdot F_{\mathrm{des}} = F_{\mathrm{act}} u_2 + F_{\mathrm{des}} \cos(\varphi) \end{aligned} \tag{87}$$

Sum of forces in F_{l2}-direction:

$$\begin{aligned} F_{l2} = \sin(\beta) F_{x.\mathrm{III}} + \cos(\beta) F_{\mathrm{des}} + \cos(\beta) \mu_{\mathrm{slide}} F_{x.\mathrm{III}} \\ = \sin(\beta) F_{\mathrm{act}}(\cos(\alpha) - u_1) + \cos(\beta) F_{\mathrm{des}} + \cos(\beta) \mu_{\mathrm{slide}} F_{\mathrm{act}}(\cos(\alpha) \\ - u_1) \\ = F_{\mathrm{act}}(\cos(\alpha) - u_1)(\sin(\beta) + \cos(\beta) \mu_{\mathrm{slide}}) + \cos(\beta) F_{\mathrm{des}} \\ = F_{\mathrm{act}} u_3 + F_{\mathrm{des}} \cos(\beta) \end{aligned} \tag{88}$$

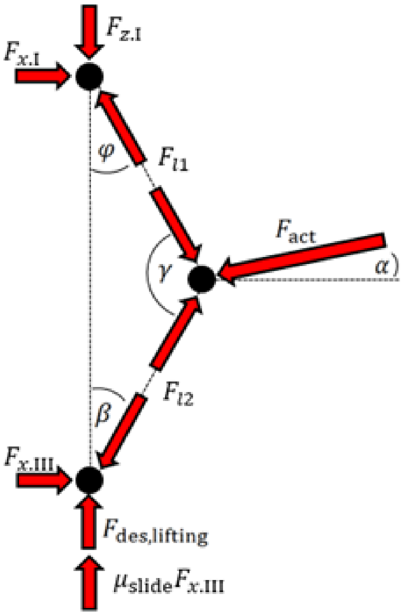

Figure 6.6: Free body diagram of knee lever

G Test Maneuvers

G.1 Urban Traffic Circuit

The precise course of road runs is shown in to Figure 6.7. The circuit contains the 25 selected traffic situations as summarized in Table 6.2. Further details concerning the representative urban traffic circuit are found in Graupner[253].

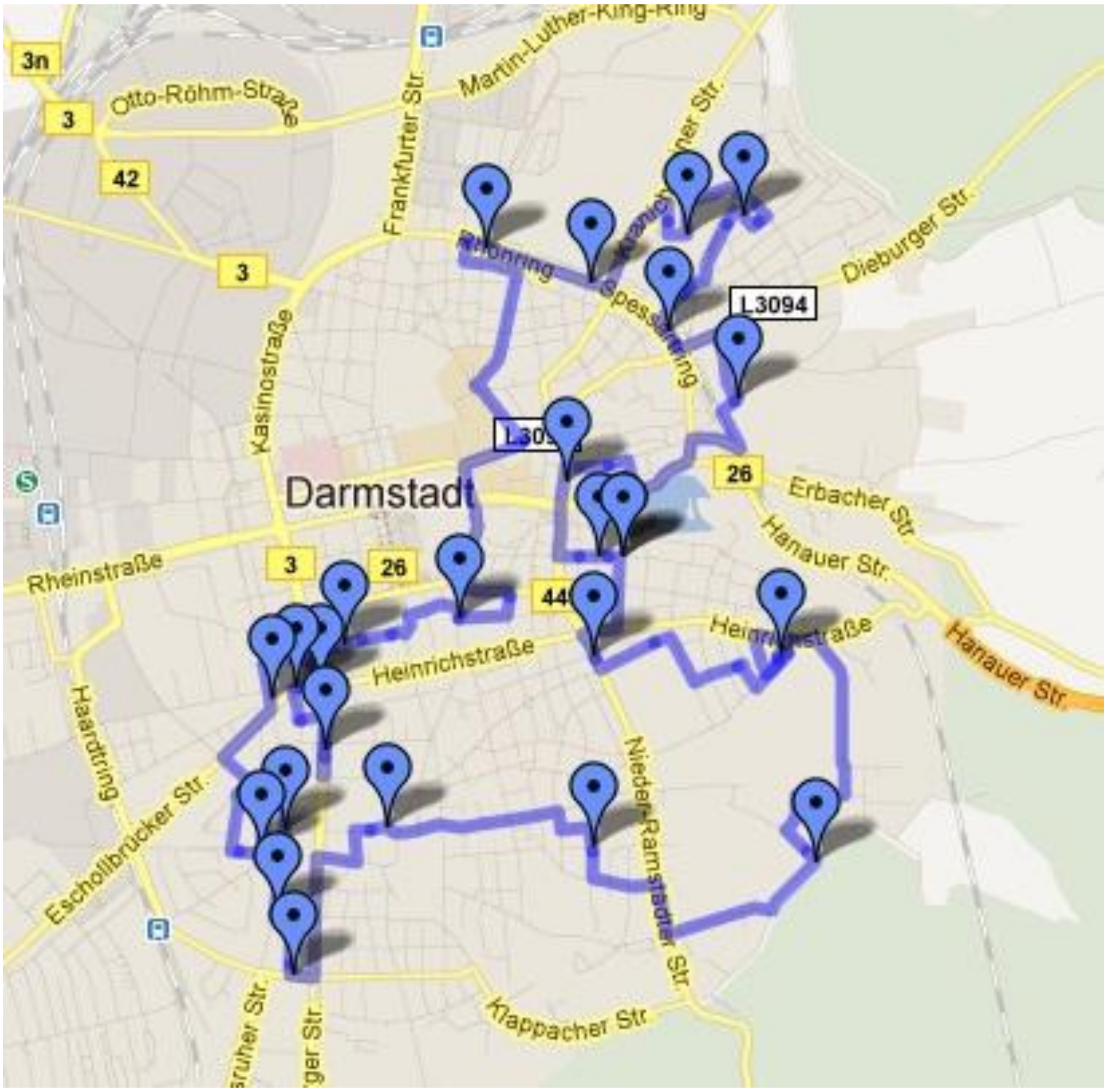

Figure 6.7: Urban traffic circuit[253]

[253] cf. Graupner: urban traffic circuit, Bachelor's thesis supervised by Betz, 2013.

Table 6.2: Composition of relevant traffic situations[253]

	Number of selected situations per group
Simple T-junction	5
General T-junction	4
X-crossing of side roads	3
X-crossing of major roads	4
Curves	5
Lane splitting	4
Lane merge	1
	25

H 8-Track Maneuver

The results of Figure 6.8 show no signal drift of the dynamic closed-loop control setup whereas the open-loop setup drifts away as can be seen by comparing the first and second cycle of the 8-track maneuver.

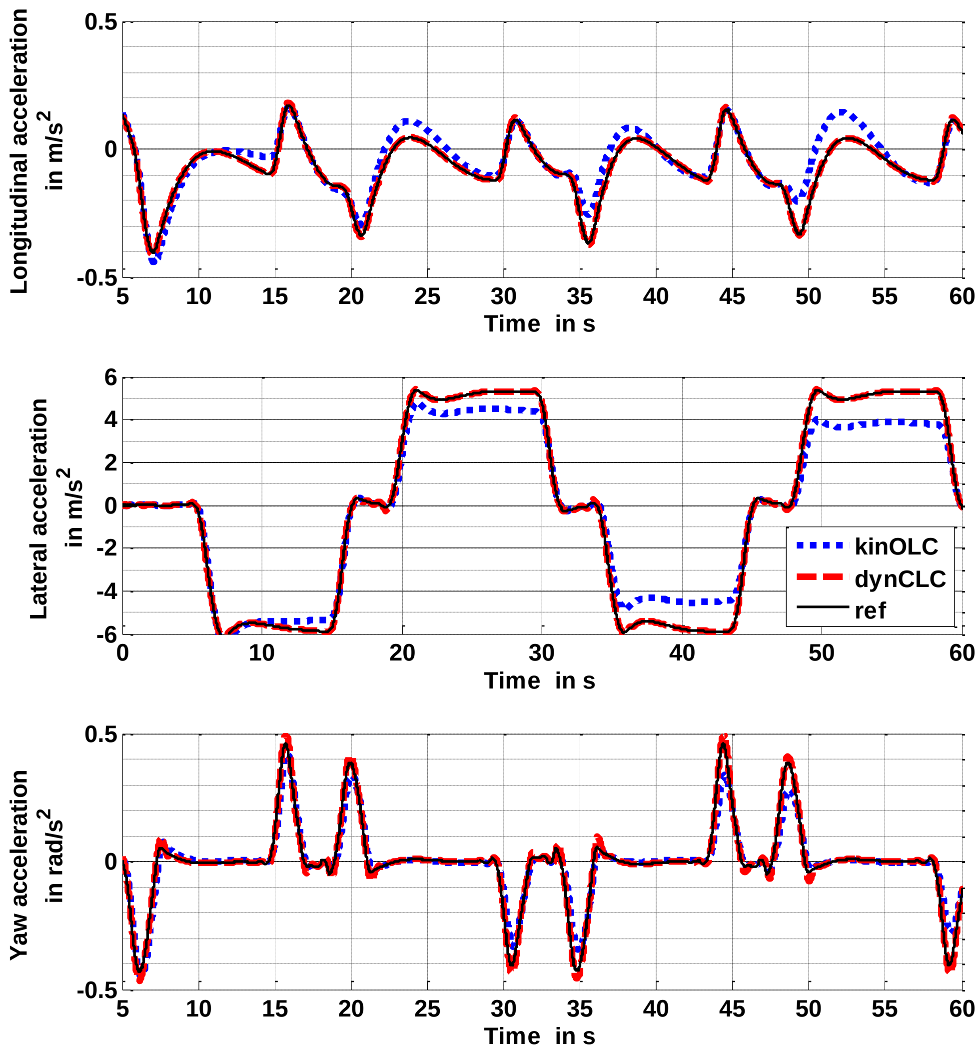

Figure 6.8: Time plot of the best and worst control setup[254]

[254] Betz et al.: driving dynamics control of WMDS, 2013.

Literaturverzeichnis

Allen, R. W.; Rosenthal, T. J.; Cook, M. L.: A Short History of Driving Simulation. Chapter 2 in: HANDBOOK OF DRIVING SIMULATION FOR ENGINEERING, MEDICINE, AND PSYCHOLOGY, Editors: Fisher D.L. & Rizzo, M. & Caird J. K. & Lee J.D., CRC Press: Taylor & Francis Group, FL, USA. 2011

Baarspul, M.: Flight Simulation Techniques with Emphasis on the Generation of High Fidelity 6 DOF Motion Cues. ICAS-86-5.3.3, S. 420-432. 1986

Baumann, G.; Riemer, T.; Liedecke, C.; Rumbolz, P.; Schmidt, A.; Piegsa, A.: The New Driving Simulator of Stuttgart University. 12^{th} International Stuttgart Symposium. Stuttgart, Germany. 2012

Beidl, C.: Lecture notes: VKMII, section 16, summer term 2013. Verbrennungskraftmaschinen und Fahrzeugantriebe, Technische Universität Darmstadt, Germany. 2013

Betz, A.: Konzeption einer Bewegungsplattform eines selbstbewegten Fahrsimulators mit 6 DoF und dessen Umsetzung in ein evaluierbares Modell. Master‘s thesis, Insitute of Automotive Engineering (Fachgebiet Fahrzeugtechnik), Technische Universität Darmstadt, Germany. 2010

Betz, A.; Winner, H.; Ancochea, M.; Graupner, M.: Motion Analysis of a Wheeled Mobile Driving Simulator for Urban Traffic Situations. Proceedings of Driving Simulation Conference 2012. p. 123-136. 6-7 September 2012 in Paris, France. 2012

Betz, A.; Hämisch, R.; Müller, M.; Winner, H.: Concept Analysis of a Wheeled Mobile Driving Simulator Showing an Omnidirectional Motion Base for Urban Traffic Simulation. SIMVEC - Berechnung, Simulation und Erprobung im Fahrzeugbau 2012, 20-21 November 2012, in Baden-Baden, Germany. 2012

Betz, A.; Butry, A.; Junietz, P.; Wagner, P.; Winner, H.: Driving Dynamics Control of a Wheeled Mobile Driving Simulator Utilizing an Omnidirectional Motion Base for Urban Traffic Simulation. Future Active Safety Technology toward zero-traffic-accident (FASTzero). 22.-26. September 2013 in Nagoya, Japan. 2013

Blana, E.: A Survey of Driving Research Simulators Around the World. Working Paper 481. Institute of Transport Studies, University of Leeds. 1996

Blaauw, G. J.: Driving Experience and Task Demands in Simulator and Instrumented Car: A Validation Study. HUMAN FACTORS 1982. 24(4). p. 473-486. 1982

Brünger-Koch, M.; Briest, S.; Vollrath, M.: Do you feel the difference? A motion assessment study. Proceedings of the Driving Simulation Conference Asia/Pacific 2006. May/June 2006 in Tsukuba, Japan. 2006

Carlsson, A.; Baumann, G.; Schmidt, A.; Reuss, H.-C.: VALIDATE – Eine virtuelle Forschungsplattform: Optimierung von Fahrzeugsystemen hinsichtlich des Energieverbrauchs. 14. VDI-Tagung: Erprobung und Simulation in der Fahrzeugentwicklung, 24-25 June 2009, Würzburg, Germany. 2009

Chapron, T.; Colinot, J.-P.: The new PSA Peugeot-Citroën Advanced Driving Simulator Overall design and motion cue algorithm. Driving Simulation Conference North America 2007. 12-14 September 2007 in Iowa City, Iowa, USA. 2007

Clark, A. J.; Sparks, H. V.; Carmein, J. A.: Unique Features and Capabilities of the NADS Motion System. Proceedings of the 17th International Technical Conference on the Enhanced Safety of Vehicles (ESV). 4-7 June 2001, Amsterdam, The Netherlands. 2001

Clark, B.; Steward, J. D.: Perception of Angular Acceleration About the Yaw axis of a Flight Simulator. Aerospace Med., Vol. 33, 1962

DART: Formular Student Electric, Electric System Form FS2013. Dart-Racing E37. Technische Universität Darmstadt. 2013

Deutsches Statistisches Bundesamt: Unfallgeschehen im Straßenverkehr 2007. Wiesbaden, Germany. 2008

Deutsches Statistisches Bundesamt: Unfallgeschehen auf deutschen Straßen 2008. Wiesbaden, Germany. 2009

Deutsches Statistisches Bundesamt: Verkehrsunfälle – Unfallentwicklung im Straßenverkehr 2009. Wiesbaden, Germany. 2010

DIN 70000: Fahrzeugdynamik und Fahrverhalten. ISO 8855. 1991

Dobbeck, R.: Darstellung von Beschleunigungen in Fahrsimulatoren bis in den Grenzbereich. Dissertation (Ph.D.), TU Berlin, Germany. 1974

Donges, E.: Fahrsimulator. Patent application DE 101 06 150 A 1, BMW AG. 2002

Durth, W.: Ein Beitrag zur Erweiterung des Modells für Fahrer, Fahrzeug und Straße in der Straßenplanung. Straßenbau und Verkehrstechnik, Volume 163. 1974

Fang, Z.; Reymond, G. Kemeny, A.: Performance Identification and Compensation of Simulator Motion Cueing Delays. Transactions of the ASME, Vol. 11, December 2011. 2011

Fischer, M.: Motion-Cueing-Algorithmen für eine realitätsnahe Bewegungssimulation. Dissertation (Ph.D.), Bericht aus dem DLR-Institut für Verkehrssystemtechnik, Volume 5, Braunschweig, Germany. 2009

FKFS – virtual: http://www.fkfs.de/fileadmin/media/02_mechatronik/05_fahrsimulatoren/pdf_dokumente/mech_pdf_5-1-1_Stuttgarter_Fahrsimulator_2010_de.pdf. Der Stuttgarter Fahrsimulator – Automobilforschung auf europäischem Spitzenniveau. Universität Stuttgart, Research Institute of Automotive Engineering and Vehicle Engines Stuttgart. Last access: January 30th 2014. 2010

FKFS – virtual: http://www.stuttgarter-zeitung.de/inhalt.fahrsimulator-an-der-uni-stuttgart-ein-technotanz-auf-sechs-beinen.717964bf-b72f-4ac2-bb52-2acd32909a87.html. Fahrsimulator an der Uni Stuttgart – Ein Technotanz auf sechs Beinen. Stuttgarter Zeitung. 9 December 2011. Last access: February 13th 2014. 2011

Fogel, L.: Biotechnology: Concepts and Application, Prentice-Hall, Inc., Englewood Cliffs, N.J.. 1963.

Grant, P.: The Development of Tuning Paradigm for Flight Simulator Motion Drive Algorithms. Dissertation (Ph.D.). Toronto. University of Toronto, Graduate Department of Aerospace Science and Engineering, Toronto, Canada. 1995

Grant, P.; Naseri, A.: Actuator State Based Adaptive Motion Drive Algorithm. Proceedings of Driving Simulation Conference North America 2005. November/December 2005 in Orlando, Florida, USA. 2005

Graupner, M.: Entwicklung eines repräsentativen Stadtparcours mittels makroskopischer Betrachtung lokaler Verkehrsbereiche. Bachelor’s thesis nr. 1084/11. Institute of Automotive Engineering (FZD), Technische Universität Darmstadt. 2011

Greenberg, J.; Artz, B.; Cathey, L.: The Effect of Lateral Motion Cues During Simulated Driving. Proceedings of DSC North America 2003. 8-10 October 2003 in Dearborn, Michigan, USA. 2003

Groen, E. L.; Bles, W.: How to use body tilt for the simulation of linear self motion. In: Journal of Vestibular Research, vol. 14, p. 375-385. 2004

Iwazaki, K.; Yonekawa, T.: Expert discussion, TOYOTA Corporation, Japan, October 15th 2013. 2013

Kerle, H.; Corves, B.; Hüsing, M.: Getriebetechnik. Grundlagen, Entwicklung und Anwendung ungleichmäßig übersetzender Getriebe. 4th edition. Wiesbaden. 2012

Knauer, M.: “Ampera soll Entwicklungskosten einfahren“. Automobilwoche, 6 July 2011. 2011

Lunze, J.: Regelungstechnik 1, Systemtheoretische Grundlagen, Analyse und Entwurf einschleifiger Regelungen. 8th edition. Springer-Verlag Berlin Heidelberg. 2010

McConnel, W. A.: Motion Sensitivity as a Guide to Road Design. SAE-Paper No. 770. 1957

van der Meulen, S. H.: Validation, Improvement and Analysis of Moving Base Simulation Model. Research report No. DCT 2004.56. Eindhoven University of Technology. Eindhoven, Netherlands. 2004

MeVEA – virtual: www.mevea.com, last access January 14th 2014

Miram, W.; Krumwiede, D. (Hg.): Informationsverarbeitung - Reiz-, Sinnes-, Neurophysiologie, Kybernetik. Schrödel Fachbuchverlag GmbH, Hannover, Germany. 1985

Mittelstädt, H.: A new solution to the problem of the subjective vertical. Max-Planck-Institut für Verhaltensphysiologie. Naturwissenschaften 70 272-281. 1983

Murano, T.; Yonekawa, T.; Aga, M.; Nagiri, S.: Development of High-Performance Driving Simulator. SAE Int. J. Passeng. Cars - Mech. Syst. 2(1). P. 661-669, doi:10.4271/2009-01-0450. 2009

NADS – virtual: http://www.nads-sc.uiowa.edu/media/pdf/NADS_2010Overview.pdf. National Advanced Driving Simulator – Overview 2010. Last access: January 14th 2014

NADS – virtual: http://www.nads-sc.uiowa.edu/sim_nads1.php, Homepage, last access: January 30th 2014

Nahon, M. A.; Reid, L. D.: Simulator Motion-Drive Algorithms: A designer's perspective. In: Journal of Guidance, Control and Dynamics, vol. 13(2), p. 356–362. 1990

Nordmark, S.: Driving Simulators, Trends and Experiences. In: VTI särtryck, p. 1–9. 1994

Pacejka, H.: Tire and Vehicle Dynamics. Issue 3. Elsevier. ISBN:0080970176. 2012

Pfaffenbichler, P. C.; Emmerling, B.; Jellinek, R., Krutak, R.: Pre-Feasibility-Studie zu „Markteinführung Elektromobilität in Österreich“. Bundesministerium für Verkehr, Innovation und Technologie (bmvit), Abteilung Mobilität und Verkehrstechnologien. Wien, Austria. 2009

RAST06: Richtlinien für die Anlage von Straßen. Issue 2006. Forschungsgesellschaft für Straßen- und Verkehrswesen. 2006

Reid, L. D.; Nahon, M. A.: Flight Simulation Motion-Base Drive Algorithms: Part 1 - Developing and Testing the Equations. University of Toronto. Toronto. UTIAS Report 296. 1985

Reymond, G.; Kemeny, A.; Droulez, J.; Berthoz, A.: Contribution on a Motion Platform to Kinesthetic Restitution in a Driving Simulator. Proceedings of the Driving Simulation Conference Europe. 7-8 July 1999 in Paris, France. 1999

Reymond, G.; Kemeny, A.: Motion Cueing in the Renault Driving Simulator. In: Vehicle System Dynamics, Bd. 34, p. 249-259. 2000

Reymond, G.; Heidet, A.; Canry, M.; Kemeny, A.: Validation of Renault's dynamic simulator for Adaptive Cruise Control experiments. Proceedings of the Driving Simulation Conference Europe. September in Paris, France. 2000

Richter, B.: BEITRAG ZUM PROBLEM DER BESCHLEUNIGUNGSSIMULIERUNG AN FAHRSIMULATOREN. Fachbereich Verkehrswesen der Technischen Universität Berlin. Berlin, Germany. 1971

Sammet, T.: Motion-Cueing-Algorithmen für die Fahrsimulation. Dissertation (Ph.D.). TU München, München, Germany. 2007

Seipel, G.: Analyse der Einflussgrößen auf die Entstehung und Intensität von Reifenspuren. Fortschritt-Berichte VDI Reihe 12 Nr. 772, ISBN 978-3-18-377212-4, Düsseldorf, Germany. 2013

Scholz, L.: Modellierung und Simulation von Elektromotoren einer Antriebseinheit für eine selbstfahrende Fahrsimulatorplattform. Master‘s thesis. Fachgebiet Fahrzeugtechnik, Technische Universität Darmstadt. Darmstadt, Germany. 2013

Schöner, H. P.: Expert discussion, Daimler AG, Stuttgart, Germany, Januar 17th 2014

Schramm, D.; Hiller, M.; Bardini, R.: Modellbildung und Simulation der Dynamik von Kraftfahrzeugen. Springer-Verlag Berlin Heidelberg. 2010

de Schrijver, P. A. R.: Control design for an over-actuated mobile robot including a nonlinear tyre model. Master's thesis. DCT2009.097. Technische Universiteit Eindhoven. Eindhoven, Netherlands. 2009

Slob, J.; Kuijpers, M.; Rosielle, P.; Steinbuch, M.: A New Approach to Linear Motion Technology – The Wall is the Limit. Proceedings of Driving Simulation Conference Europe 2009. Monaco. 2009

Stefani, A. M.: Report on Development of the National Advanced Driving Simulator Resulted in Substantial Cost Increases and Schedule Delays. U.S. Department of Transportation. Report Number: IN-2001-104. 28 September 2001. 2001

Stewart, D.: A Platform with Six Degrees of Freedom. Aircraft Engineering. p. 30-35. April 1966. 1966

Suikat, R.: The New Dynamic Driving Simulator at DLR. In: Driving Simulator Conference 2005. November/December 2005 in Orlando, Florida, USA (not published). 2005

Telban, R. J.: A Nonlinear Motion Cueing Algorithm with a Human Perception Model. Research Report, AIAA (American Institute of Aeronautics and Astronautics. 2002

Telban, R. J.; Cardullo, F. M.; Houck, J. A.: A nonlinear human-centered approach to motion cueing with neurocomputing solver. IAAA Modeling and Simulation Technologies Conference. 2002

Tiesler, G.: Bewegungswahrnehmung in Fahrzeugsimulatoren. Gesellschaft zur Förderung der astrophysikalischen Forschung e.V.-Forschungsinstitut für Anthropotechnik, Meckenheim Forschungsbericht, Nr. 12. 1973

TNO – virtual: https://www.tno.nl/downloads/vehilbrochure.pdf. Vehicle Hardware In the Loop (VeHIL): the synergy of real and virtual. TNO: Knowledge for business. 2008. Last access: January 14th 2014

Tomaske, W.: Einfluß der Bewegungsinformation auf das Lenkverhalten des Fahrers sowie Folgerungen für die Auslegung von Fahrsimulatoren. Dissertation (Ph.D.), University of the Federal Armed Forces Hamburg, Hamburg, Germany. 1983

TU Delft – virtual:
http://www.dcsc.tudelft.nl/Research/Old/project_og_bds_mv.html#fig_vehil_hall.
VeHIL. Last access: February 16th 2014

Wagner, P.: Aufbau und Inbetriebnahme eines selbstfahrenden Fahrsimulatorprüfstands. Master's thesis nr. 520/13. Institute of Automotive Engineering (FZD), Technische Universität Darmstadt. 2013

Wagner, P; Betz, A.; Winner, H.: CONCEPTION AND DESIGN OF MOBILE DRIVING SIMULATORS. Proceedings of the ASME 2014 International Design Engineering Technical Conferences & Computers and Information in Engineering Conference (IDETC/CIE) 2014. 17-20 August 2014 in Buffalo, New York, USA. 2014

Waldron, K; Schmiedeler, J.: Kinematics. In: Siciliano, B.; Khatib, O. (Eds.): Springer Handbook of Robotics. p. 9-31. Springer-Verlag Berlin Heidelberg. 2008

Weber – virtual: http://www.auto-motor-und-sport.de/news/daimler-reduziert-testfahrten-fahrsimulator-ersetzt-strassentests-2785201.html. Fahrsimulator ersetzt Straßentest. 5 October 2014. Last access: February 13th 2014

Wentink, M.; Valente Pais, R.; Mayrhofer, M.; Feenstra, P.; Bles, W.: First curve driving experiments in the Desdemona simulator, Proceedings of Driving Simulation Conference Europe 2008, January/February 2008 in Monaco. 2008

Zeeb, E.: Daimler's New Full-Scale, High-dynamic Driving Simulator – A Technical Overview. Proceedings of the Driving Simulation Conference Europe 2010. P. 157-165. 9-10 September 2010 in Paris, France. 2010

Zöller, I.; Betz, A.; Mautes, N.; Scholz, L.; Abendroth, B.; Bruder, R.; Winner, H.: VALID REPRESENTATION OF A HIGHLY DYNAMIC COLLISION AVOIDANCE SCENARIO IN A DRIVING SIMULATOR. Transportation Research Part F: Traffic Psychology and Behaviour. (accepted in 2014)

Zöller, I; Diederich, C.; Abendroth, B.; Bruder, R.: Fahrsimulatorvaliditätt – Systematisierung und quantitative Analyse bisheriger Forschung. Zeitschrift für Arbeitswissenschaft, 2013, 67 (4), p. 197-206. 2013

Eigene Veröffentlichungen

Betz, A.; Wagner, P.; Scheibe, T.; Winner, H.: Konzeptanalyse und Erprobung eines selbstfahrenden Fahrsimulators für die Simulation von Stadtverkehr. SIMVEC - Simulation und Erprobung in der Fahrzeugentwicklung 2014, 18-19 November 2014, in Baden-Baden, Germany. 2014

Betz, A.; Wagner, P.; Albrecht, T.; Winner, H.: Development and Validation of a Safety Architecture for a Wheeled Mobile Driving Simulator. Proceedings of the Driving Simulator Conference Europe 2014, Paris, France. 2014

Schweizerhof, H.; Betz, A.; Winner, H.: ANALYSIS OF A SITUATIONAL ADAPTIVE CHASSIS WITH RESPECT TO MANEUVERABILITY AND FOOTPRINT. Proceedings of the ASME 2014 International Design engineering Technical Conference & Computers and Information in Engineering Conference (IDETC/CIE) 2014. 17-20 August 2014 in Buffalo, New York, USA. 2014

Wagner, P; Betz, A.; Winner, H.: CONCEPTION AND DESIGN OF MOBILE DRIVING SIMULATORS. Proceedings of the ASME 2014 International Design Engineering Technical Conferences & Computers and Information in Engineering Conference (IDETC/CIE) 2014. 17-20 August 2014 in Buffalo, New York, USA. 2014

Zöller, I.; Betz, A.; Mautes, N.; Scholz, L.; Abendroth, B.; Bruder, R.; Winner, H.: VALID REPRESENTATION OF A HIGHLY DYNAMIC COLLISION AVOIDANCE SCENARIO IN A DRIVING SIMULATOR. Transportation Research Part F: Traffic Psychology and Behaviour. (accepted in 2014)

Betz, A.; Butry, A.; Junietz, P.; Wagner, P.; Winner, H.: Driving Dynamics Control of a Wheeled Mobile Driving Simulator Utilizing an Omnidirectional Motion Base for Urban Traffic Simulation. Future Active Safety Technology toward zero-traffic-accident (FASTzero). 22.-26. September 2013 in Nagoya, Japan. 2013

Betz, A.; Hämisch, R.; Müller, M.; Winner, H.: Concept Analysis of a Wheeled Mobile Driving Simulator Showing an Omnidirectional Motion Base for Urban Traffic Simulation. SIMVEC - Berechnung, Simulation und Erprobung im Fahrzeugbau 2012, 20-21 November 2012, in Baden-Baden, Germany. 2012

Betz, A.; Winner, H.; Ancochea, M.; Graupner, M.: Motion Analysis of a Wheeled Mobile Driving Simulator for Urban Traffic Situations. Proceedings of Driving Simulation Conference 2012. p. 123-136. 6-7 September 2012 in Paris, France. 2012

Betz, A.: Konzeption einer Bewegungsplattform eines selbstbewegten Fahrsimulators mit 6 DoF und dessen Umsetzung in ein evaluierbares Modell. Master's thesis, Insitute of Automotiv Engineering (Fachgebiet Fahrzeugtechnik), Technische Universität Darmstadt, Germany. 2010

Reul, M.; Betz, A.; Winner, H.: Optimierung des Anbremsvorgangs durch Koordination semi-aktiver Dämpfer mit ABS. 12. Internationale VDI-Tagung Reifen-Fahrwerk-Fahrbahn. 20.-21. Oktober 2009 in Hannover, Germany. 2009

Betreute studentische Arbeiten

Schweizerhof, H.: Entwicklung eines situativ anpassbaren Fahrwerks hinsichtlich Manövrierbarkeit und Aufstandsfläche. Diplomarbeit Nr. 525/13. 2013

Collado, C.: Anwendung eines Lösungsbaukastens für ein funktional zerlegtes Fahrwerk eines Fahrzeugs für den urbanen Verkehrsbereich. Master-Thesis Nr. 523/13. 2013

Wagner, P.: Aufbau und Inbetriebnahme eines selbstfahrenden Fahrsimulatorprüfstands. Master-Thesis Nr. 520/13. 2013

Cai, L.: Entwicklung eines Bremssystems für Elektrofahrzeuge. Master-Thesis Nr. 517/13. 2013

Arias, M.: Identifikation und Implementierung eines repräsentativen und hochdynamischen Fahrmanövers in IPG CarMaker. Bachelor-Thesis Nr. 1144/13. 2013

Nguyen, A.: Implementierung eines bestehenden Teststreckenverlaufs in IPG CarMaker. Bachelor-Thesis Nr. 1143/13. 2013

Tchomgouo, U.: Rechenzeitoptimierung eines Fahrdynamikmodells in IPG CarMaker und Matlab/Simulink. Bachelor-Thesis Nr. 1142/13. 2013

Butry, A.: Implementierung eines Reglers in ein bestehendes Fahrdynamikmodell für die omnidirektionale Grundplattform eines selbstfahrenden Fahrsimulators. Bachelor-Thesis Nr. 1139/13. 2013

Epenstein, S.; Schaffranek, T.; Wang, X.; Wartenberg, D. Wolkenhauer, S.: Auslegung, Konstruktion und Komponentenauswahl einer omnidirektionalen Bewegungsplattform eines selbstfahrenden Fahrsimulators. Advanced Design Project Nr. 46/13. 2013

Scholz, L.: Modellierung und Simulation von Elektromotoren einer Antriebseinheit für eine selbstfahrende Fahrsimulatorplattform. Master-Thesis Nr. 512/12. 2012

Müller, M.: Entwicklung eines fahrdynamischen Reglerkonzepts für die omnidirektionale Grundplattform eines selbstfahrenden Fahrsimulators. Master-Thesis Nr. 509/12. 2012

Wege, G.: Entwicklung eines Lösungsbaukastens für ein funktional zerlegtes Fahrwerk eines Fahrzeugs für den urbanen Verkehrsbereich. Studienarbeit Nr. 1116/12. 2012

Dressler, S.: Entwicklung einer Fahreinheit für die omnidirektionale Bewegungsplattform eines selbstfahrenden Fahrsimulators für Verifikationsversuche. Bachelor-Thesis Nr. 1115/12. 2012

Stallings, M.: Identifikation der inversen Kinematik eines Tripodsystems unter Verwendung von MapleSim. Bachelor-Thesis Nr. 1114/12. 2012

Wolkenhauer, S.: Entwicklung eines virtuellen Prototypens einer selbstfahrenden Fahrsimulatorplattform in MapleSim. Bachelor-Thesis Nr. 1113/12. 2012

Junietz, P.: Entwicklung eines virtuellen Prototypens einer selbstfahrenden Fahrsimulatorplattform in IPG CarMaker. Bachelor-Thesis Nr. 1112/12. 2012

Rathgeber, C.; Gründing, D.; Hämisch, R.; Scholz, L.; Cai, L.: Entwicklung einer Fahreinheit für die omnidirektionale Bewegungsplattform eines selbstfahrenden Fahrsimulators. Advanced Design Project Nr. 41/12. 2012

Hämisch, R.: Entwicklung eines virtuellen Prototypen einer selbstfahrenden Fahrsimulatorplattform in MSC ADAMS. Bachelor-Thesis Nr. 1091/11. 2011

Graupner, M.: Entwicklung eines repräsentativen Stadtparcours mittels makroskopischer Betrachtung lokaler Verkehrsbereiche. Bachelor-Thesis Nr. 1084/11. 2011

Ancochea, M.: Entwicklung und Inbetriebnahme eines Prüfstands zur Untersuchung des Verhaltens von Linearaktoren auf Längs- und Querkräfte. Bachelor-Thesis Nr. 1079/11. 2011

Krpo, E.: Entwicklung einer Methodik zur Bewertung repräsentativer innerstädtischer Verkehrssituationen. Studienarbeit Nr. 1068/11. 2011

Lebenslauf

Persönliche Daten

Name:	Alexander Betz
Geburtsdatum:	01.02.1986
Geburtsort:	Regensburg

Schulzeit

1992 - 1996	Grundschule, An den Linden in Rödermark
1996 - 2005	Gymnasium, Ricarda-Huch-Schule in Dreieich-Sprendlingen Abschluss: Abitur

Studium

2005 - 2008	Studiengang Maschinenbau – Mechanical and Process Engineering Technische Universität Darmstadt Abschluss: BACHELOR OF SCIENCE (B.Sc.)
2008 - 2010	Studiengang Maschinenbau – Mechanical and Process Engineering Technische Universität Darmstadt und Virginia Polytechnic Institute and State University, USA Abschluss: MASTER OF SCIENCE (M.Sc.)

Berufstätigkeit

2010 - 2014	Wissenschaftlicher Mitarbeiter am Fachgebiet Fahrzeugtechnik der Technischen Universität Darmstadt